Spring 5-1-2014

Materials and Surface Processes at Gale Crater and the Moons of Mars Derived from High Spatial and Spectral Resolution Orbital Datasets

Abigail Ann Fraeman
Washington University in St. Louis

WASHINGTON UNIVERSITY IN ST. LOUIS

Department of Earth and Planetary Sciences

Dissertation Examination Committee:
Raymond Arvidson, Chair
Jeffrey Catalano
Martin Israel
Bradley Jolliff
William McKinnon

Materials and Surface Processes at Gale Crater and the Moons of Mars Derived from High Spatial and Spectral Resolution Orbital Datasets

by

Abigail Ann Fraeman

A dissertation presented to the
Graduate School of Arts and Sciences
of Washington University in
partial fulfillment of the
requirements for the degree
of Doctor of Philosophy

May 2014

St. Louis, Missouri

TABLE OF CONTENTS

LIST OF FIGURES vi

LIST OF TABLES viii

ACKNOWLEDGEMENTS ix

ABSTRACT OF THE DISSERTATION xi

Chapter 1: Introduction to the Dissertation 1

References Cited 6

Chapter 2: Analysis of Disk-Resolved OMEGA and CRISM Spectral Observations of Phobos and Deimos 9

Abstract 9

2.1 Introduction 10

2.2 Overview of Data Sets 11

2.3 Retrieval of Spectrophotometric Properties 14

2.3.1 Overview 14

2.3.2 Solar-dominated regime 16

2.3.3. Mixed solar and thermal regimes 18

2.4 Analysis of Phobos and Deimos Spectra 20

2.4.1 Search for spectral absorption features 20

2.4.2 Comparisons to laboratory spectra 21

2.4.3 Effects of space weathering 23

2.5 Summary and Conclusions 25

2.6 Acknowledgements 26

2.7 Tables 27

2.8 Figures 29

2.9 References Cited 42

Chapter 3: Spectral Absorptions on Phobos and Deimos in the Visible/Near Infrared Wavelengths and Their Compositional Constraints 49

Abstract 49

3.1 Introduction 50

3.2 Data Reductions and Visible/Near-Infrared Absorptions in CRISM Observations 51

3.3 Spectral Analysis 53

3.3.1 Standard band depth mapping 53

3.3.2 Spectral feature at 0.65 μm observed in multiple datasets 54

3.3.3 Spectral feature at 2.8 μm 57

3.4 Comparison to Asteroid Spectra 59

3.5 Comparison to Lab Spectra 61

3.5.1 Spectral feature at 0.65 μm 61

3.5.2 Spectral feature at 2.8 μm 63

3.6 Discussion and Compositional Interpretations 64

3.6.1 Hypothesis as desiccated phyllosiliciates 64

3.6.2 Exogenic hypotheses: nanophase Fe and solar wind implanted H 65

3.7 Summary 67

3.8 Acknowledgements 68

3.9 Figures 69

3.10 References Cited 77

Chapter 4: A Hematite-Bearing Layer in Gale Crater: Mapping and Implications for Past Aqueous Conditions 85

Abstract 85

4.1 Introduction 85

4.2 Spatial Processing of CRISM Along-Track Oversampled Data 87

4.3 Mapping of Crystalline Hematite and Additional Mineral Phases 88

4.4 Hematite Ridge Geology Setting and Formation Hypotheses 89

4.5 Acknowledgements 93

4.6 Figures 94

4.7 Reference Cited 98

Chapter 5: Future *In Situ* Observation of the Hematite Ridge with Curiosity 102

Abstract 102

5.1 Introduction 102

5.2 Background: Curiosity Payload 103

5.2.1 Mast-mounted remote sensing instruments 103

5.2.2 Arm contact science instruments 104

5.2.3 Rover body instruments 105

5.3 Curiosity's Initial Observations of the Ridge 106

5.4 Ridge Approach and Initial Reconnaissance 108

5.5 Distinguishing Between Hematite Textures Using Contact Science 110

5.5.1 Iron oxides as dominant phase 110

5.5.2 Cements 112

5.5.3 Coatings 113

5.6 Conclusions 114

5.7 Acknowledgements 115

5.8 Tables 116

5.9 Figures 119

5.10 References Cited 134

LIST OF FIGURES

Figure 2.1: HRSC and OMEGA observations of Phobos with viewing geometries 29

Figure 2.2: HiRISE and CRISM observations of Phobos with viewing geometries 30

Figure 2.3: Demonstration of importance of reflected solar radiance and themal emission in OMEGA L-detector data..... 31

Figure 2.4: Representative Phobos I/F Spectra from CRISM and OMEGA 32

Figure 2.5: HiRISE and CRISM observations for Deimos with viewing geometries 33

Figure 2.6: Representative Deimos I/F Spectrum from CRISM..... 34

Figure 2.7: Range of incidence and emergence angles in the OMEGA datasets 35

Figure 2.8: Global average best-fit single scattering albedo..... 36

Figure 2.9: I/F and SSA spectra from the same regions on Phobos and Deimos 37

Figure 2.10: Demonstrations of attempts to thermally correct OMEGA data to 5 μm 38

Figure 2.11: Representative Phobos and Deimos SSA spectra from CRISM and OMEGA..... 39

Figure 2.12: Comparison of Phobos and Deimos spectra to laboratory analogs, the Moon, and Mercury..... 40

Figure 3.1: Context HiRISE and CRISM images of Phobos and Deimos..... 69

Figure 3.2: Representative CRISM I/F and SSA spectra from Phobos and Deimos..... 70

Figure 3.3: Mineral parameter maps of CRISM Phobos and Deimos data 71

Figure 3.4: SSA and telescopic spectra showing absorption at 0.65 μm in Phobos Red Unit 72

Figure 3.5: Thermally corrected CRISM SSA spectra showing absorption near 2.7 μm..... 73

Figure 3.6: Asteroid spectra with 0.65 μm feature 74

Figure 3.7: Asteroid spectra with 2.7 μm feature 75

Figure 3.8: Comparison of CRISM Phobos red unit spectra to laboratory analogs and models .. 76

Figure 4.1: Ridge context map 94
Figure 4.2: CRISM mineral detections at and around ridge 95
Figure 4.3: Geologic setting of ridge 96
Figure 4.4: CRISM ridge spectrum and laboratory analogs 97
Figure 5.1: Instruments on the Curiosity Mars Rover 119
Figure 5.2: Curiosity traverse in Gale Crater 120
Figure 5.3: Sol 45 Mastcam Mosaic of Hematite Ridge 121
Figure 5.4: Mastcam spectral parameter mapping of ridge 122
Figure 5.5: ChemCam Passive Spectra of Hematite Ridge 123
Figure 5.6: Curiosity rover size in relationship to ridge 124
Figure 5.7: Ridge accessibility 125
Figure 5.8: Iron oxide and oxyhydroxide samples 126
Figure 5.9: Massive sample spectrum 127
Figure 5.10: Massive sample thin section and backscatter electron image 128
Figure 5.11: XRD analysis of massive sample 129
Figure 5.12: Cemented sample thin section and backscatter electron image 130
Figure 5.13: Cemented sample spectra 131
Figure 5.14: Coated sample spectra 132
Figure 5.15: Coated sample thin section and backscatter electron image 133

LIST OF TABLES

Table 2.1: Summary OMEGA and CRISM Phobos and Deimos disk-resolved observations.....27

Table 5.1: Summary of Expected Observations for Iron Oxides with Different Textures.....116

Table 5.2: Weight % Oxides for Massive Samples 117

Table 5.3: Weight % Oxides for Cement Samples 117

Table 5.4: Weight % Oxides for Coated Samples 118

ACKNOWLEDGEMENTS

First and foremost I would like to acknowledge my advisor, Raymond Arvidson, for his outstanding mentorship and patient guidance over the last five years. I would also like to acknowledge all the co-authors who have helped me with this work through intellectual discussion, particularly Jeff Catalano, Dick Morris, and Scott Murchie. Thank you to the members of my thesis defense committee for volunteering their time to read and comment on this thesis and to listen to me defend it. I also want to acknowledge the grad students and postdocs in the department who have helped make grad school life so memorable, and the staff of the remote sensing lab for making lab logistics so easy. Finally, I want to acknowledge my family whose unconditional love and support over the last five years, and for the twenty-two before that, allowed me to find and follow my passions, and without whom none of this would have been possible.

This work was supported by a National Science Foundation Graduate Research Fellowship Program (Grant DGE-1143954), a Mr. and Mrs. Spencer T. Olin Fellowship for Women in Graduate Study, and a P.E.O. Scholar Award. Additional funding to support the three months I spent working on Curiosity operations at the Jet Propulsion Laboratory was provided by the NASA Participating Scientist program and the McDonnell Center for Space Sciences at Washington University in St. Louis.

For my Parents,

who have always encouraged me to ask questions

ABSTRACT OF THE DISSERTATION

Materials and Surface Processes at Gale Crater and the Moons of Mars

Derived from High Spatial and Spectral Resolution Orbital Datasets

by

Abigail Ann Fraeman

Doctor of Philosophy in Earth & Planetary Sciences

Washington University in St. Louis, 2014

James S. McDonnell Distinguished University Professor Raymond Arvidson, Chair

The compositions of terrestrial planetary bodies reflect the geologic processes that have shaped them over time. This thesis is a collection of studies that use orbital remote sensing data to investigate the composition and geologic histories of Mars' moons, Phobos and Deimos, and Mt. Sharp, the destination for the Curiosity Mars rover. A final chapter focuses on Curiosity data and terrestrial analog studies to supplement orbital predictions about Mt. Sharp.

Disk-resolved hyperspectral observations of Phobos acquired at a range of lighting and viewing geometries are fit with a Hapke photometric function to solve for the single particle phase function and single scattering albedos of Phobos and also disk-resolved hyperspectral observations of Deimos. Fe^{2+} electronic absorptions diagnostic of olivine and pyroxene are not detected. A broad absorption centered on 0.65 μm within the red spectral units of both moons is seen, and this feature is also evident in telescopic, Pathfinder, and Phobos-2 observations of Phobos. A 2.8 μm metal-OH combination absorption on both moons is also detected, and this absorption is shallower in the Phobos blue unit than in the Phobos red unit and Deimos. The strength, position, and shape of both absorptions are similar to features seen on low-albedo

primitive asteroids. Two end-member hypotheses could explain these spectral features: the presence of highly desiccated Fe-phyllosilicate minerals indigenous to the bodies, or Rayleigh scattering and absorption of small iron particles formed by exogenic space weathering processing, coupled with implantation of H from solar wind. Phobos' and Deimos' low reflectances, lack of mafic absorption features, and red spectral slopes are incompatible with even highly space weathered chondritic or basaltic compositions. These results, coupled with similarities to laboratory spectra of Tagish Lake (possible D-type asteroid analog) and CM carbonaceous chondrite meteorites, show that Phobos and Deimos have primitive compositions. If the moons formed *in situ* rather than by capture of primitive bodies, primitive materials must have been added to the Martian system during accretion or a late stage impact.

Oversampled visible/near-infrared hyperspectral data over Mt. Sharp in Gale Crater are used to generate spatially sharpened maps of the location of red crystalline hematite within the uppermost stratum of a ~6.5 km long ridge on the mound's northern flank. Emplacement of the hematite is hypothesized to result either from exposure of anoxic Fe^{+2}-rich groundwater to an oxidizing environment or from in place weathering of precursor silicate materials under oxidizing conditions. Although at the time of writing the rover is still ~6 km north of the ridge, high resolution color imaging and low resolution spectral remote sensing data of the ridge collected by Curiosity are consistent with orbital observations. When Curiosity does arrive at the ridge, it is well equipped to distinguish between predicted end-member textural scenarios for ridge materials, which will be essential to understand its formation and evolution.

Chapter 1: Introduction to the Dissertation

The compositions of terrestrial planetary bodies reflect the geologic processes that have shaped them over time. On Mars for example, hydrated silicates are generally found only in the planets' oldest rocks, and this has been interpreted to illustrate a global transition from an early wet Mars that experienced extensive aqueous alteration to the cold and dry Mars of today [*Bibring et al.,* 2006; *Mustard et al.,* 2008]. Gale Crater was selected as the landing site for the Curiosity Mars Rover largely because orbital data showed the ~5 km tall stack of sedimentary material in the crater's center, Mt. Sharp, contains phyllosilicates and sulfates overlain by anhydrous minerals, suggesting this period of dramatic environmental change is preserved in the mound's layers [*Milliken et al.,* 2010; *Thomson et al,* 2011]. Curiosity's detailed surface investigation of Mt. Sharp will reveal a great deal about changing conditions on early Mars, and in turn, the potential for the planet to have supported developing life.

The compositions of Mars' moons, Phobos and Deimos, not only preserve a record of space weathering processes that have modified their surfaces over billions of years, but they are also a direct indicator of the mechanism that formed these bodies. One of the longstanding, unresolved questions of planetary science is whether Phobos and Deimos formed *in situ* around Mars either through co-accretion or giant impact [*Burns,* 1992, *Safronov,* 1986], or if they are captured asteroids that originated from elsewhere in the solar system [*Hunten,* 1979; *Sasaki,* 1990]. The key to unlocking this mystery will be to determine whether the moons are composed of materials expected to be native to the Martian system or if they are made of something more exotic that could only have arrived from another location [e.g. *Murchie et al.,* 2014].

This thesis is a collection of three published chapters that use orbital remote sensing data to investigate the composition and geologic histories of Mars' moons and Mt. Sharp. A fourth

chapter focuses on rover and terrestrial analog data to supplement the orbital predictions about Mt. Sharp. The foundation of this work is based on data collected by two visible to near infrared (VNIR) imaging spectrometers that measure composition remotely and that are currently orbiting Mars: the Observatoire pour la Minéralogie, l'Eau, les Glaces et l'Activité (OMEGA) [*Bibring et al.,* 2004] on ESA's Mars Express mission, and the Compact Reconnaissance Imaging Spectrometer for Mars (CRISM) [*Murchie et al.,* 2007] on NASA's Mars Reconnaissance Orbiter. Over the last ten years, these instruments have collected the highest spatial and spectral resolution datasets of Mars and its moons ever acquired.

Chapters 2 and 3 of this thesis focus on CRISM and OMEGA disk-resolved observations of Phobos and Deimos. At the time these observations were collected, the moons' compositions were poorly constrained despite multiple targeted Earth- and space-based campaigns [*Rivkin et al.,* 2007 and references therein]. Determining Phobos' and Deimos' surface compositions remotely has proven to be challenging in part because spectral observations of the moons are acquired at a variety of lighting conditions, which makes it difficult to compare them to laboratory spectra of well-characterized samples collected under controlled lighting conditions. In Chapter 2, OMEGA data are analyzed to understand how the behavior of the Phobos' spectra change with viewing geometry, and this knowledge is used to model both the CRISM and OMEGA Phobos and Deimos spectra as they would appear in a laboratory setting. The analysis in this chapter robustly demonstrates that Phobos and Deimos likely have primitive compositions because they are spectrally similar to CM carbonaceous chondrites or to the unusual chondrite, Tagish Lake. If the moons formed *in situ* rather than by capture of primitive bodies, primitive materials must therefore have been added to the Martian system during accretion or a late stage impact.

Another reason Phobos' and Deimos' composition is difficult to ascertain remotely is because their spectra lack strong diagnostic absorptions. In chapter 3, two subtle absorption features that were detected for the first time using the high-resolution CRISM observations are discussed. The strength, position, and shape of both absorptions are similar to features seen on red-sloped, low-albedo primitive asteroids, which is consistent with the moons' having primitive compositions. Two end-member hypotheses are presented to explain the specific phases that are likely causing these features; the first invokes the presence of highly desiccated Fe-phyllosilicate minerals indigenous to the bodies, and the second appeals to small iron particles formed by exogenic space weathering processing coupled with implantation of H from solar wind. Both end-member hypotheses may play a role,and *in situ* exploration will be needed to ultimately determine the underlying causes for this pair of spectral features.

Chapters 4 and 5 shift to a discussion of the composition of materials in Gale Crater on Mars, specifically focusing on the mapping and implications of a hematite-bearing layer located near the bottom of Mt. Sharp. In Chapter 4, a new technique for collecting CRISM data at spatial resolutions up to 3x higher than initially used to map minerals in Mt. Sharp is developed, and one of the first discoveries made from these high spatial resolution data, that crystalline hematite is closely associated with a ridge in lower Mt. Sharp, is discussed. The mapping detail afforded by the increased spatial resolution CRISM data leads to the development of two hypotheses about the formation mechanisms for this highly localized hematite deposit, and both scenarios imply that the ridge may be a previously habitable environment. The ridge is now considered a high priority target for future investigation by Curiosity because of the results discussed in this chapter [*Grotzinger et al.,* 2014].

Chapter 5 is not designed to be submitted for publication as it is written in this thesis, but

it will be presented to the Curiosity science team to help with initial strategic planning and to provide a basis for subsequent team discussion when Curiosity approaches the hematite ridge. This chapter is focused on observations Curiosity has made and will make of the ridge to supplement the orbital observations. Although at the time of writing the rover is still ~6 km to the north of the ridge, high resolution color imaging and low resolution spectral remote sensing data of the ridge collected by Curiosity are consistent with the orbital observations described in Chapter 4. Once Curiosity does reach Mt. Sharp, strategic path planning to reach the hematite-rich ridge top will be necessary to find a traversable route that provides access to the most scientifically rewarding targets. A future detailed *in situ* campaign is proposed based on analyses of orbital data, investigations of terrestrial iron oxide and oxyhydroxide samples, and previous experience of Curiosity's investigations at Yellowknife Bay [*Grotzinger et al.,* 2014].

The work in these chapters was led by A. A. Fraeman with guidance from her academic advisor, R. E. Arvidson. Specific inputs from additional co-author were as follows:

- Chapter 2: S. Murchie provided the CRISM dataset, extensive discussions, and significant input to the text, A. Rivkin helped with extensive discussions, J-P. Bibring and B. Gondet provided the OMEGA dataset and discussion, D. Humm helped calibrate the CRISM observations, T. Choo calculated viewing geometries for the CRISM observations, N. Manaud calculated viewing geometries for the OMEGA observations, and R. Kuzmin and E. Zabalueva provided results from thermal models of Phobos' surface that corresponded with the CRISM and OMEGA observations.
- Chapter 3: S. Murchie provided extensive discussion, significant input for the text, and was the first to report the discovery of a 0.65 μm feature, R. Clark

provided extensive discussion, the radiative transfer models of nanophase iron to reproduce the 0.65 μm feature, and methods for surface temperature estimation, R. Morris provided extensive discussion, input for the text, and libraries of laboratory spectra for comparison to the 0.65 μm feature, and A. Rivkin and F. Vilas provided discussion about asteroid spectra.

- Chapter 4: J. Catalano provided extensive discussion about geochemical processes responsible for hematite formation and inputs to the text, R. Morris provided extensive discussion, input to the text, and his spectral library of well-characterized iron oxides, J. Grotzinger and S. Murchie contributed to general discussion, K. Stack calculated strike and dip measurements, J. McGovern was instrumental in helping to develop the CRISM oversampling scheme, and F. Seelos, K. Seelos, and C. Viviano provided discussion and improvements in CRISM parameter mapping.

Chapter 2 has been published in the *Journal of Geophysical Research* [*Fraeman et al.*, 2012], Chapter 3 has been published in *Icarus* [*Fraeman et al.*, 2014], and Chapter 4 has been published in *Geology* [*Fraeman et al.*, 2013].

REFERENCES CITED

Bibring, J-P. et al., 2004. "OMEGA: Observatoire pour la Minéralogie, l'Eau, les Glaces et l'Activité," *Mars Express: the scientific payload,* edited by A. Wilson, *Eur. Space Agency Spec. Publ.1240,* 37-39.

Bibring, J-P. et al., 2006. "Global Mineralogical and Aqueous Mars History Derived from OMEGA/Mars Express Data," *Science*, 312, 5772, 400-404. doi:10.1126/science.1122659.

Burns, J. A., 1992. "Contradictory clues as to the origin of the Martian moons," *Mars*, edited by H. Kieffer, B. Jakosky, C. Snyder, M. Matthews, Univ. Arizona Press, Tuscon, 1283–1301.

Fraeman, A., Arvidson, R., Murchie, S., Rivkin, A., Bibring, J-P., Choo, T., Gondet, B., Humm, D., Kuzmin, D., Manaud, N., Zabalueva, E., 2012. "Analysis of disk-resolved OMEGA and CRISM spectral observations of Phobos and Deimos," *Journal of Geophysical Research*, 117, doi:10.1029/2012JE004137.

Fraeman, A., Arvidson, R., Catalano, J., Grotzinger, J., Morris, R., Murchie, S., Seelos, F., Seelos, K., McGovern, J., Humm, D., Stack, K., Viviano, C., 2013. "A hematite-bearing layer in Gale Crater: mapping and implications for past aqueous conditions," *Geology*, 41, 1103-1106. doi:10.1130/G43613.1.

Fraeman, A., Murchie, S., Arvidson, R., Clark, R., Morris, R., Rivkin, A., Vilas, F., 2014. "Spectral absorptions on Phobos and Deimos in the visible/near infrared wavelengths and their compositional constraints," *Icarus*, 229, 196-205, doi: 10.1016/j.icarus.2013.11.021.

Grotzinger, J., et al., 2014. "A Habitable Fluvio-Lacustrine Environment at Yellowknife Bay, Gale Crater, Mars," *Science*, 343, 6169. doi:10.1126/science.1242777.

Hunten, D. M. 1979. “Capture of Phobos and Deimos by photoatmospheric drag,” *Icarus*, *37*, 113–123, doi:10.1016/0019-1035(79)90119-2.

Milliken, R.E., Grotzinger, J.P., Thomson, B.J., 2010. “Paleoclimate of Mars as captured by the stratigraphic record in Gale Crater,” *Geophysical Research Letters*, v. 37, doi:201010.1029/2009GL041870.

Murchie, S. et al., 2007. “Compact Reconnaissance Imaging Spectrometer for Mars (CRISM) on Mars Reconnaissance Orbiter (MRO),” *J. Geophys. Res.*, *112*, E05S03, doi:200710.1029/2006JE002682.

Murchie, S., Eng., D., Chabot, N., Guo, Y., Arvidson, R., Yen, A., Trebi-Ollennu, A., Seelos, F., Adams, E., Fountain, G., 2014. “MERLIN: Mars-Moons exploration, reconnaissance and landed investigation,” *Acta Astronautica* 93, 475-482. doi: 10.1016/j.actaastro.2012.10.014.

Mustard, J. et al., 2008. “Hydrated silicate minerals on Mars observed by the Mars Reconnaissance Orbiter CRISM instrument,” *Nature*, 454, 305-309. doi:10.1038/nature07097.

Rivkin, A.S., 2007. “The Composition of Phobos and Deimos: Constraints and Questions,” *Workshop on the Exploration of Phobos and Deimos*, abstract #7022.

Safronov, V. S., Pechernikova, G. V., Ruskol, E. L., and Vitjazev, A. V., 1986. “Protosatellite swarms,” *Satellites*. J. A. Burns and M. S. Matthews, editors. University of Arizona Press, Tucson, AZ, pp. 89–116.

Sasaki, S., 1990. “Origin of Phobos: Aerodynamic drag capture by the primary atmosphere of Mars,” *Lunar Planet. Sci. Conference 21*, abstract #1069.

Thomson, B.J., Bridges, N.T., Milliken, R., Baldridge, A., Hook, S.J., Crowley, J.K., Marion, G.M., De Souza Filho, C.R., Brown, A.J., and Weitz, C.M., 2011. "Constraints on the origin and evolution of the layered mound in Gale Crater, Mars using Mars Reconnaissance Orbiter data," *Icarus*, v. 214, p. 413–432, doi:10.1016/j.icarus.2011.05.002.

Chapter 2: Analysis of Disk-Resolved OMEGA and CRISM Spectral Observations of Phobos and Deimos

Associated Publication: Fraeman, A., Arvidson, R., Murchie, S., Rivkin, A., Bibring, J-P. Choo, T., Gondet, B., Humm, D., Kuzmin, R., Manaud, N., Zabalueva, E. 2012. "Analysis of disk-resolved OMEGA and CRISM spectral observations of Phobos and Deimos," *Journal of Geophysical Research*, 117, doi:10.1029/2012JE004137.

ABSTRACT

Disk-resolved observations of Phobos acquired by OMEGA at a range of lighting and viewing geometries were fit with the Hapke photometric function to solve for the single particle phase function and single scattering albedos from 0.4 to 2.5 μm. Single scattering albedos were recovered from CRISM observations of Phobos using the OMEGA derived single particle phase function and are similar to those from OMEGA data. Both the ubiquitous red unit and the blue unit around the crater Stickney exhibit a smooth red-sloped spectrum, with a steeper continuum in the redder unit. Single scattering albedos retrieved from CRISM measurements of Deimos are similar to those for the red unit on Phobos. Retrieval of single scattering albedos from OMEGA data at 2.8 to 5.0 μm has greater uncertainty, but results in this wavelength range are also consistent with a smooth, red-sloped spectrum. Phobos' and Deimos' low reflectances, lack of mafic absorption features, and red spectral slopes are incompatible with even highly space weathered chondritic or basaltic compositions. These results, coupled with similarities to laboratory spectra of Tagish Lake (possible D-type asteroid analog) and CM carbonaceous chondrite meteorites, show that Phobos and Deimos have primitive compositions. If the moons formed *in situ* rather than by capture of primitive bodies, primitive materials must have been added to the Martian system during accretion or a late stage impact.

2.1 INTRODUCTION

Mars' moons Phobos and Deimos are small, irregularly shaped, low-density bodies with low albedos and spectra similar to D-type asteroids common in the outer main asteroid belt and outer solar system [e.g. *Burns*, 1992; *Murchie and Erard*, 1996; *Rivkin et al.*, 2002 and references therein]. The compositions of Phobos and Deimos are poorly understood, although proposed formation mechanisms for the moons can help constrain their probable make-up. There are two main classes of models to explain the origin of the Martian moons: capture or formation in Mars orbit. Capture of dark, low-density objects from the outer solar system [*Burns*, 1978; *Hartmann*, 1990] would explain Phobos' and Deimos' low densities and albedos, but this scenario is considered unlikely given that dynamical models for capture require specific conditions, including aerodynamic drag by an early Mars proto-atmosphere [*Hunten*, 1979; *Sasaki*, 1990]. If they are captured bodies, the moons' orbits are also difficult to explain dynamically because both are circular; Phobos spirals toward Mars, while Deimos spirals out. In his review of orbital constraints on the moons' origins, *Burns* [1992] concluded that formation *in situ* was favored dynamically. *In situ* formation hypotheses include formation by co-accretion with Mars [*Safronov et al*., 1986] and formation resulting from a giant impact on Mars [*Craddock*, 2011].

Together, these origin hypotheses result in Phobos and Deimos having one of three likely compositions: (1) primitive, undifferentiated compositions dominated by phyllosilicates with C-containing phases, similar to CM-type carbonaceous chondrites [*Brearley and Jones*, 1998] or to the more primitive Tagish Lake meteorite, commonly thought to be a compositional analog to D-type asteroids [*Brown et al.*, 2000; *Hiroi et al.*, 2001], (2) compositions resembling pre-differentiated, bulk Mars, which is expected to be mainly composed of ordinary chondrites with

a minor carbonaceous chondrite component and dominated by olivine and pyroxene minerals [*Lodders and Fegley,* 1998], or (3) basaltic compositions similar to the Martian crust and upper mantle, also dominated by olivine and pyroxene minerals.

In this chapter, we evaluate the compositions of Phobos and Deimos using disk-resolved imaging spectrometer measurements of Phobos covering 0.4 to 5.0 μm acquired by the Observatoire pour la Mineralogie, l'Eau, les Glaces et l'Activité (OMEGA) onboard Mars Express (MEx) [*Bibring et al.*, 2004], and measurements of both moons covering 0.4 to 2.7 μm acquired by the Compact Reconnaissance Imaging Spectrometer for Mars (CRISM) on Mars Reconnaissance Orbiter (MRO) [*Murchie et al.*, 2007]. Although CRISM data extend to 3.9 μm, we restrict our CRISM analyses to shorter wavelengths pending resolution of radiometric calibration artifacts at longer wavelengths [*Murchie et al.*, 2009]. OMEGA observations of Phobos acquired at a range of lighting and viewing conditions for Phobos are used to retrieve single scattering albedos and single particle phase functions using the Hapke photometric function [*Hapke*, 1993]. These functions are then used to simulate single scattering albedo values for CRISM observations to directly compare the two data sets and to determine if Deimos has similar spectral properties as Phobos. Finally, we compare the moons with telescopic and laboratory spectra in order to assess proposed compositions and discuss implications.

2.2 Overview of Data Sets

OMEGA is a suite of three spectrometers: a visible (V) channel (0.35 μm to 1 μm), a short wavelength infrared (SWIR-C) channel (1 μm to 2.5 μm), and a medium wavelength infrared L (SWIR-L) channel (~2.8 μm to 5 μm) [*Bibring et al.*, 2004]. OMEGA acquired ten disk-resolved observations of Phobos over a period from May 2004 through January 2011 (Table 2.1), six of which contain high-quality data in both the V and C channels. The remaining four

observations are either V-only or were taken late in the instrument's lifetime and contain a number of degraded spectral channels within the C channel. The OMEGA measurements of Phobos have spatial sampling from 120 m/pixel to 2200 m/pixel and provide broad coverage of both the sub- and anti-Mars hemispheres of Phobos (Fig. 2.1). In addition, High Resolution Stereo Camera (HRSC) images acquired in conjunction with the OMEGA observations provide morphologic context for the OMEGA observations (Table 2.1, Fig. 2.1).

CRISM is a suite of two high spatial resolution spectrometers, a visible/near-infrared (VNIR) channel from 0.4 to 1.0 μm and an infrared (IR) channel from 1.0 to 3.9 μm, both have spectral resolutions of ~6.55 nm/channel [*Murchie et al.*, 2007]. The CRISM Phobos dataset consists of three observations acquired in succession on 23 October 2007 at an average phase angle of 41°, spatial sampling of 350 m/pixel, and covering approximately the same region in the western side of Phobos' sub-Mars hemisphere (Table 2.1, Fig. 2.2) [*Murchie et al.*, 2008]. HiRISE observations provide high-resolution spatial context for the CRISM data, although the HiRISE data were not acquired in coordination with the CRISM data (Table 2.1, Fig. 2.2) [*Thomas et al.*, 2011].

Previous work shows that there are two color or spectral units exposed on Phobos, a red and a blue unit [e.g. *Murchie and Erard*, 1996; *Rivkin et al.*, 2002]. The red unit covers most of the surface of the moon and is characterized by low overall albedo and a red spectral slope. The blue unit is exposed on and near the 9-km diameter crater Stickney and has spectral properties similar to the ubiquitous red unit, but with a less red spectral slope. Regions of interest (ROIs) within these two units and in Stickney crater are shown in figures 2.3 and 2.4.

To utilize both the CRISM and OMEGA data sets over as much of their spectral range as possible, we need to explicitly model the spectrophotometry and both the reflected solar and

emitted thermal radiation. For example, Fig. 2.3 shows averaged radiance spectra from OMEGA data between 0.4 to 5.0 μm covering portions of the same region on the sub-Mars hemisphere of Phobos. For illustrative purposes, scattered solar irradiance is plotted assuming a Lambert Albedo of 0.05, and thermal emission is shown for a selection of surface kinetic temperatures within the range predicted using models by *Kuzmin and Zabalueva* [2003] for the times and locations of the OMEGA observation. These relatively simple approximations to the spectral radiances for Phobos demonstrate that the transition between solar scattered light and emission dominated spectra occurs longwards of ~2.7 μm. At these longer wavelengths spectrophotometric models must account for the presence of both scattered solar irradiance and thermal emission. It is thus appropriate to begin the analyses using the OMEGA V and C data (0.4 to 2.5 μm) and to then separately turn attention to the L data (2.8 to 5.0 μm).

Fig. 2.4 shows I/F spectra (radiance/(solar irradiance/π)) for OMEGA and CRISM data of approximately the same regions on Phobos. The spectra from the CRISM observation are brighter than spectra from the OMEGA observations because the CRISM data were acquired at a lower phase angle (41°) than the OMEGA observation (63°), and the surface of Phobos is known to be backscattering and thus darkens with increasing phase angle [*Simonelli et al.*, 1998]. Both sets of spectra brighten nearly monotonically with increasing wavelength and exhibit a large thermal emission at longer wavelengths, consistent with radiance spectra shown in Fig. 2.3. Marsshine is present in the sub-Mars facing data for OMEGA data (CRISM observations were taken on the night side of Mars); based on analyses by *Goguen et al.*, [1979], Marsshine in the OMEGA observations is only at most few percent of the radiance and to first order can be ignored.

CRISM collected for the first time spatially resolved imaging spectrometer measurements of Deimos in June 2007 [*Murchie et al.*, 2008]. Three successive data sets were acquired covering the sub-Martian hemisphere of Deimos at an average phase angle of 22° with a spatial sampling ~1.2 km/pixel (Fig. 2.5). Because these observations were taken when Deimos was over the night side of Mars, Marsshine has a negligible contribution to the measured radiance. Fig. 2.6 shows the average I/F spectrum from the middle CRISM Deimos observation. There is very little spectral variation from pixel to pixel within this observation except for spatially varying thermal emission. The I/F increases nearly monotonically with wavelength and is similar in magnitude to the I/F spectra of Phobos. As noted previously, here we restrict retrieval of spectrophotometric properties for CRISM data to wavelengths <2.7 μm; inclusion of longer wavelength data in Fig. 2.6 is illustrative and not meant to be quantitative.

2.3 Retrieval of Spectrophotometric Properties

2.3.1 Overview

The broad phase angle coverage of the six OMEGA Phobos observations (Table 2.1) allows us to derive spectrophotometric parameters for the V and C channels. OMEGA I/F, equivalent to radiance factor *r*, may be modeled using Hapke's equation for bidirectional radiance and directional emissivity expressed as a function of incidence angle *i*, emission angle *e*, phase angle α, and kinetic temperature *T*, in the following manner for a given wavelength:

$$r(i,e,\alpha,T) = \frac{w}{4}\frac{\mu_{0e}}{\mu_{0e}+\mu_e}\left[\left(1+B(\alpha)\right)p(\alpha,g_1) + H(w,\mu_{0e})H(w,\mu_e) - 1\right]S(i,e,\alpha,\theta) + \sqrt{1-w}\cdot H(w,\mu)\cdot\frac{\beta_0(T)}{J/\pi} \quad (2.1)$$

where w is the average single scattering albedo, μ is the cosine of the emergence angle, μ_e and μ_{0e} are the effective cosines of the emergence and incidence angles respectively, $B(\alpha)$ models the opposition-effect, $p(g_1)$ is the single particle phase function, H is an approximation for the isotropic multiple scattering function, and S is the shadowing function defined by a macroscopic roughness parameter, θ [*Hapke*, 1993]. In addition, β_0 is the Planck irradiance at a given temperature T and J is the solar irradiance at the solar distance at the time of observation [*Hapke*, 2005].

The one-term Henyey-Greenstein single particle phase function is dependent only on phase angle and one asymmetry parameter, g_1, as

$$p(\alpha, g_1) = \frac{1-g_1^2}{(1+2g_1\cos(\alpha)+g^2)^{3/2}} \tag{2.2}$$

In this form, negative values of g_1 are associated with backscattering material and positive values indicate forward scattering material. We choose to fit the data using the one-term Henyey-Greenstein function rather than a more complex phase function in order to keep the number of parameters to be fit at the minimum possible. The lack of low phase angle observations did not allow us to constrain parameters associated with the opposition surge, B_0 and h, so we adopted the best fit values derived from Viking clear-filter data of 5.7 and 0.072 respectively [*Simonelli et al.*, 1998]. This selection has a minimal effect on the derived best-fit parameters as all parameters are derived using phase angles greater than 35 degrees. The opposition surge is most influential for observations at very small phase angles, less than ~15 degrees.

2.3.2 Solar-dominated regime

Our approach was first to solve Equation 1 over the spectral region dominated by scattered solar radiation, i.e., using data from the V and C channels. For the six OMEGA observations we searched for the values of w, g_1, and θ that would provide the best global average fit for the surface of Phobos at selected wavelengths. A total of 38 spectra were selected from each observation (the maximum number allowed given the observation with the fewest available spectra), and the IDL subroutine MPFIT was used to find the combination of w, g_1, and θ values that best fit all of data at each selected wavelength. The incidence and emergence angles for each spectrum used in the fit are presented in Fig 2.7, phase angles for the six observations are listed in Table 2.1. Note that these fits are for all OMEGA data and thus should be most relevant to the aerially dominant red unit surfaces.

MPFIT is a non-linear, least squares fitting function based on the Levenberg-Marquardt algorithm [*Moré*, 1978; *Markwardt*, 2009]. This algorithm searches through a space of chi-square values beginning with a set of initial parameter guesses and finds the parameter combination associated with a local minimum in this chi-square parameter space by following the steepest gradient in the space. Because different values of initial conditions may converge on local minima chi-square values rather than the absolute minimum, we ran the models multiple times using systematically varying initial values to ensure the resultant best-fit parameters truly represented the absolute minimum chi-square value rather than a local minimum. The absolute best-fit parameters are those with the smallest chi-square values.

Since the roughness parameter, θ, should be independent of wavelength, this value was determined by first letting it vary freely at each selected wavelength. We found an average best-fit θ value of 14° over all wavelengths and subsequently held θ fixed at this value while each

wavelength was re-run with only w and g_1 free to vary. We did not attempt to constrain temperature as the contribution of thermal emission is negligible in the solar dominated wavelength regime, i.e. $\beta_0(T,\lambda) \sim 0$ for all reasonable surface temperatures. One-sigma uncertainty values were assigned to the best-fit w and g_1 values using a routine described by [*Cord et al.*, 2003] and adopted by [*Johnson et al.*, 2006]. In this method, the parameter of interest is held fixed in a series of values moving away from the best-fit value while other parameters are allowed to vary freely. The one-sigma confidence level occurs when the resulting chi-square of the best-fit model has doubled from its original value. In our case, the opposition surge parameters B_0 and h and roughness parameter θ were assumed to be fixed, so the only parameters allowed to vary were either w or g_1. For a well-constrained parameter the chi-square value increases quickly as that parameter is forced to move away from its best-fit value. Conversely, changing the values of a poorly constrained parameter will result in only a gradual increase of chi-square values. For a more detailed description and validation of this method see [*Cord et al.*, 2003] and [*Johnson et al.*, 2006].

Fig. 2.8 shows the wavelength-dependent, global average best-fit values for single scattering albedo for Phobos at selected wavelengths. Single scattering albedos increase monotonically with wavelength, beginning with values of ~0.05 at 0.45 μm and increasing to ~0.15 at 2.5 μm. The results at shorter wavelengths are consistent with previous photometric studies based on clear-filter Viking data centered at 0.54 μm and Hubble Space Telescope observations from 0.41-1.042 μm [*Simonelli et al.*, 1998; *Cantor et al.*, 1999]. The best-fit asymmetry parameter was found to be wavelength independent, with a value of -0.28±0.3, indicative of a backscattering surface. The phase function is most sensitive to changing g_1 values for phase angles ≤50° and ≥100° [*Helfenstein and Veverka*, 1989] whereas four of the six

OMEGA observations analyzed were made at phase angles between 50° to 100° (Table 2.1). Thus the large uncertainty in estimating g_1 is not unexpected. We note that regolith-covered planetary surfaces have been modeled using values of g_1 between -0.20 and -0.40 [e.g., *Clark et al.*, 2002a], providing assurance that our results are reasonable.

The ability of the Hapke Function to model the OMEGA and CRISM data for the Phobos red unit is shown in Fig. 2.9. Here spectra of similar regions in both data sets have been recast to single scattering albedo by solving equation 2.1 using measured I/F values, known viewing geometries, and the OMEGA derived best fit phase function and roughness parameter. The similarity in the single scattering albedo spectra indicates that the two instruments provide comparable measurements of sunlight scattered from the surface and that the photometric model represents how light is scattered as a function of lighting and viewing geometries to within stated formal uncertainties. Given that we have derived a global spectrophotometric model of Phobos from OMEGA data that also works for CRISM data and that previous photometry studies have suggested Phobos and Deimos have similar photometric behavior [*Thomas et al.*, 1996; *Simonelli et al.*, 1998], we can therefore also recast the CRISM Deimos data into single scattering albedo values. Results indicate that Deimos is indeed similar to the red unit that dominates the surface of Phobos.

2.3.3. Mixed solar and thermal regimes

The addition of a thermal emission component introduces another unknown (i.e., surface kinetic temperature) into the Hapke Function and makes it impossible to continue to solve for global-average Hapke parameters in OMEGA data at >2.6 μm in the L channel because of pixel-to-pixel temperature variations. These difficulties are evident in inspection of the radiance spectra in Fig. 2.3 in which emission from Phobos produces spectra that are shallower than

spectrally neutral graybody emitters. Either the single scattering albedos increase in magnitude in the wavelength range of the L channel or the OMEGA pixels sample surfaces with spatially non-uniform temperatures. In order to work with OMEGA data in this region, we assume that the global-average wavelength independent Hapke parameters found at shorter wavelengths remain constant up to 5 μm. This simplification reduces the unknown quantities to single scattering albedo and surface temperature, assuming that each pixel's radiance can be modeled as resulting from a single surface kinetic temperature.

We begin our retrieval of single scattering albedos with estimates of the surface temperatures expected in the OMEGA observations using a thermal model of the surface of Phobos [*Kuzmin and Zabalueva*, 2003]. This model takes into account the ellipsoidal shape of Phobos, eclipses of Phobos by Mars, reflected thermal radiation from Mars, and the absence of internal heat sources. The model uses an average Phobos albedo of 0.07 (consistent with our average retrieval in the solar-dominated region of the spectrum), a surface regolith density of 1100 kg m^3, and temperature-dependent thermal conductivity and specific heat equations that are analogous to lunar regolith. Emission is assumed to be blackbody and directionally uniform. The approach we used was to solve for spectral single scattering albedo and examine the retrieved spectra with the realization that albedos need to be within the bounds between 0 and 1. Single scattering albedo retrievals were found to be particularly noisy around the thermal cross over where solar reflected radiance and thermal emission become equal. The exact wavelength depends on the surface kinetic temperature and lighting and viewing geometries, with a typical value of ~4.5 μm. Retrievals longward of the cross over wavelength were very noisy indeed (Fig. 2.10). The inability to retrieve precision spectra in the mixed solar and thermal regime is not surprising given the uncertainties in the model used and the complex shape of Phobos as

compared to the shape model used to compute the thermal emission. Our best estimate is that the single scattering albedos continue to increase in magnitude (i.e., redden with a increasing wavelength) to at least ~4.5 μm, but this result is notional and we do not attempt quantitative analyses of the spectral range from 2.6 to 4.5 μm.

2.4 Analysis of Phobos and Deimos Spectra

Single scattering albedo data for Phobos and Deimos are shown in Fig. 2.11 for the blue and red units and for the average of the CRISM Deimos observation. OMEGA data for this particular observation, ORB0756_0, show a peculiar concave downward V spectrum that becomes more pronounced toward the upper left of the data frame. We suspect this is a calibration artifact. Otherwise the results for the two instruments are similar indeed and consistent with the limited earlier observations [e.g. *Murchie and Erard*, 1996; *Rivkin et al.*, 2002] in that the two moons have very low single scattering albedos and red slope.

2.4.1 Search for spectral absorption features

Results from the Phobos-2 Imaging Spectrometer for Mars (ISM) were interpreted as indicating the presence of olivine and pyroxene on Phobos [*Murchie and Erard*, 1996; *Gendrin et al.*, 2005], and these minerals are expected to be present if Phobos and Deimos have chronditic or basaltic compositions. We have therefore specifically searched for these features in the CRISM and OMEGA single scattering albedo spectra by generating the standard mafic mineral summary parameter maps that are commonly used in analysis of OMEGA and CRISM observations of Mars [*Mustard et al.*, 2005; *Loizeau et al.*, 2007; *Pelkey et al.*, 2007]. These summary parameters are sensitive to the broad absorptions around 1 and 2 μm caused by iron related crystal field transitions in both minerals. The resulting parameter maps designed to highlight the presence of olivine and low- and high-calcium pyroxene show little or no indication

for any of these minerals, and we conclude that there is no evidence for mafic mineral absorption features above a few percent, the level of instrument noise. This discussion is expanded for the CRISM dataset only Chapter 3.

Analyses of the CRISM Phobos and Deimos I/F observations also revealed the presence of a broad, shallow absorption feature centered near 0.65 μm in the redder unit of Phobos and on Deimos [*Murchie et al.*, 2008]. Again, we leave a more thorough discussion of this CRISM-based detection to Chapter 3 in which we expand on the initial discovery and place limits on the possible causes of this broad feature.

2.4.2 Comparisons to laboratory spectra

Given our knowledge of Phobos and Deimos spectrophotometry, we can model the spectra to simulate the lighting and viewing conditions as they would appear for laboratory spectra. The bidirectional reflectance measurements provided in the RELAB database may be expressed using the Hapke model for radiance coefficient as [*Hapke*,1993]

$$rc(i,e,\alpha) = \frac{w}{4}\frac{1}{\mu_{0e}+\mu_e}\left[\left(1+B(\alpha)\right)p(\alpha,g_1) + H(w,\mu_{0e})H(w,\mu_e) - 1\right]S(i,e,\alpha,\theta) \quad (2.3)$$

The ability to model OMEGA and CRISM data as laboratory spectra allows us for the first time to directly compare the slope and absolute magnitudes of the Phobos and Deimos spectra to lab data without the need for scaling, and this is an important diagnostic tool given the lack of obvious mineralogical absorption features in the moons' spectra.

Fig. 2.12 (top left) shows CRISM blue unit spectra from Stickney's interior and ejecta modeled as bidirectional radiance coefficients at i = 30˚ along with three meteorite analogs that were also observed at i = 30º. We found analogs by searching through libraries of dark,

relatively featureless spectra, including highly space weathered lunar material, CI chondrites, and CM chondrites. By visual inspection, the best match meteorite analogs have primitive, CM carbonaceous chondrite-like compositions (Murchison and Mighei) and an ultraprimitive, D-asteroid analog composition (Tagish Lake). All three are close matches to the slope and absolute magnitude of the Phobos blue unit spectrum. The closest meteorite analog is 0-63 μm particles from Murchison, a typical CM chondrite, that have been heated to 700˚ C for one week [*Hiroi et al.*, 1993]. Before heating, Murchison was dominantly composed of Mg-serpentine and Fe-bearing serpentine-group mineral cronstedtite and sulfide mineral tochilinite, with smaller amounts of olivine, clinoenstatite, and pyrrhotite [*Bland et al.*, 2004]. As a result of heating beyond 600˚ C, the serpentines began to dehydrate and recrystallize as olivine while iron-rich orthopyroxenes and tochilinite had been converted to troilite [*Hiroi et al.*, 1993]. The featureless heated Murchison spectrum has a similar slope to spectra from Stickney's interior and ejecta, and in particular, has a similar absolute magnitude with the Stickney ejecta spectrum.

Another closely matched spectral candidate to the blue unit is for 0 - 45 μm bulk particles from the CM chondrite Mighei. This meteorite has a similar composition to the unheated Murchison but a higher Fe/(Fe+Mg) ratio [*Cloutis et al.*, 2011]. The Mighei spectrum has a similar brightness and slope to the Phobos blue unit, although it does show absorption features near 0.4 μm and 0.7 μm that are not observed in the Phobos blue spectra. The steep drop off near 0.4 μm is found in many unheated CM chondrite spectra and is attributed to phyllosilicates, magnetite, or organics [*Cloutis et al.*, 2011]. The fact that this feature is not observed in the CRISM spectra may be due to unreliable data shorter than 0.44 μm. The shallow, broad absorption centered near 0.7 μm is attributed to mixed valence Fe-bearing serpentine group phyllosilicates [*Cloutis et al.*, 2011].

The Tagish Lake meteorite has been interpreted as a sample from the ultra-primitive D-type asteroids from the outer solar system [*Hiroi et al.*, 2001]. This meteorite is a carbon-rich, aqueously altered unusual carbonaceous chondrite with high concentrations of presolar grains and carbonate minerals [*Hiroi et al.*, 2001]. The spectrum of Tagish Lake has an absolute reflectance consistent with the spectrum from Stickney's interior and no visible absorption features, although its slope deviates at the longer wavelengths and is not as good a fit as the CM chondrite spectra.

The closest match analog spectra to the Phobos red unit and Deimos in terms of slope and absolute magnitude are also CM chondrites (Fig. 2.12, top right). Unlike the Phobos blue unit, no laboratory analogs were found that perfectly match the slope and absolute magnitude of red unit spectra, although a few are quite close. Particles <40 μm from a bulk Mighei sample were a good match, as well as particles <125 μm from the CM Chondrite Cold Bokkeveld. Like Mighei, Cold Bokkeveld is large CM chondrite with little terrestrial alteration. The two samples have similar modal volume of the abundant mineral phases Mg-serpentine and Fe-cronstedtite [*Cloutis et al.*, 2011], and these phases are evident in the broad, shallow features near 0.4 μm and 0.7 μm. These features are not observed in the CRISM and OMEGA spectra.

2.4.3 Effects of space weathering

In the case of airless bodies like Phobos and Deimos, any comparison to laboratory analogs based on the magnitude and slope of spectra is confounded by the fact that we are unable to fully quantify the role space weathering has played in modifying Phobos and Deimos. Space weathering is defined by *Clark et al.* [2002b] as processes that modify the traits (including spectral properties) of an airless body's surface from analogous traits of the body's inherent bulk materials. The processes we expect to cause space weathering on Phobos and Deimos include

micrometeorite impact and solar wind ion implantation and sputtering. Analysis of lunar samples has shown that these processes form reduced, submicroscopic iron particles (SMFe) infused throughout mineral grains and glasses [e.g. *Pieters et al.*, 2000; *Hapke*, 2001; *Noble et al.*, 2001; *Taylor et al.*, 2001; *Noble et al.*, 2007; *Lucey and Noble*, 2008] The addition of SMFe particles influences the VNIR spectral properties of a surface by reducing the strengths of absorption features and modifying spectral slope and magnitude. SMFe particles smaller than ~50 nm both darken and redden the surface while particles larger than ~50 nm just darken the surface [*Noble et al.*, 2007; *Lucey and Noble*, 2008; *Lucey and Riner*, 2011].

While space weathering can darken a surface, it is difficult to explain the dark nature of Phobos and Deimos through space weathering alone if the inherent compositions of the moons are similar to ordinary chondrites (similar to bulk Mars) or basaltic or ultramafic material (similar to Martian crust and upper mantle). The most mature, darkest lunar mare spectra collected by the Moon Mineralogy Mapper (M3) [*Green et al.*, 2011] are brighter than Phobos and Deimos when corrected to the same viewing geometries ($i = \alpha = 30^o$, $e = 0^o$) (Fig. 2.12, bottom left). Even in the intense space weathering environment at Mercury, average I/F spectra collected from the Mercury Atmospheric and Surface Composition Spectrometer (MASCS) [*Izenberg et al.*, 2012] are substantially brighter that Phobos and Deimos I/F spectra modeled at the same viewing geometry ($i = e = 45^o$, $\alpha = 90^o$) (Fig. 2.12, bottom right). Although the space-weathering environment around Phobos and Deimos is poorly understood, it is difficult to argue that Phobos and Deimos would have a more intense space weathering environment than Mercury. The moons of Mars are intrinsically dark and are better fit by spectra from primitive meteorite analogs than by space weathered basaltic soils (Fig. 2.12). .

2.5 SUMMARY AND CONCLUSIONS

Disk-resolved observations of Phobos from six OMEGA observations acquired at a range of lighting and viewing geometries were analyzed with the Hapke photometric function to solve for the single particle phase function and single scattering albedos from 0.4 to 2.5 μm, the spectral region covered by OMEGA V and C channel data. Single scattering albedos recovered from CRISM observations of Phobos using the OMEGA single particle phase function are similar to those retrieved from OMEGA data for the same areas, both for the ubiquitous red unit and for the blue unit exposed in and around the crater Stickney. In addition, CRISM-based single scattering albedos retrieved for Deimos are similar to those for the dominant red unit on Phobos. Retrieval of single scattering albedos for OMEGA L data (2.8 to 5.0 μm) is problematic at this time due to the presence of both reflected solar and thermal emission signatures together with the complex shape of Phobos, although we infer that the single scattering albedo spectra continue to have low values and red slopes.

The low single scattering albedos and red slopes are consistent with previous studies that indicate primitive compositions for the two moons. Mafic mineral absorptions are absent. Recasting the spectra for Phobos and Deimos to laboratory lighting and viewing conditions shows that the spectra are very similar to laboratory spectra of Tagish Lake (D-type asteroid meteorite analog) and CM carbonaceous chrondrite meteorites. The spectral properties of Phobos and Deimos are inconsistent with (1) a chondritic composition similar to bulk Mars or (2) a basaltic composition similar to differentiated Martian crust and upper mantle. Even extensive space weathering does not appear to be sufficient to darken and redden chondritic or basaltic composition materials to produce the spectral characteristics of the two moons.

Phobos and Deimos could be primitive objects from the outer solar system captured into Martian orbit, although dynamical models for capture require special and improbable conditions [*Hunten*, 1979; *Sasaki*, 1990]. Conversely, formation of bodies with primitive materials is not currently accounted for in *in situ* formation models [*Safronov* et al., 1986; *Craddock*, 2011]. Thus, future dynamical models of the formation of the moons should specifically account for the primitive character of these bodies. In addition to improved origin models, the next logical step in definitively understanding the origin, evolution, and composition of Phobos and Deimos is *in situ* analysis of composition or sample return from these satellites.

2.6 Acknowledgements

We thank NASA/JHUAPL for support on this work and the engineers and scientists associated with the CRISM operations center. Further, we thank the team of OMEGA scientists and engineers for the acquisition, processing, and availability of the OMEGA data. Bruce Hapke and Beth Clark provided constructive comments that greatly enhanced the clarity of the published manuscript. We also thank Nancy Chabot for reviewing an early draft of this chapter leading to an improved version. This research utilizes spectra available from the NASA RELAB facility at Brown University and spectra provided by Noah Izenberg, Rachel Klima, and Debra Lorin. This work was supported by CRISM APL/JPL contract 104149 and AAF was funded by an NSF Graduate Student Research Fellowship, Grant #DGE-1143954.

2.7 TABLES

Table 2.1: Summary OMEGA and CRISM Phobos and Deimos disk-resolved observations

All OMEGA and CRISM Phobos and Deimos disk-resolved observations. Observations in italics were not used in this study due to insufficient wavelength coverage, lower quality data, or low spatial resolution. The observations cover a range of phase angles and have varying spatial resolutions. Incidence *i*, emergence *e*, and phase angle α for the OMEGA data were computed using a prototype version of the Navigation and Ancillary Information Facility (NAIF) SPICE Toolkit that includes a Digital Shape Kernel (DSK) system in conjunction with a Phobos shape model. The photometric angles *i*, *e*, and α for the CRISM dataset were calculated using P. Thomas' shape model and the SciBox toolkit [*Thomas*, 1993; *Choo et al.*, 2012; *McGovern et al.*, 2012].

Disk Resolved OMEGA and CRISM Observations of Phobos and Deimos

Moon	Inst.	Obs ID	Acquisition Date	Wavelength Range	Avg. Phase Angle	Spatial Resolution	Hemisphere	HRSC/HiRISE Context Image
Phobos	OMEGA	ORB0413_0	2004-05-18	0.35-5 μm	43°	2200 m/pixel	Sub-Mars	H0413_0000
		ORB0756_0	2004-08-22	0.35-5 μm	63°	200 m/pixel	Sub-Mars	H0756_0000
		ORB2747_0	*2006-06-09*	*0.35-1 μm* (V-channel only obs)	*93°*	*Not used in this study*		*H2747_0000*
		ORB2780_0	*2006-04-20*	*0.35-1 μm* (V-channel only obs)	*47°*			*H2787_0000*
		ORB3769_3	2006-12-14	0.35-5 μm	86°	1170 m/pixel	Both	H3769_0000
		ORB3843_3	2007-01-03	0.35-5 μm	66°	800 m/pixel	Anti-Mars	H3843_0000
		ORB5851_2	2008-07-23	0.35-5 μm	99°	120 m/pixel	Anti-Mars	H5851_0000
		ORB7926_3	2010-03-10	0.35-5 μm	38°	380 m/pixel	Anti-Mars	H7926_0009
		ORB8477_0	*2010-09-10*	*0.35-5 μm*	*70°*	*Not used in this study*		*H8477_0000*
		ORB8974_0	*2011-01-17*	*0.35-1 μm* (V-channel only obs)	*38°*			*H8974_0000*
	CRISM	FRT00002992	2007-10-23	0.4-3.9 μm	41°	350 m/pixel	Sub-Mars	PSP_007769_9015
Deimos	CRISM	FRT00002983	2007-06-07	0.4-3.9 μm	22°	1200 m/pixel		ESP_012065_9000

*Acquired at a separate time than CRISM observation but still used for context imaging

2.8 FIGURES

Figure 2.1: HRSC and OMEGA observations of Phobos with viewing geometries

False color observations of Phobos from HRSC and OMEGA observations ORB0756_0 and ORB7926_3 along with associated incidence *i*, emergence *e*, and phase angle α calculations that were generated using the NAIF SPICE system. The most prominent feature in these observations is the 9 km Stickney crater, labeled in the HRSC image.

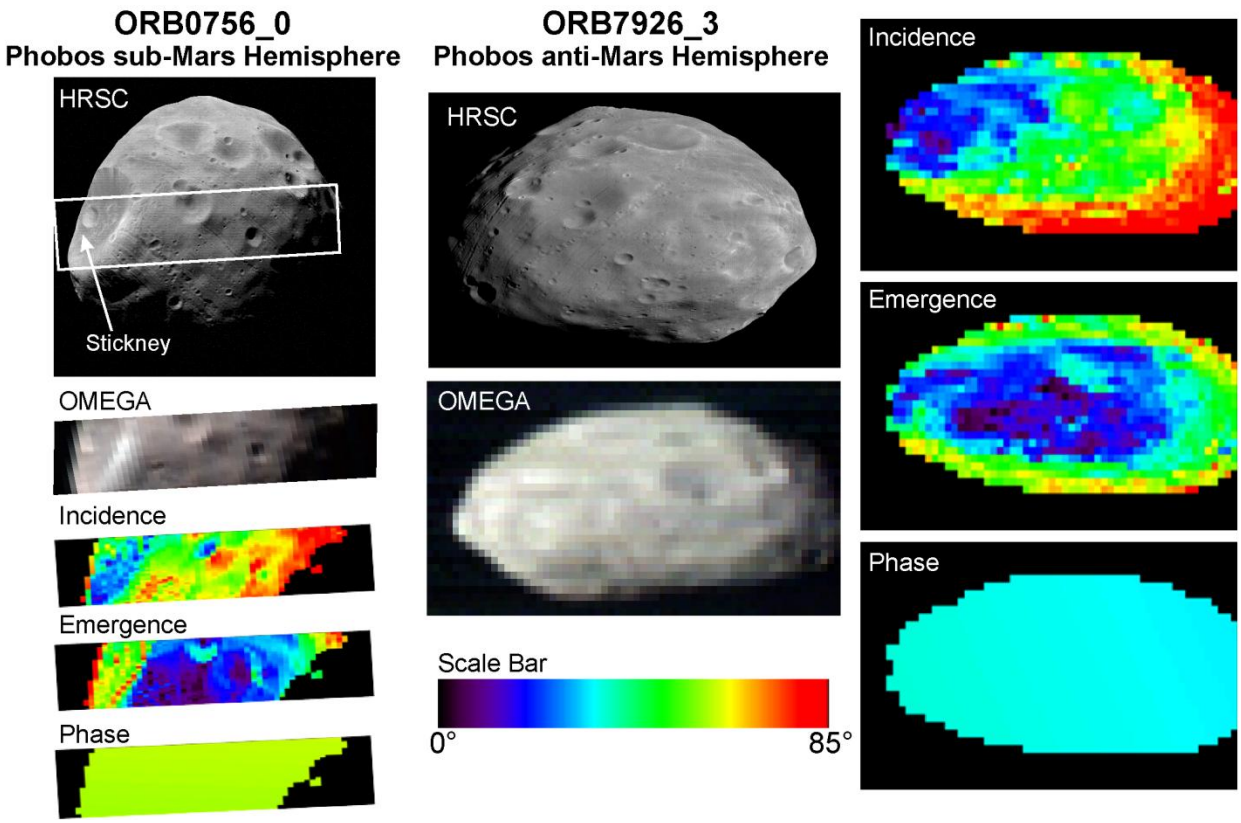

Figure 2.2: HiRISE and CRISM observations of Phobos with viewing geometries

False color observations of Phobos from HiRISE PSP_007769_9015 and CRISM FRT00002992_03_IF162S_TRR7. The incidence *i*, emergence *e*, and phase angles α for the CRISM observation were calculated using the SciBox toolkit.

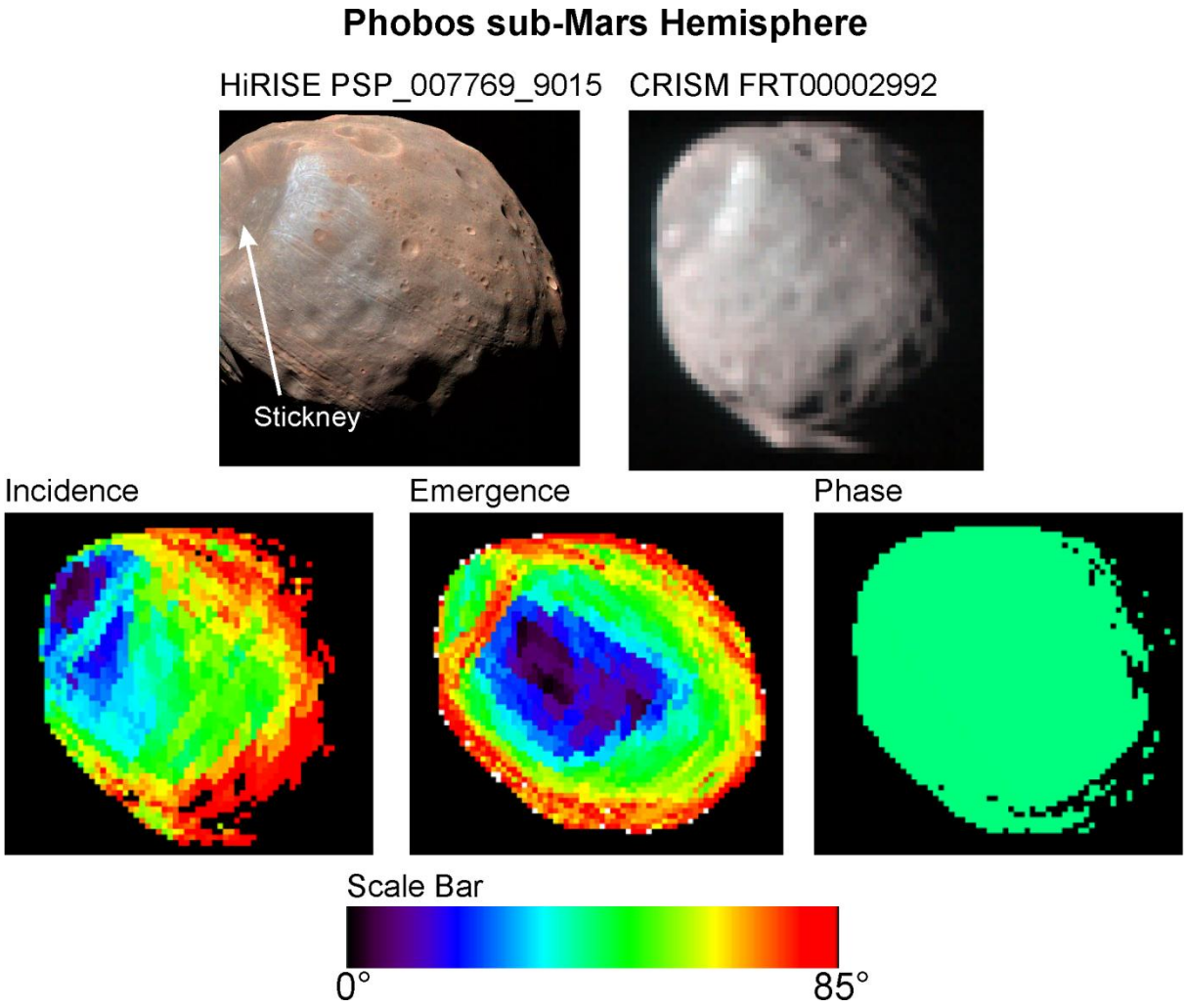

Figure 2.3: Demonstration of importance of reflected solar radiance and themal emission in OMEGA L-detector data

OMEGA radiance data of Phobos from ORB0756_0 (red, green, blue) plotted along the scattered solar radiance expected for a surface with a constant Lambert albedo of 0.05. Also shown are associated graybody curves for a range of expected surface temperatures at the time of the observation. This figure demonstrates the relative importance of both reflected solar radiance and thermal emission in the OMEGA L-detector data. Additionally, this simple model shows Phobos has a changing albedo that likely increases with wavelength beyond 2.7 μm.

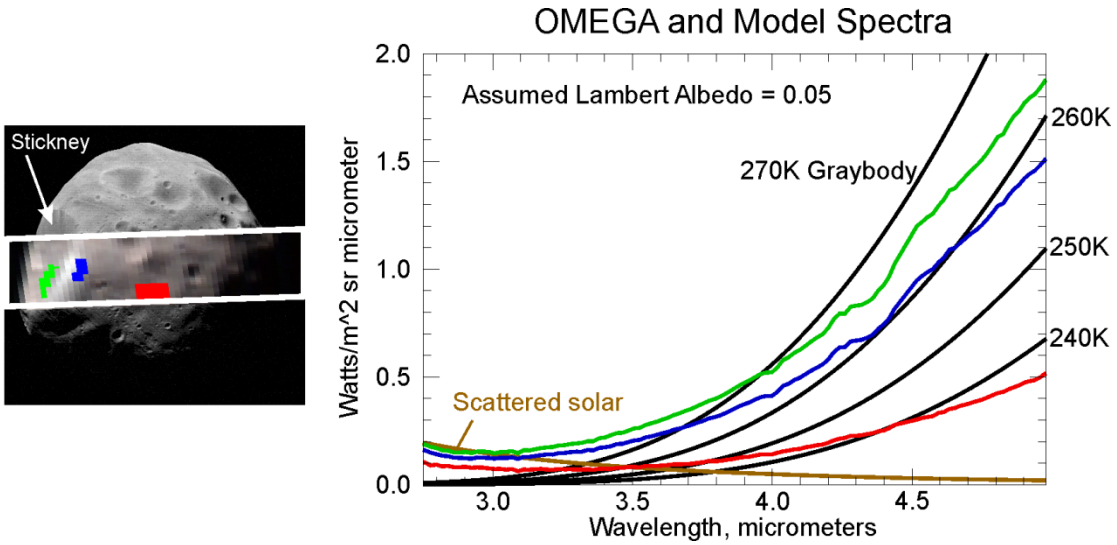

Figure 2.4: Representative Phobos I/F Spectra from CRISM and OMEGA

Representative region of interest (ROI) I/F spectra from blue and red regions of Phobos, as well as Stickney interior from OMEGA ORB0756_0 (top left) and CRISM FRT00002992_03 (top right). Associated ROIs are indicated in the bottom figures. Spectra used in this analysis have been smoothed using a median filter with a width of 10 channels and plotted atop original I/F data (dots). Gaps in the OMEGA data around 1 and 2.7 μm and CRISM data around 0.6, 1, and 2.7 μm are associated with boundaries between detectors and optical filters mounted on the detectors. We restrict our CRISM analyses to wavelengths < 2.6 μm pending resolution of radiometric calibration artifacts at longer wavelengths, and data from this wavelength region is shown for illustrative purposes only. Overall, spectra from the CRISM observation are systematically redder and brighter than OMEGA spectra due to differences in viewing geometry (OMEGA average phase angle = 63°, CRISM average phase angle = 41°).

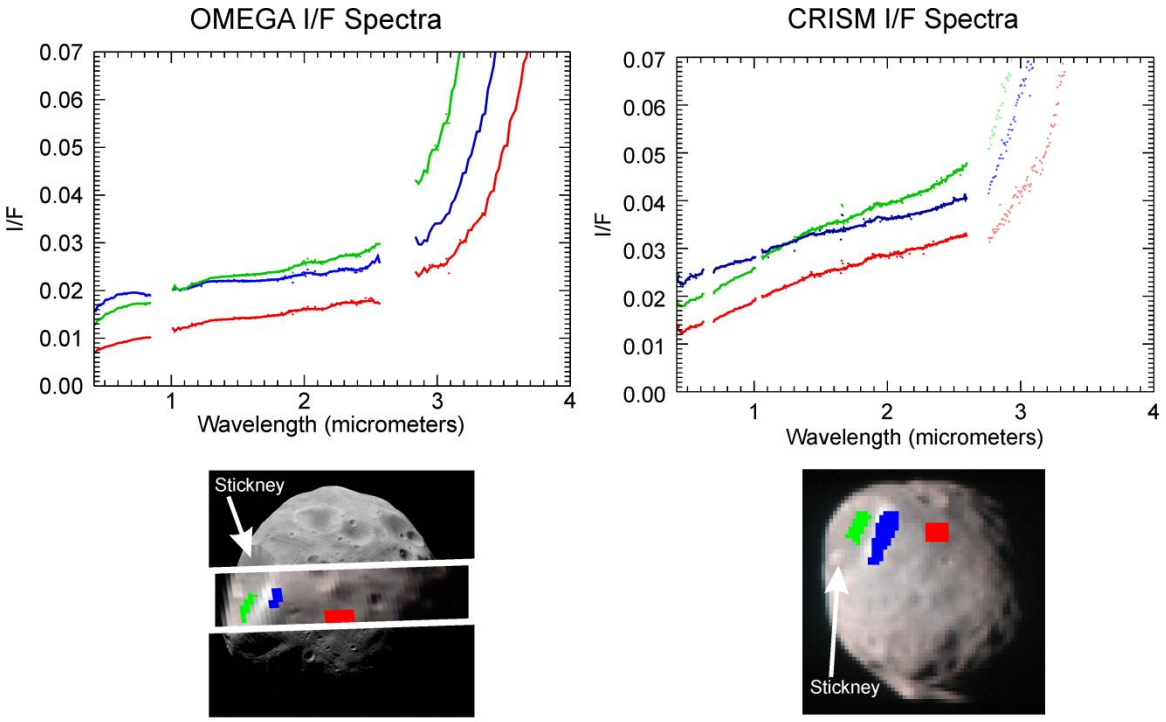

Figure 2.5: HiRISE and CRISM observations for Deimos with viewing geometries

False color observations of Deimos from HiRISE ESP_012065_9000 and CRISM FRT00002983_03_IF162S_TRR7. The HiRISE and CRISM images were taken at different times and cover different locations on Deimos; we show them here to provide higher resolution context of the surface of Deimos. The incidence *i*, emergence *e*, and phase angles α for the CRISM observation were calculated using the SciBox toolkit.

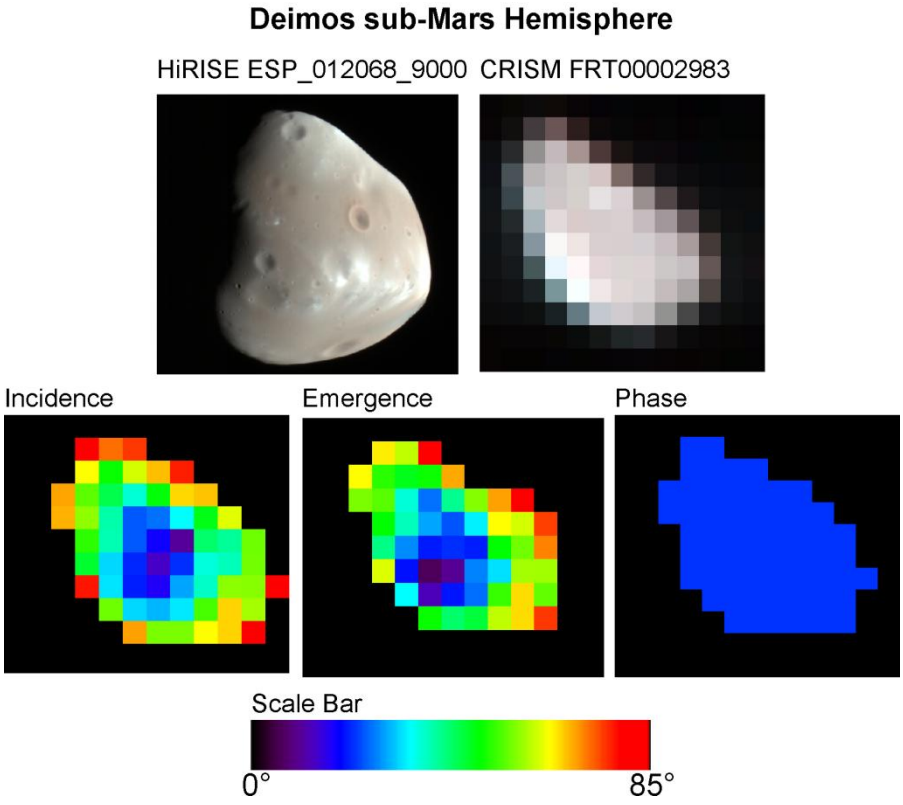

Figure 2.6: Representative Deimos I/F Spectrum from CRISM

Average CRISM Deimos spectrum from FRT00002983_03_IF162_TRR7. Portions of the spectrum used in this analysis have been smoothed using a median filter with a width of 10 channels (black) and plotted atop original I/F data (gray). Gaps in the data around 0.6, 1, and 2.7 μm are associated with boundaries between detectors and optical filters mounted on the detectors. We restrict our CRISM analyses to wavelengths < 2.6 μm pending resolution of radiometric calibration artifacts at longer wavelengths, and data from this wavelength region is shown for illustrative purposes only.

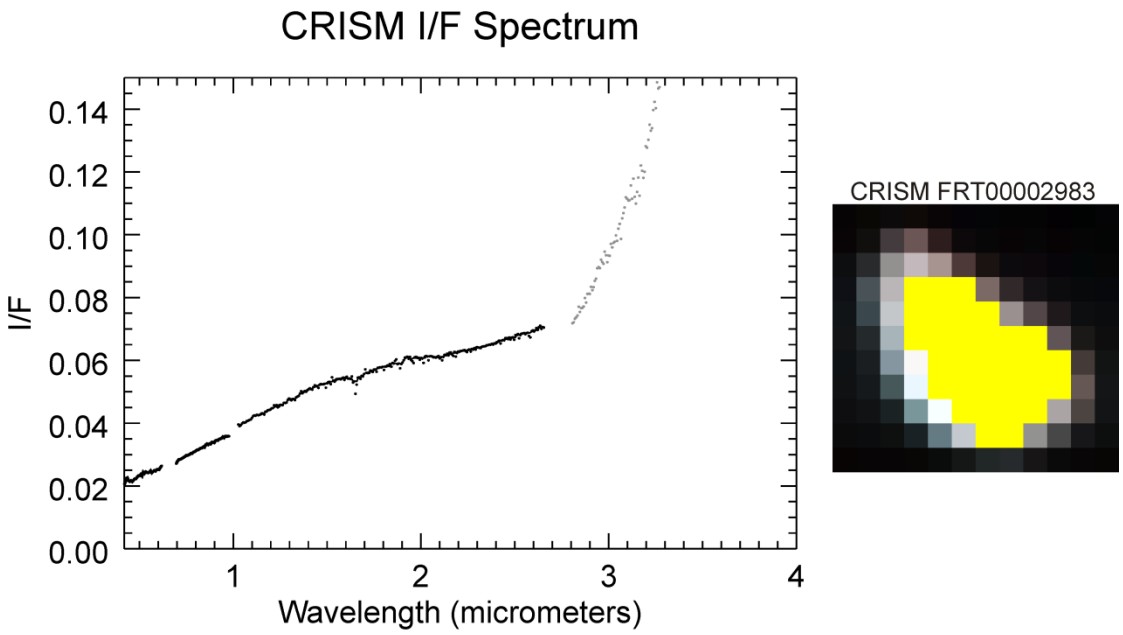

Figure 2.7: Range of incidence and emergence angles in the OMEGA datasets

Range of incidence and emergence angles for points used to find best fit global Hapke parameters. The phase angles were essentially constant across each individual observation and are presented in Table 1.

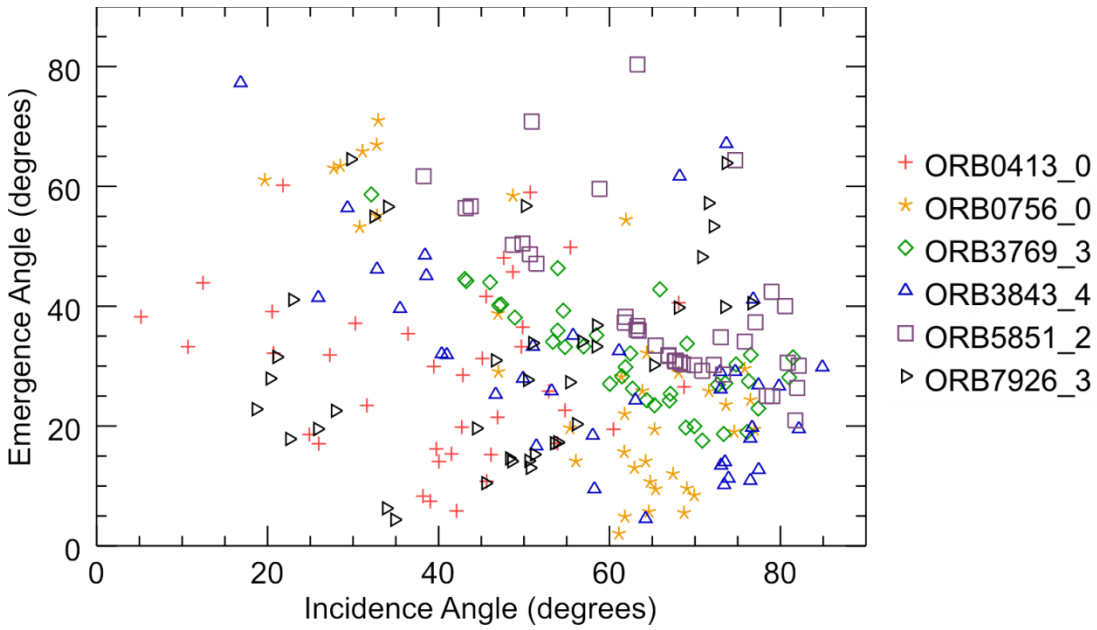

Figure 2.8: Global average best-fit single scattering albedo

Wavelength dependent, global average best-fit single scattering albedo at selected wavelengths between 0.4 and 2.5 μm. The gap in data around 1 μm is due to a detector gap in the OMEGA instrument. All values were derived from OMEGA observations only. Also shown for comparison is global-average best-fit single scattering albedo derived from Viking clear-filter data [*Simonelli et al.*, 1998].

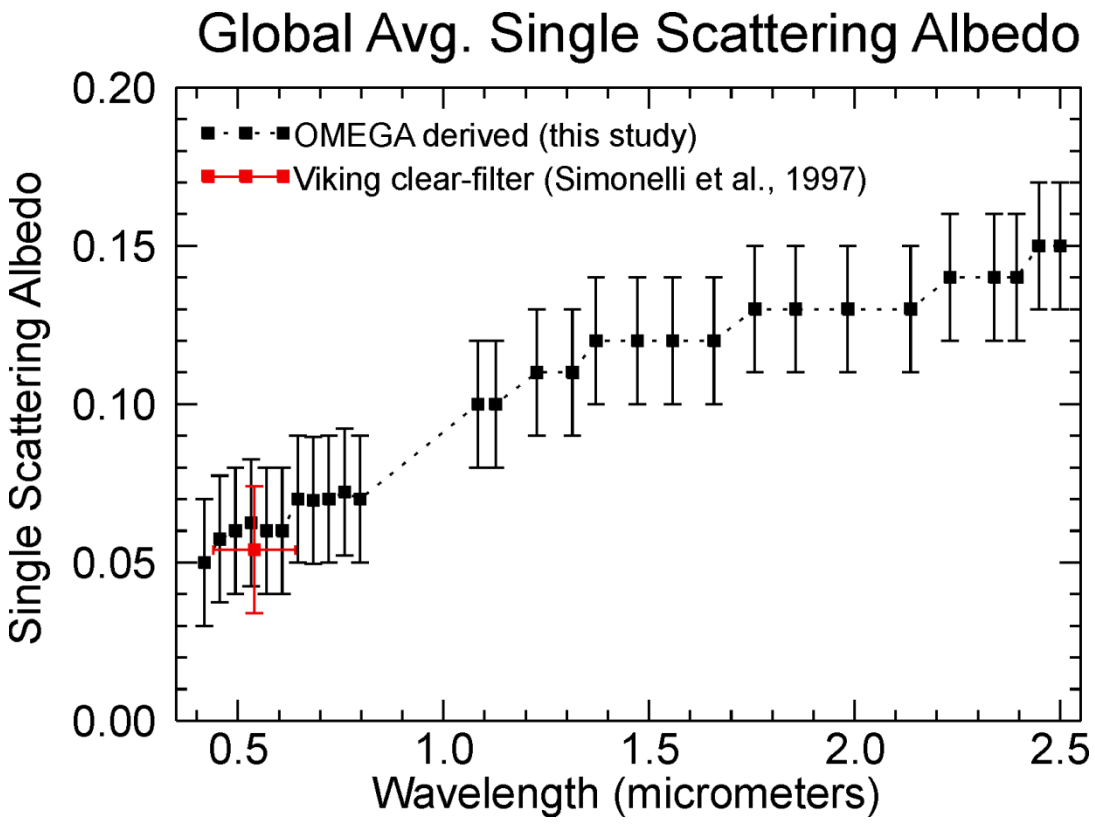

Figure 2.9: I/F and SSA spectra from the same regions on Phobos and Deimos

CRISM and OMEGA raw I/F data from the Phobos red unit and Deimos (top) and their associated single scattering albedos derived using the OMEGA best-fit single particle phase function and roughness parameter (bottom).

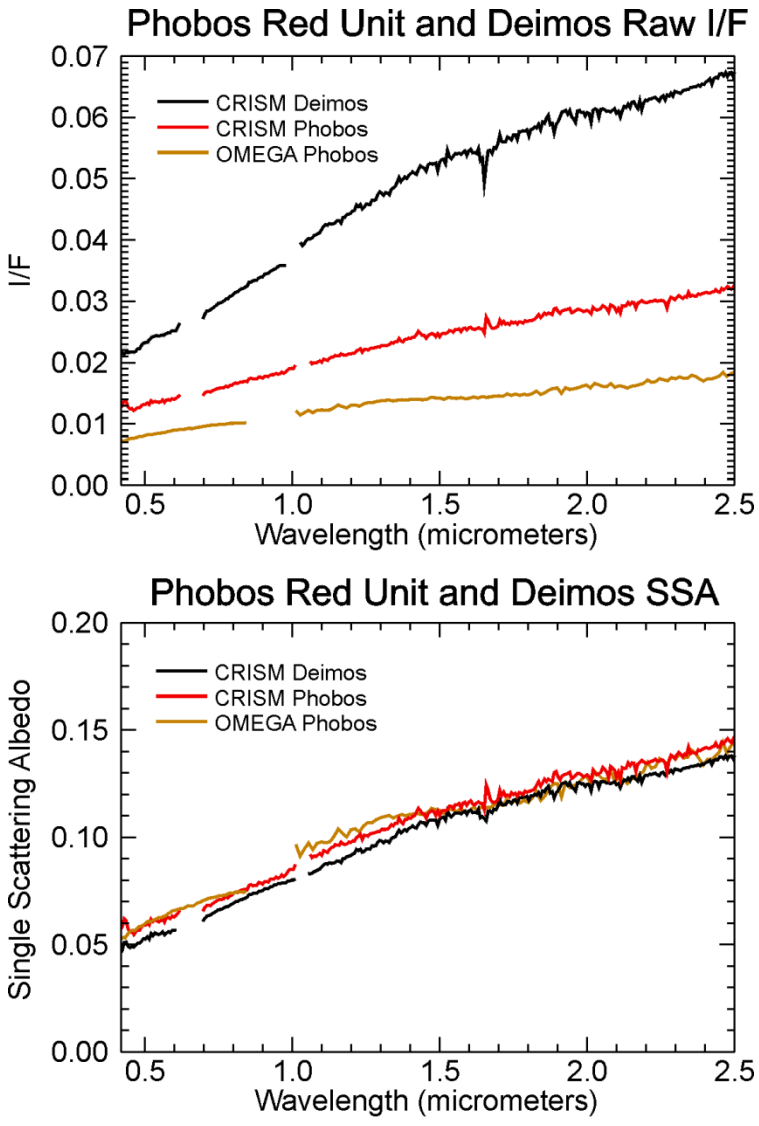

Figure 2.10: Demonstrations of attempts to thermally correct OMEGA data to 5 µm

Demonstration of attempts to thermally correct a single pixel spectrum beyond ~2.5 µm. In this case, we have assumed an asymmetry parameter of -0.28 and solved for single scattering albedo using the full Hapke model, which includes a temperature-dependent term that we have fit using three reasonable temperatures, similar to those predicted by thermal models. Although the spectra have been smoothed using a median filter, they are still noisy, particularly around the thermal crossover region. Our analysis of this spectral region is therefore somewhat notional and we merely conclude the single scattering albedo of Phobos increases with wavelength until at least ~4 µm.

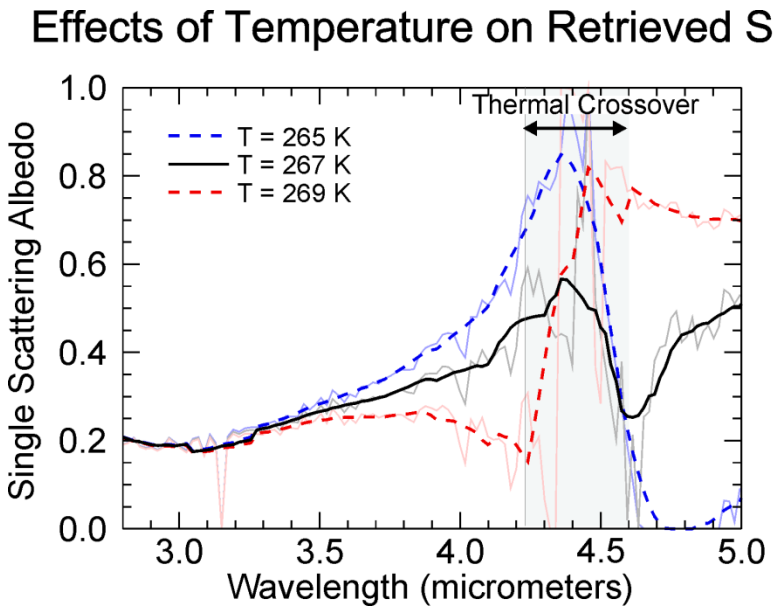

Figure 2.11: Representative Phobos and Deimos SSA spectra from CRISM and OMEGA

Representative ROI single scattering albedo spectra from OMEGA (top left) and CRISM (top right) observations of Phobos and Deimos. ROIs are the same as shown in Figures 2.4 and 2.6. Spectra have been smoothed using a median filter with a width of 10 channels and have been plotted atop original data (dots). Gaps in the OMEGA data around 1 μm and CRISM data around 0.6 and 1 μm are associated with detector and filter boundaries. Despite the variation in viewing geometries of the two observations, there is generally good agreement between the CRISM and OMEGA spectra, consistent with the notion that single scattering albedo is independent of viewing geometry. Minor differences between spectra from the two instruments are likely due to small differences in instrument calibrations.

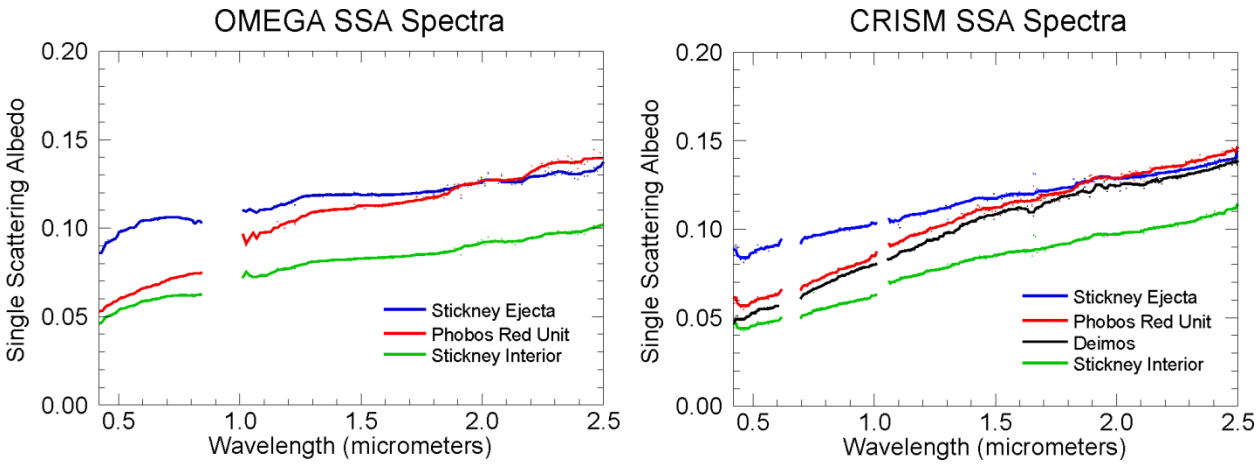

Figure 2.12: Comparison of Phobos and Deimos spectra to laboratory analogs, the Moon, and Mercury

Top: Comparison of CRISM and OMEGA spectra to laboratory analogs available in the RELAB database. The CRISM and OMEGA single scattering albedo data have been reprojected to bidirectional radiance coefficient spectra (eq. 3) acquired at the same viewing geometries as the laboratory spectra ($i = \alpha = 30°$ and $e = 0°$). The Phobos blue unit (top left), red unit (top right), and Deimos (top right) spectra are all good matches to primitive meteorites [*Hiroi et al., 1993; Cloutis et al., 2011*] in terms of slope and absolute brightness. RELAB spectra plotted are cdmb64 (Heated Murchison < 63 μm), s1rs42 (Mighei < 45 μm), bkramt011 (Tagish Lake), c1mb61 (Cold Bokkeveld < 125 μm), cdms01 (Mighei Bulk < 40 μm), and c1lr73, c1lr11, c1lr80 (lunar mare 15071, 12001, 15041). Bottom: Comparison of modeled CRISM Phobos blue and red unit spectra to surface spectra from highly space weathered parent bodies. Here, the CRISM spectra have been modeled as I/F spectra at two viewing geometries. Bottom left shows a comparison between Phobos blue and red units to Lunar Mare spectra collected by M3 and corrected to $i = \alpha = 30°$ and $e = 0°$ [Green et al., 2011]**.** Bottom right shows a comparison between Phobos blue and red unit to average Mercury spectra observed by MACAS at i = e = 45°**,** $\alpha = 90°$ [Izenberg et al., 2012]. In both cases, the Phobos spectra are much darker than the space weathered surface spectra.

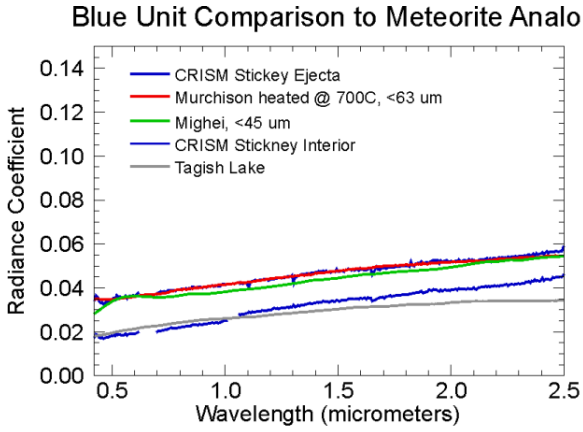
Blue Unit Comparison to Meteorite Analogs
CRISM Stickey Ejecta
Murchison heated @ 700C, <63 um
Mighei, <45 um
CRISM Stickney Interior
Tagish Lake
Radiance Coefficient
Wavelength (micrometers)

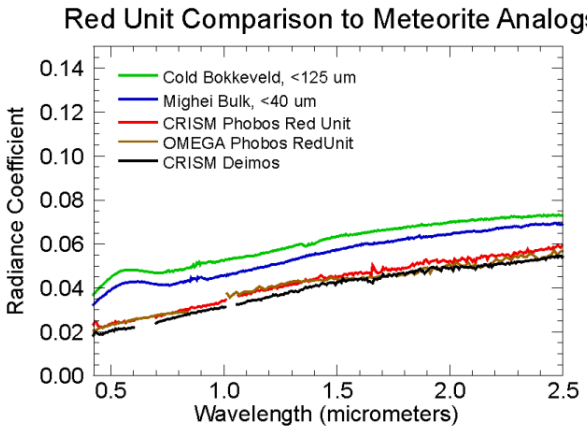
Red Unit Comparison to Meteorite Analogs
Cold Bokkeveld, <125 um
Mighei Bulk, <40 um
CRISM Phobos Red Unit
OMEGA Phobos RedUnit
CRISM Deimos
Radiance Coefficient
Wavelength (micrometers)

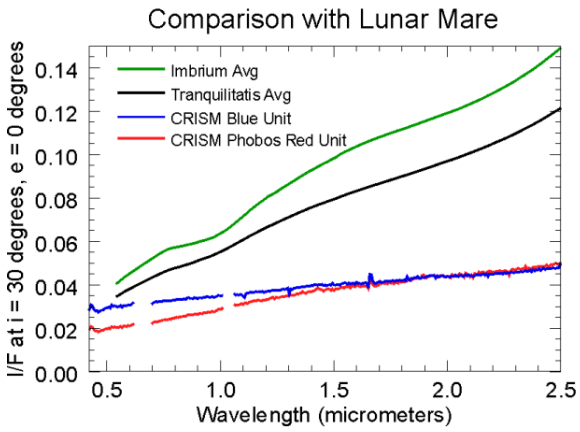
Comparison with Lunar Mare
Imbrium Avg
Tranquilitatis Avg
CRISM Blue Unit
CRISM Phobos Red Unit
I/F at i = 30 degrees, e = 0 degrees
Wavelength (micrometers)

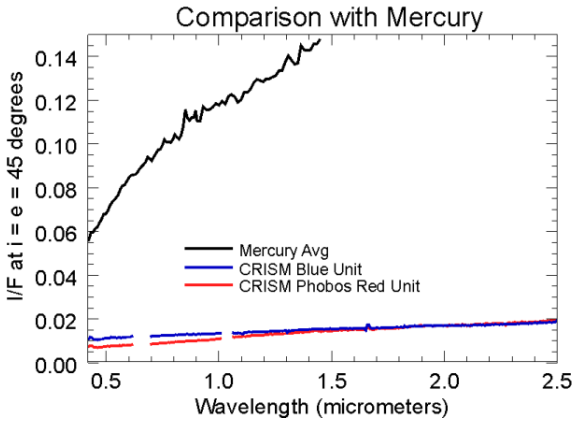
Comparison with Mercury
Mercury Avg
CRISM Blue Unit
CRISM Phobos Red Unit
I/F at i = e = 45 degrees
Wavelength (micrometers)

2.9 REFERENCES CITED

Bibring, J-P. et al. (2004), OMEGA: Observatoire pour la Minéralogie, l'Eau, les Glaces et l'Activité, in *Mars Express: the scientific payload,* edited by A. Wilson, *Eur. Space Agency Spec. Publ.1240,* 37-39.

Bland, P. A., G. Cressey, and O. N. Menzies (2004), Modal mineralogy of carbonaceous chondrites by X-ray diffraction and Mössbauer spectroscopy, *Meteoritics & Planetary Science, 39*, 3–16, doi:10.1111/j.1945-5100.2004.tb00046.x.

Brearley, A. J., and R. H. Jones (1998), Chondritic Meteorites, *Reviews in Mineralogy and Geochemistry, 36,* 3.1–3.398.

Brown, P. G. et al. (2000), The Fall, Recovery, Orbit, and Composition of the Tagish Lake Meteorite: A New Type of Carbonaceous Chondrite, *Science, 290*(5490), 320–325, doi:10.1126/science.290.5490.320.

Burns, J. A. (1978), The dynamical evolution and origin of the Martian moons, *Vistas in Astronomy, 22, Part 2*, 193–210, doi:10.1016/0083-6656(78)90015-6.

Burns, J. A. (1992), Contradictory clues as to the origin of the Martian moons, in *Mars*, edited by H. Kieffer, B. Jakosky, C. Snyder, M. Matthews, Univ. Arizona Press, Tuscon, 1283–1301.

Cantor, B., M. Wolff, P. Thomas, P. James, and G. Jensen (1999), Phobos Disk-Integrated Photometry: 1994–1997 HST Observations, *Icarus*, *142*(2), 414–420, doi:10.1006/icar.1999.6222.

Choo, T. H. et al. (2012), SciBox: An end-to-end automated science planning and commanding system, *ActaAstronautica*, in press.

Clark, B. E., P. Helfenstein, J. F. Bell III, C. Peterson, J. Ververka, N. I. Izenberg, D. Domingue, D. Wellnitz, and L. McFadden (2002a), NEAR Infrared Spectrometer Photometry of Asteroid 433 Eros, *Icarus*, *155*, 189–204, doi:10.1006/icar.2001.6748.

Clark, B. E., B. Hapke, C. Pieters, and D. Britt (2002b), Asteroid Space Weathering and Regolith Evolution, in *Asteroids III*, edited by W. Bottke et al., Univ. of Ariz. Press, Tuscon, 585–599.

Cloutis, E. A., P. Hudon, T. Hiroi, M. J. Gaffey, and P. Mann (2011), Spectral reflectance properties of carbonaceous chondrites: 2. CM chondrites, *Icarus*, *216*(1), 309–346, doi:10.1016/j.icarus.2011.09.009.

Cord, A. M., P. C. Pinet, Y. Daydou, and S. D. Chevrel (2003), Planetary regolith surface analogs, *Icarus*, *165*(2), 414–427, doi:10.1016/S0019-1035(03)00204-5.

Craddock, R. A. (2011), Are Phobos and Deimos the result of a giant impact?, *Icarus*, *211*(2), 1150–1161, doi:10.1016/j.icarus.2010.10.023.

Green, R. O., et al. (2011), The Moon Mineralogy Mapper (M3) imaging spectrometer for lunar science: Instrument description, calibration, on-orbit measurements, science data calibration and on-orbit validation, J. Geophys. Res., 116, E00G19, doi:10.1029/2011JE003797.

Gendrin, A., Y. Langevin, and S. Erard (2005), ISM observation of Phobos reinvestigated: Identification of a mixture of olivine and low-calcium pyroxene, *J. Geophys. Res.*, *110*, doi:200510.1029/2004JE002245.

Goguen, J., J. Veverka, and T. Duxbury (1979), Marsshine on Phobos, *Icarus*, *37*(2), 377–388, doi:10.1016/0019-1035(79)90002-2.

Hapke, B. (1993), *Theory of reflectance and emittance spectroscopy*, Cambridge University Press, Cambridge, UK.

Hapke, B. (2001), Space weathering from Mercury to the asteroid belt, *J. Geophys. Res.*, *106*(E5), 10,039–10,073, doi:200110.1029/2000JE001338.

Hapke, B. (2005), Theory of Reflectance and Emittance Spectroscopy, *Theory of Reflectance and Emittance Spectroscopy*, Cambridge University Press, Cambridge, UK.

Hartmann, W. K. (1990), Additional evidence about an early intense flux of C asteroids and the origin of Phobos, *Icarus*, *87*(1), 236–240, doi:10.1016/0019-1035(90)90033-6.

Helfenstein, P., and J. Veverka (1989), Physical characterization of asteroid surfaces from photometric analysis, in *Asteroids II*, edited by R. Binzel et al., Univ. of Ariz. Press, Tuscon, 557–593.

Hiroi, T., C. M. Pieters, M. E. Zolensky, and M. E. Lipschutz (1993), Evidence of Thermal Metamorphism on the C, G, B, and F Asteroids, *Science*, *261*(5124), 1016–1018, doi:10.1126/science.261.5124.1016.

Hiroi, T., M. E. Zolensky, and C. M. Pieters (2001), The Tagish Lake Meteorite: A Possible Sample from a D-Type Asteroid, *Science*, *293*(5538), 2234–2236, doi:10.1126/science.1063734.

Hunten, D. M. (1979), Capture of Phobos and Deimos by photoatmospheric drag, *Icarus*, *37*(1), 113–123, doi:10.1016/0019-1035(79)90119-2.

Izenberg, N. R., G. M. Holsclaw, D. L. Domingue, W. E. McClintock, R. L. Klima, D. T. Blewett, M. C. Kochte, J. Helbert, M. D'Amore, A. L. Sprague, F. Vilas, and S. C. Solomon (2012) Ultraviolet Through Near-Infrared Reflectance Variation on Mercury and the Search for Mineralogical Telltales, Lunar Planet. Sci. 43, abstract #2365.

Johnson, J. R. et al. (2006), Spectrophotometric properties of materials observed by Pancam on the Mars Exploration Rovers: 1. Spirit, *J. Geophys. Res.*, *111*, E02S14, doi:200610.1029/2005JE002494.

Kuzmin, R. O., and E. V. Zabalueva (2003), The temperature regime of the surface layer of the Phobos regolith in the region of the potential Fobos-Grunt space station landing site, *Solar System Research*, *37*(6), 480–488, doi:10.1023/B:SOLS.0000007946.02888.bd.

Lodders, K., and B. Fegley (1998), *The Planetary Scientist's Companion*, Oxford University Press, Oxford.

Loizeau, D. et al. (2007), Phyllosilicates in the Mawrth Vallis region of Mars, *J. Geophys. Res.*, *112*, E08S08, doi:200710.1029/2006JE002877.

Lucey, P., and S. Noble (2008), Experimental test of a radiative transfer model of the optical effects of space weathering, *Icarus*, *197*(1), 348–353, doi:10.1016/j.icarus.2008.05.008.

Lucey, P. G., and M. A. Riner (2011), The optical effects of small iron particles that darken but do not redden: Evidence of intense space weathering on Mercury, *Icarus*, *212*(2), 451–462, doi:10.1016/j.icarus.2011.01.022.

Markwardt, C. B. (2009), Non-linear Least-squares Fitting in IDL with MPFIT, *Astronomical Society of the Pacific*, (411), 251-254.

McGovern, J. A., S. L. Murchie, K. D. Seelos, H. Nair, and F. P. Seelos (2012), Cost effective operation of the CRISM instrument, *ActaAstronautica*, in press.

Moré, J. J. (1978), The Levenberg-Marquardt algorithm: Implementation and theory, in *Numerical Analysis*, vol. 630, edited by G. A. Watson, 105–116, Springer Berlin Heidelberg.

Murchie, S., and S. Erard (1996), Spectral Properties and Heterogeneity of Phobos from Measurements by Phobos 2, *Icarus*, *123*(1), 63–86, doi:10.1006/icar.1996.0142.

Murchie, S. et al. (2007), Compact Reconnaissance Imaging Spectrometer for Mars (CRISM) on Mars Reconnaissance Orbiter (MRO), *J. Geophys. Res.*, *112*, E05S03, doi:200710.1029/2006JE002682.

Murchie, S., T. Choo, D. Humm, A. Rivkin, J.-P. Bibring, Y. Langevin, B. Gondet, T. Roush, T. Duxbury, and CRISM Team (2008). MRO/CRISM Observations of Phobos and Deimos. Lunar Planet. Sci. 39, abstract #1434.

Murchie, S.L, F.P. Seelos, C.D. Hash, D.C. Humm, E. Malaret, J.A. McGovern, K.D. Seelos, D.L. Buczkowski, M.F. Morgan, O.S. Barnouin-Jha, H. Nair, H.W. Taylor, G.W. Patterson, C.A. Harvel, J.F. Mustard, R.E. Arvidson, P. McGuire, M.D. Smith, M.J. Wolff, T.N. Titus, and the CRISM Science Team, The CRISM investigation and data set from the Mars Reconnaissance Orbiter's Primary Science Phase, J. Geophys. Res., 114, E00D07, doi:10.1029/2009JE003344, 2009.

Mustard, J. F., F. Poulet, A. Gendrin, J.-P. Bibring, Y. Langevin, B. Gondet, N. Mangold, G. Bellucci, and F. Altieri (2005), Olivine and Pyroxene Diversity in the Crust of Mars, *Science*, *307*(5715), 1594 –1597, doi:10.1126/science.1109098.

Noble, S. K., C. M. Pieters, L. A. Taylor, R. V. Morris, C. C. Allen, D. S. McKAY, and L. P. Keller (2001), The optical properties of the finest fraction of lunar soil: Implications for space weathering, *Meteoritics & Planetary Science*, *36*(1), 31–42, doi:10.1111/j.1945-5100.2001.tb01808.x.

Noble, S. K., C. M. Pieters, and L. P. Keller (2007), An experimental approach to understanding the optical effects of space weathering, *Icarus*, *192*(2), 629–642.

Pelkey, S. M. et al. (2007), CRISM multispectral summary products: Parameterizing mineral diversity on Mars from reflectance, *J. Geophys. Res.*, *112*, E08S14, doi:200710.1029/2006JE002831.

Pieters, C. M., L. A. Taylor, S. K. Noble, L. P. Keller, B. Hapke, R. V. Morris, C. C. Allen, D. S. McKay, and S. Wentworth (2000), Space weathering on airless bodies: Resolving a mystery with lunar samples, *Meteoritics & Planetary Science*, *35*(5), 1101–1107, doi:10.1111/j.1945-5100.2000.tb01496.x.

Rivkin, A. S., R. H. Brown, D. E. Trilling, J. F. Bell III, and J. H. Plassmann (2002), Near-Infrared Spectrophotometry of Phobos and Deimos, *Icarus*, *156*(1), 64–75, doi:10.1006/icar.2001.6767.

Safronov, V. S., Pechernikova, G. V., Ruskol, E. L., and Vitjazev, A. V. (1986) Protosatellite swarms. in *Satellites*. J. A. Burns and M. S. Matthews, editors. University of Arizona Press, Tucson, AZ, pp. 89–116.

Sasaki, S. (1990) Origin of Phobos: Aerodynamic drag capture by the primary atmosphere of Mars. Lunar Planet. Sci. 21, abstract #1069.

Simonelli, D., M. Wisz, A. Switala, D. Adinolfi, J. Ververka, P. Thomas, and P. Helfenstein (1998), Photometric Properties of Phobos Surface Materials From Viking Images, *Icarus*, *131*(1), 52–77, doi:10.1006/icar.1997.5800.

Taylor, L. A., C. M. Pieters, L. P. Keller, R. V. Morris, and D. S. McKay (2001), Lunar Mare Soils: Space weathering and the major effects of surface-correlated nanophase Fe, *J. Geophys. Res.*, *106*(E11), 27,985–27,999, doi:200110.1029/2000JE001402.

Thomas, N., R. Stelter, A. Ivanov, N. T. Bridges, K. E. Herkenhoff, and A. S. McEwen (2011), Spectral heterogeneity on Phobos and Deimos: HiRISE observations and comparisons to

Mars Pathfinder results, *Planetary and Space Science*, *59*(13), 1281–1292, doi:10.1016/j.pss.2010.04.018.

Thomas, P. (1993), Gravity, Tides, and Topography on Small Satellites and Asteroids: Application to Surface Features of the Martian Satellites, *Icarus*, *105*(2), 326–344, doi:10.1006/icar.1993.1130.

Thomas, P., D. Adinolfi, P. Helfenstein, D. Simonelli, and J. Vevkera (1996), The Surface of Deimos: Contribution of Materials and Processes to Its Unique Appearance, *Icarus*, *123*(2), 536–556, doi:10.1006/icar.1996.0177.

Chapter 3: Spectral Absorptions on Phobos and Deimos in the Visible/Near Infrared Wavelengths and Their Compositional Constraints

Associated Publication: Fraeman, A., Murchie, S., Arvidson, R., Clark, R., Morris, R., Rivkin, A., Vilas, F. 2014. "Spectral absorptions on Phobos and Deimos in the visible/near infrared wavelengths and their compositional constraints," *Icarus*, 229, 196-205, doi: 10.1016/j.icarus.2013.11.021

ABSTRACT

Absorption features on Phobos and Deimos in the visible / near infrared wavelength region (0.4 - 3.9 μm) are mapped using observations from the Compact Reconnaissance Imaging Spectrometer for Mars (CRISM). Fe^{2+} electronic absorptions diagnostic of olivine and pyroxene are not detected. A broad absorption centered around 0.65 μm within the red spectral units of both moons is detected, and this feature is also evident in telescopic, Pathfinder, and Phobos-2 observations of Phobos. A 2.8 μm metal-OH combination absorption on both moons is also detected in the CRISM data, and this absorption is shallower in the Phobos blue unit than in the Phobos red unit and Deimos. The strength, position, and shape of both of the 0.65 μm and 2.8 μm absorptions are similar to features seen on red-sloped, low-albedo primitive asteroids. Two end-member hypotheses are presented to explain the spectral features on Phobos and Deimos. The first invokes the presence of highly desiccated Fe-phyllosilicate minerals indigenous to the bodies, and the second invokes Rayleigh scattering and absorption of small iron particles formed by exogenic space weathering processing, coupled with implantation of H from solar wind. Both end-member hypotheses may play a role, and in-situ exploration will be needed to ultimately determine the underlying causes for the pair of spectral features observed on Phobos and Deimos.

3.1 INTRODUCTION

The compositions of Mars' small and irregularly shaped moons, Phobos and Deimos, have remained controversial despite multiple Earth- and space-based observations acquired during the last 40 years (Rivkin, 2007 and references therein). Phobos exhibits two spectral units that are both dark, yet distinctly different at visible to near infrared wavelengths (Fig. 3.1, 3.2). The two units are a spectrally red-sloped (increasing reflectance with increasing wavelength) "red unit" that covers most of Phobos and a less red-sloped "blue unit" that is present in the interior and ejecta of the ~9-km diameter impact crater Stickney (Murchie and Erard, 1996; Rivkin et al., 2002). Deimos is similar spectrally to Phobos' red unit (Rivkin et al., 2002; Fraeman et al., 2012) (Fig. 3.2). Studies using visible to near infrared spectroscopy show that the moons' surfaces resemble D- or T-type asteroids or carbonaceous chondrite meteorites (e.g. Murchie and Erard, 1996; Rivkin et al., 2002; Fraeman et al., 2012), although their specific mineralogy is difficult to determine because they lack strong diagnostic absorption features.

The bulk compositions of Phobos and Deimos provide constraints on how the moons formed. Current hypotheses are that Phobos and Deimos formed *in situ* in Mars orbit (Burns, 1992) or by capture of asteroidal bodies originating outside the Mars system (Hunten, 1979; Sasaki, 1990). Possible compositions for the moons have been proposed based on these formation mechanisms (reviewed by Murchie et al., 2014) including (1) primitive phyllosilicate-rich carbonaceous chondrites or anhydrous, olivine- and pyroxene-dominated carbonaceous chondrites, representing capture of a body from outside the Mars system or late stage addition of primitive materials, (2) darkened ordinary chondrites, similar to a predicted bulk Mars-like composition possibly representing co-accretion, and (3) a Mars crust-like composition representing accretion of ejecta after a giant impact early in Mars' history. Surface materials on

Phobos and Deimos have also been proposed as possible *in situ* sources of water or hydrogen for future human mission to Mars (Castillo-Rogez et al., 2012; Muscatello et al., 2012), and remote sensing constraints on their surface compositions aid in assessing this concept's viability.

In this chapter, results are presented that provide new insights into the compositions of Phobos and Deimos. Band-depth mapping using data from the Compact Reconnaissance Imaging Spectrometer for Mars (CRISM) shows no evidence for olivine or pyroxene. However, CRISM data do show a broad absorption feature centered at 0.65 μm for the entire surface of Deimos and for the red unit of Phobos. New telescopic data of Phobos reported here as well as a reexamination of older spacecraft observations of Phobos and Deimos support the CRISM-based detection. CRISM data also show a 2.8 μm metal-OH absorption present on both moons, although the feature is less deep in the Phobos blue unit. Two end-member models are presented for the origin of this pair of features, representing either a phase inherent to the bodies or phases formed through exogenic processes.

3.2 Data Reductions and Visible/Near-Infrared Absorptions in CRISM Observations

In June and October 2007, the CRISM instrument on the Mars Reconnaissance Orbiter (Murchie et al., 2007) acquired three disk-resolved hyperspectral images each of Deimos and Phobos (Fig. 3.1) using the instrument's full spectral range (0.4 μm to 3.9 μm) with a spectral sampling of ~6.55 nm/channel (Murchie et al., 2008; Fraeman et al., 2012). These data provide the highest spatial (~350 m/pixel) and spectral resolution hyperspectral coverage of Phobos to date, as well as the first disk-resolved (~1200 m/pixel) hyperspectral observations of Deimos. Both sets of observations were acquired over the night side of Mars so that scattered light and Mars-shine on the moons' surfaces are not significant (Goguen et al., 1979). Data shortward of

0.45 μm have lower reliability owing to differences in how the spectrometer's diffraction gratings perform on the two moons, which highly underfill the field of view, versus the internal calibration source, which completely fills the field of view. Measurements longwards of ~3.1 μm are known to be confounded by poorly characterized calibration artifacts and are not analyzed here (Murchie et al., 2007).

Fraeman et al. (2012) derived Hapke scattering parameters for Phobos using observations of the moon made by the Observatoire pour la Mineralogie, l'Eau, les Glaces et l'Activité (OMEGA) onboard Mars Express (Bibring et al., 2004). The OMEGA observations cover a similar wavelength range as the CRISM dataset but at lower spectral resolution, and were acquired over multiple phase angles from 38° to 99° (Fraeman et al., 2012). The OMEGA-based scattering parameters are valid for the CRISM Phobos and Deimos observations (Fraeman et al., 2012), and are used in this chapter to derive single scattering albedo spectra for Phobos and Deimos at wavelengths less than 2.5 μm (Fig. 3.2). Single scattering albedo values are by definition independent of lighting and viewing conditions (Fig. 3.2b).

At wavelengths longer than ~2.5 μm, the moons' radiance factor measured by CRISM (also referred to as I/F and defined as radiance/(solar irradiance/$\boldsymbol{\pi}$)) contains a component from emitted thermal radiation as temperatures on the surface of Phobos and Deimos can reach up to 300-350K (Kuzmin and Zabalueva, 2003; Lynch et al., 2007). In this wavelength region, we therefore must solve for single scattering albedo by jointly modeling both the reflected solar and the thermal emission contributions. The Hapke equation describing contributions from bidirectional reflectance and directional emissivity is expressed as a function of incidence angle i, emission angle e, phase angle α, and kinetic temperature T for a given wavelength is (eq 3.1) (Hapke, 1993):

$$r(i,e,\alpha,T) = \frac{w}{4}\frac{\mu_0}{\mu_0+\mu}\left[\left(1+B(\alpha)\right)p(\alpha,g_1) + H(w,\mu_0)H(w,\mu) - 1\right]S(i,e,\alpha,\theta) + \sqrt{1-w}$$
$$\cdot H(w,\mu)\cdot\frac{\beta_0(T)}{J/\pi}$$

(eq 3.1)

where *w* is the single scattering albedo we wish to solve for, *r* is the radiance factor measured by CRISM, μ and μ_0 are the cosines of the emergence and incidence angles, respectively, $B(\alpha)$ models the opposition-effect, $p(g_1)$ is the single particle phase function, *H* is an approximation for the isotropic multiple scattering function, and *S* is the shadowing function defined by a macroscopic roughness parameter, θ (Hapke, 1993). The parameter β_0 is the Planck irradiance at a given temperature *T*, and *J* is the solar irradiance at the solar distance at the time of observation (Hapke, 1993).

The values of the Hapke parameters for Phobos and Deimos and illumination angles for the CRISM observations are derived in Fraeman et al. (2012), and we use the method of Clark et al., (2011) to derive surface temperatures from the CRISM spectra. This algorithm employs an iterative approach to estimating the thermal contribution and associated temperature for a spectrum using the assumption that the continuum of the reflected solar component of the spectrum is approximately linear between 2.6 and 3.1 μm. Further details, including model validation, can be found in Clark et al., (2011).

3.3 Spectral Analysis

3.3.1 Standard band depth mapping

Mineral parameter maps were generated using single scattering albedo spectra from Phobos and Deimos. Parameter maps designed to highlight broad features caused by Fe^{2+} electronic absorptions in olivine near 1 μm and low- and high-calcium pyroxenes at ~1 μm and

~2 μm (Pelkey et al., 2007) show no discernible absorptions that are not attributable to edge-effect artifacts (Fig. 3.3). Parameters designed to highlight spectra having 1.9 μm absorptions caused by combination overtones of the H_2O bend and OH stretches likewise show no discernible absorptions (Pelkey et al., 2007) (Fig. 3.3).

3.3.2 Spectral feature at 0.65 μm observed in multiple datasets

Preliminary investigation of CRISM spectra revealed a broad, shallow absorption feature on Phobos' red unit and on Deimos (Murchie et al., 2008) (Fig. 3.3, 3.4). Murchie et al., (2008) found the feature was centered close to 0.65 μm, although CRISM data around 0.65 μm are compromised by a boundary between detector-mounted filters, so the feature's actual center can only be approximated by extrapolating data from the absorption's wings near 0.60 and 0.70 μm. Here, the absorption is mapped in the single scattering albedo spectra using a band depth parameter centered where valid data exist around 0.60 μm ($BD_{0.60}$). Assuming a linear continuum between 0.50 and 0.85 μm, the band depth is calculated using the following formulas (eq 2.3, 3.3):

$$BD_{0.60} = 1 - R'_{avg(0.59:0.62)} \tag{3.2}$$

$$R'_{avg(0.59:0.62)} = R_{avg(0.59:0.62)} \Big/ \frac{R_{avg(0.84:0.86)} - R_{avg(0.49:0.51)}}{\lambda_{avg(0.84:0.86)} - \lambda_{avg(0.49:0.51)}} \times \left(\lambda_{avg(0.59:0.62)} - \lambda_{avg(0.49:0.51)}\right) + R_{avg(0.49:0.51)} \tag{3.3}$$

where $R'_{avg(0.59:0.62)}$ is the continuum removed single scattering albedo averaged between 0.59 and 0.62 um, $R_{avg(x:y)}$ is the average single scattering albedo from *x* μm to *y* μm, and $\lambda_{avg(x:y)}$ are the wavelengths associated with reflectances between *x* μm and *y* μm (after Clark and Roush, 1984). Band depths range between ~0.5% and 5% (Fig. 3.3).

The presence and strength of the 0.65 μm absorption is spatially correlated with the slope of the visible to near-infrared spectral continuum, expressed as a visible to near-infrared ratio (eq 3.4):

$$\frac{VIS}{NIR} = \frac{R_{avg(0.40:0.50)}}{R_{avg(0.75:0.85)}} \tag{3.4}$$

In general, spectra with a lower visible to near-infrared ratio (Phobos red spectral unit and Deimos) have 0.65-μm absorption depths ranging between 1% and 4%, and spectra with higher visible to near-infrared ratio (Phobos spectral blue unit) have ~0% 0.65-μm absorption depths (Fig. 3.3, 3.4). On Deimos, the band depth is independent of surface location and equivalent to the strongest band depths on Phobos (~3-5%) (Fig. 3.3, 3.4).

The 0.65 μm feature on Phobos is also evident in ground based telescopic spectra obtained on 4-5 September 2003 UT using the Mayall 4-m telescope on Kitt Peak with the Ritchey-Chretien Spectrograph (RCSP) as part of a campaign of near-Earth object (NEO) spectroscopy. These spectra used a solar analog calibration star from the Landolt (1992) catalog (L 93-101) as a the calibration standard. Details of data collection, reduction, and the overall NEO campaign are reported by Binzel et al. (2001) and Binzel et al. [2004]. The Phobos observations focused on the moon's leading hemisphere, which contains the crater Stickney, centered near 60° W longitude, and its exposed blue unit, located on the eastern rim of the crater. Forty-seven images on 4 September obtained between 7:30-8:24 UT were combined into 10 final spectra with central longitudes varying from 52-92° W, and 28 images obtained on 5 September between 6:48-7:08 UT were combined into 6 final spectra with central longitudes from 68-82°W. On both dates the sub-Earth latitude was 36° and the sub-solar latitude 44°.

Disk-integrated spectra centered over predominantly red regions from the 4 Sept 2003 observations reveal a 0.65-μm absorption having a shape and depth similar to the feature observed in the CRISM single scattering albedo spectra (Fig. 3.4). The depth of this band increases as the central longitude of the observation increases from 52° W to 92° W, consistent with disk-integrated reflectance becoming more dominated by Phobos' red unit that exhibits this feature as the central longitude moves off Stickney and the blue unit (Fig. 3.4). Spectra from overlapping locations obtained on 5 Sept 2003 have a systematically lesser band depths than those from 4 Sept 2003, although this observing night was hampered by the presence of clouds, which may have resulted in lower quality data.

Although a feature at 0.65 μm in the Phobos red unit and Deimos has not been reported in spectral data of Phobos and Deimos collected previously by instruments other than CRISM, a reexamination of these datasets shows they are consistent with the CRISM-based results. Visible to near-infrared color-ratio spectra for Phobos obtained by the Imaging Spectrometer for Mars (ISM) instrument onboard the Phobos-2 spacecraft (Murchie and Erard, 1996) also show that a broad 0.65 μm feature is present in the Phobos red unit and absent in the Phobos blue unit. Compared to the bluer unit, Phobos' redder unit exhibits a downward inflection at wavelengths shorter than 0.9-1.0 μm (Murchie and Erard, 1996), similar to that observed in 3.4. The inflection is stronger in materials with lower visible to near-infrared color ratios. Calibration uncertainties and ISM's limitations to wavelengths >0.77 μm prevented definitive recognition of the inflection as being the long-wavelength shoulder of an absorption at 0.65 μm and instead it was mistakenly interpreted from ratio spectra as resulting from a weak 1-μm absorption in the bluer unit.

The 0.65 μm absorption is also recognizable in reexamined disk-integrated spectra of the sub-Mars hemisphere of Phobos obtained from the Martian surface by the Imager for Mars

Pathfinder (IMP) (Murchie et al., 1999). Those data consist of 12-band spectra collected by averaging over the ~3-pixel disk of Phobos, which from the perspective of Mars is dominated by the red unit. Although these measurements were lower in spatial resolution than ISM measurements, they include wavelengths 0.44-1.0 μm covering the full absorption. The absorption's shape, depth, and center near 0.65 μm are consistent with results from CRISM. The multiband photometry approach used to retrieve those spectra yielded higher band-to-band uncertainties than in CRISM spectra, rendering any absorption in the spectrum of the <1-pixel disk of Deimos below the level of noise.

Finally, OMEGA observations of Phobos show spatial variations in VIS/NIR ratio consistent with those in CRISM data, and some observations show a 0.65 μm absorption in the red unit. However, known calibration artifacts (e.g., Fraeman et al., 2012) affecting OMEGA's visible detector (0.35-1.0 μm) preclude definitive detection of the broad and weak 0.65 μm feature in all OMEGA observations of the Phobos red unit, and we withhold detailed analyses of the OMEGA data set pending further resolution of calibration artifacts.

3.3.3 Spectral feature at 2.8 μm

The CRISM single scattering albedo modeled without the thermally emitted component (described in section 3.2) show a feature at 2.8 μm present in spectra for both Phobos and Deimos (Fig. 3.3, 3.5). The spatial distribution of this feature is mapped using equations (3.2) and (3.3) modified for a band center at 2.8 μm and a calculated linear continuum from 2.1 to 2.5 μm, which provides a good approximation for the linear continuum over this feature. Note that CRISM data in the wavelength range 2.70-2.76 μm are compromised by a boundary between filters mounted to the IR detector that blocks higher orders from the diffraction grating; these wavelengths are not routinely downlinked by the instrument.

The depth of the 2.8 μm feature varies from ~1 – 10% across all of Phobos and Deimos, and the band is deepest in the very edges of the image, which may be an artifact caused by extreme viewing geometries (Fig. 3.3). A similar 2.8 μm feature on Earth's moon has been shown to increase in depth at high incidence angles (McCord et al., 2011). Overall, the 2.8 μm band depth map is noisier than the 0.60 μm band depth map and VNIR ratio map (Fig. 3.3), consistent with CRISM data being noisier in this wavelength range. There is not a strong pixel-to-pixel correlation between the depths of the 0.65 μm and 2.8 μm bands or between the VNIR ratio and the depth of the 2.8 μm band. However, the increased noise in the CRISM data at longer wavelengths resulting in the noisy 2.8 μm band depth map could mask potential one-to-one correlations. We therefore compared average band depths from a sample of the reddest Phobos pixels (defined as VNIR ratio < 0.79 and not located at extreme geometries near the moon's limb or terminator), and a sample of the bluest Phobos pixels (defined as VNIR ratio > 0.84, also not located at extreme geometries). The reddest regions of Phobos had an average $BD_{0.60}$ value of 2% ± 1% whereas the bluest regions had an average $BD_{0.60}$ value of -1% ± 1%. The corresponding $BD_{2.8}$ values for the red and blue regions were 7% ± 3% and 3% ± 3% respectively. Two-tailed t-tests comparing the mean $BD_{0.60}$ and $BD_{2.8}$ of samples of pixels from the red and blue units resulted in p-values < 0.001, indicating the differences between these sample means is statistically significant. We conclude pixels in the Phobos red unit are on average associated with deeper 0.65 μm and 2.8 μm bands, whereas pixels in the Phobos blue unit have no 0.65 μm band and a weaker 2.8 μm band. Pixels on Deimos have 2.8-um band depths comparable to the deepest Phobos red unit bands.

The 2.8 μm feature is apparent and has approximately the same spatial distributions in two additional CRISM observations of Phobos (FRT00002992_01 and FRT00002992_05) and

Deimos (FRT00002983_01 and FRT00002983_05) taken in the same sequences immediately before and after the observations shown in Fig. 3.3 (Phobos: FRT00002992_03, Deimos: FRT00002983_3). The lighting and viewing geometry and spatial coverage of the moons is nearly identical within each set of observations, but the positions of the moons varies between observations, providing confidence that the feature is not the result of a column-based artifact in the CRISM data. Although a few CRISM spectral channels near 2.7 μm and data longwards of ~3.1 μm are compromised by instrument artifacts, there are no known plausible instrument artifacts that would produce an apparent asymmetric band at 2.8 μm (D. Humm, personal communication).

As of yet, there are no telescopic- or space-based data sets with sufficient spectral range and signal-to-noise levels to independently validate this feature's presence. OMEGA observations of Phobos do cover the necessary wavelength range, but a detector boundary with an unknown offset near 2.7 μm makes it impractical to detect a weak absorption here.

3.4 Comparison to Asteroid Spectra

Features similar to both the 0.65 μm and 2.8 μm absorptions are observed on dark asteroids interpreted to have primitive compositions (C-, G-, P-, and D-class asteroids). A search through the Vilas asteroid spectral catalog (Vilas et al., 1998) revealed several asteroids with 0.65 μm absorptions that are similar in shape and wavelength to the corresponding features observed on Phobos and Deimos (Fig. 3.6). Asteroids that exhibit these features sometimes have an additional absorption near 0.43 μm or 0.9 μm, but all of them are dark and red sloped. Absorptions near 0.7 μm on low albedo asteroids have been ascribed to Fe-bearing phyllosilicates, and almost always are accompanied by additional absorptions associated with hydration or hydroxylation near 3 μm (Vilas and Gaffey, 1989; Vilas et al., 1993; Vilas, 1994;

Rivkin et al., 2002). Low albedo asteroids having absorptions closer to 0.60 μm - 0.65 μm are interpreted as containing iron oxides when the absorption is paired with a second feature 0.80 - 0.90 μm (Vilas et al., 1994). Mineralogical interpretations for the asteroids most similar to Phobos and Deimos that have absorptions near 0.65 μm but not 0.8 – 0.9 μm remain uncertain (Jarvis et al., 1993; Vilas et al., 1994).

Many low albedo asteroids also display an absorption centered near 2.8 μm, and these features can be qualitatively grouped into Ceres-type, Pallas-type, or Themis-type spectral classes based on band-shape and position (Rivkin et al., 2011). Ceres-type absorptions have a symmetric absorption with minima near 3 μm and 3.3 μm (Milliken and Rivkin, 2009) while Themis-type absorptions are slightly broader, centered near 3.1 μm and 3.4 μm (Rivkin and Emery, 2010). The feature observed on Phobos and Deimos most closely resembles the third class, Pallas-type, which have a single sharp asymmetric absorption near 2.8 μm and are similar to absorptions seen in CM chondrites (Rivkin et al., 2011; Takir et al., 2013). Fig. 3.7 shows a comparison between Phobos and Deimos and other asteroids that show a Pallas-type band when thermal emission is accounted for using the methods described in Rivkin et al., (2011). While the shape and position of the Phobos and Deimos feature in particular is similar to absorptions seen on 96 Aegle, 13 Egeria, and 51 Nemausa, the Phobos and Deimos feature is much weaker than these asteroids, and has a strength more comparable to the band in 566 Stereoskopia (Fig. 3.7). The weakness of the Phobos and Deimos 2.8 μm band in combination with terrestrial atmospheric absorptions near in this wavelength range may explain why this feature has not yet been observed in terrestrial-based observations of the moons (Rivkin et al., 2002).

3.5 COMPARISON TO LAB SPECTRA

3.5.1 Spectral feature at 0.65 μm

Multiple absorption processes can result in a spectral feature near 0.65 μm, including Fe^{2+} and Fe^{3+} electronic transition, Fe^{2+}-Fe^{3+} charge transfer , and metallic iron absorptions combined with Rayleigh scattering by nanophase particles (Morris et al., 1985; Clark et al., 2012). Assignment of the 0.65 μm absorption to both a unique material and formation pathway is therefore difficult because of the non-uniqueness of the feature (King and Clark, 1998). To interpret the feature on Phobos and Deimos, we explored spectra from a variety of phases and materials that can be dark, red-sloped, and have absorptions near 0.65 μm including clay minerals, graphite, ilmenite reduced to Fe metal and Ti_4O_7, nanophase metallic Fe, and CI/CM carbonaceous chondrites and we next discuss in detail two cases that best fit the data.

Fe-bearing phyllosilicates have an absorption centered between 0.65 μm and 0.7 μm. The most common phyllosilicate in CM chondrites (Phobos and Deimos' closest spectral analog based on spectral slope and absolute reflectance (Fraeman, et al., 2012)) is cronstedtite (Cloutis et al., 2011). Cronstedite is dark, red sloped with an absorption centered near 0.7 μm that results from an Fe^{2+} - Fe^{3+} charge transfer transition (Clark et al., 2003; Clark et al., 2007; Calvin and King, 1997) (Fig. 3.8). Linear-continuum removal, however, shows this feature is narrower and centered at a longer wavelength than the 0.65 μm feature on Phobos and Deimos (Fig. 3.8). Phobos and Deimos also lack the broad ~1.2 μm iron absorption seen in cronstedite.

Nontronite, another Fe-bearing phyllosilicate, has an Fe^{3+} electronic transition at 0.65 μm that is closer in position to the feature observed on Phobos and Deimos (Fig. 3.8), but this mineral has additional absorptions around 1.4 μm, 1.9 μm, and 2.3 μm related to H_2O and OH, as well as additional Fe^{3+} electronic features near 0.43 and 0.9 μm, none of which are observed in

the spectrum of Phobos or Deimos. Absorptions could be masked by opaque phases, although it would remain difficult to explain why the large Fe-related feature near 1 μm would be obscured while the 0.65 μm feature reamains detectable. However, any phyllosilicate present on the surface is subjected to desiccating conditions because the moons regularly experience surface temperatures up to ~340 K and are exposed to the vacuum of space (Kuzmin and Zabalueva, 2003; Lynch et al., 2007).

Under desiccating conditions, the spectral properties of desiccated nontronite more closely resemble the Phobos and Deimos spectra. A sample of nontronite desiccated by heating in a dry N_2 atmosphere (i.e., desiccating conditions) at 105° C (378 K) for 451 hours lost the bands at 1.4 μm and 1.9 μm because of the complete removal of its interlayer H_2O. The spectrum also exhibited a shallow feature centered near 0.65 μm instead of separate absorptions centered near 0.6- and 0.9-μm (Morris et al., 2010) (Fig. 3.8).

A mixture of iron particles ranging in size from a few nanometers to a few micrometers provides an alternative spectral match for the 0.65 μm feature on Phobos and Deimos. The optical constants of iron show a strong red slope with a relative minimum near 0.65 μm, and coarse-grained iron particles (few micrometers in diameter) show this spectral structure when observed in an environment that prevents oxidation (Ordal et al., 1985; Cahill et al., 2012; Clark et al., 2012). Iron particles also have the optical property that as particles become smaller, their reflectance is determined by the competing effects of Rayleigh absorption and Rayleigh scattering (Noble et al., 2007; Clark et al., 2012), and a mixture of micrometer and sub-micrometer iron particles can result in enhancement of the apparent strength of the 0.65 μm feature through Rayleigh absorption and Rayleigh scattering.

We were able to model the 0.65 μm absorption feature in the spectra of the red unit on Phobos and Deimos here by direct calculation assuming a mixture of different-sized iron particles embedded in a neutral silicate matrix (Fig. 3.8) and a modified Hapke model (Clark et al., 2012). A best fit model for Phobos uses optical constants of iron (Ordal et al., 1985) and assumes metallic iron particles that are suspended in a relatively transparent matrix having a wavelength independent absorption coefficient and index of refraction similar to values of generic gray basalt (values of 200 and 1.6 respectively). The inclusion of iron in the model causes a red slope, and its combination with generic particles that have wavelength independent absorptions generates concave upward curvature centered near 0.65 μm, as well as convex upward curvature from 1 to 2.5 μm. The strength, width, and position of the 0.65 μm feature varies with iron grain size and abundances, which can be adjusted to match the absorption seen on Phobos and Deimos (Fig. 3.8). The model shown is comprised of a mixture of Fe particles having diameters of 2.6 μm (1.1%) and 3.5 μm (2.1%), nanophase (~nm) iron mixed with spectrally neutral materials having diameters of 1.1 μm (0.8%), 2.5 μm (0.4%), 0.011 μm (0.02%), and uncoated spectrally neutral material with a diameter of 23.0 μm (95.5%).

3.5.2 Spectral feature at 2.8 μm

The position and asymmetric shape of the 2.8 μm feature is uniquely diagnostic of a fundamental vibration caused by a M-O-H (hydroxyl) stretch (Clark et al., 1990). The specific position of this absorption can vary depending on the cation attached to the hydroxyl, although the lack of reliable CRISM data around 2.7 μm makes it difficult to assign a band center with enough precision to provide a constraint for phase identification. Because this feature is generally stronger in pixels with stronger 0.65 μm bands and the 0.65 μm band is consistent with desiccated clays, the 2.8 μm band could result from an M-OH in a desiccated clay.

Alternatively, this feature may be caused by solar-wind induced hydroxylation because of the exposure of Phobos' and Deimos' surfaces to the space environment. Both hypotheses are described in more detail below.

3.6 Discussion and Compositional Interpretations

The absence of detectable Fe^{2+} absorptions on Phobos and Deimos resulting from pyroxene and olivine does not support the moons' compositions being similar to Martian crustal material because, even in space-weathered forms, absorption from these minerals are likely retained at a strength detectable by CRISM. This conclusion follows Fraeman et al.'s (2012) finding that even the lowest-albedo space-weathered basaltic materials on the Earth's moon retain subtle mafic absorptions. Similarly, the lack of these absorptions fails to support a composition of higher-grade carbonaceous chondrites or darkened ordinary chondrites that retain olivine and pyroxene absorptions. The two absorptions that are detected on Phobos and Deimos are similar to absorptions seen in other primitive bodies, supporting previous claims that the moons have a primitive, carbonaceous chondrite-like composition.

We present two end-member hypotheses for the specific phases causing the 0.65 and 2.8 μm spectral features on Phobos and Deimos. In the first hypothesis, both features are caused by the presence of a highly desiccated Fe phyllosilicate(s) indigenous to the Phobos and Deimos. The second hypothesis invokes exogenic processes associated with small iron particles generated during space weathering coupled with OH generated by implantation of H from solar wind. These hypotheses are not mutually exclusive and both could be active.

3.6.1 Hypothesis as desiccated phyllosiliciates

Both the 0.65 and 2.8 μm features could result from a highly desiccated Fe-phyllosilicate. The 0.65 μm feature matches the desiccated nontronite spectrum (Fig. 3.8), and, although

interlayer and adsorbed H_2O are removed from nontronites during desiccation, it is not possible to remove OH (present as metal-OH) without destroying the mineral's structure. The 2.8 μm metal-OH in association with the 0.65 μm feature could therefore be evidence that desiccated phyllosilicates are present on the moons' surface. Assuming the weak ~2.8 μm spectral feature is caused by a fundamental M-O-H vibration from a phyllosilicate, the combination/overtone bands at the shorter wavelengths will be much less intense (i.e. the 2.3 μm Fe-OH band that remains in the nontronite after heating and desiccation), consistent with their absence in CRISM data at a level greater than noise.

Phyllosilicates are a major phase in carbonaceous chondrite meteorites, and results from thermal infrared measurements by the Planetary Fourier Spectrometer (PFS) on MEx and Mars Global Surveryor's (MGS) Thermal Emission Spectrometer (TES) have also been interpreted as indicating the presence of phyllosilicates on parts of Phobos (Giuranna et al., 2011). Although (Giuranna et al., 2011) interpreted the phyllosilicate signature to be associated with the Phobos blue unit, visual comparison of the footprints of their spectra with CRISM color variations indicates a better match with the red unit. The blue unit is spectrally featureless in the thermal infrared, as it is in the near-infrared.

3.6.2 Exogenic hypotheses: nanophase Fe and solar wind implanted H

The second end member hypothesis is that the two features are from separate phases both formed through space weathering-related processes and produced on the moons' surfaces. The 0.65 μm feature can be replicated by a mixture of different sized metallic Fe particles, which are found on Earth's Moon as a product of space weathering (e.g. Pieters et al., 2000). While the presence of pyroxene and/or olivine could hide any nanophase Fe-related spectral curvature on the Moon, a broad ~0.7 μm feature similar to the 0.65-um band in dark material on Iapetus has

been modeled by competing scattering effects of microphase and nanophase metallic iron, possibly mixed with nanophase iron oxides (Clark et al., 2012).

To consider whether formation of metallic iron by space weathering of Phobos and Deimos is viable, we must assume some starting material. We again interpret the lack of detectable mafic absorptions on Phobos and Deimos and the moons' low albedo to suggest the starting material is best modeled as a primitive material, for example a CM carbonaceous chondrite (Fraeman et al., 2012). The maximum possible total iron available to later form metallic iron through interaction with H^+ from the solar wind in carbonaceous meteorites is 21-25% (Mason, 1963), equivalent to that in the most iron-rich lunar maria (Lawrence et al., 2002). Space weathering processes in carbonaceous materials is not understood, and there are no known examples of highly space weathered carbonaceous regolith in the meteorite collection in which to measure the effects directly. Laboratory experiments to simulate it using laser irradiation on the CM meteorite Mighei (Moroz et al., 2004a) demonstrate reddening and weakening of absorptions resulting from water and hydroxyl; microscopic examination of the laser-irradiated CM meteorite Mighei also shows that sub-microscopic metallic iron is produced (Shingareva et al., 2004). In contrast, in ion irradiation experiments on the organic component of terrestrial primitive materials, an initially red spectral slope becomes grayer resulting from production of elemental carbon (Moroz et al., 2004b).

In this scenario, the 2.8 μm metal-OH absorption is not caused by a phase indigenous to Phobos and Deimos, but rather forms on the moons' surfaces through processes involving interaction of H^+ from the solar wind with oxygen in the moons' regolith. A similar process is thought to be the cause of a 2.8 μm absorption observed on the Moon that is approximately the same strength as the features observed on Phobos and Deimos (Clark, 2009; Pieters et al., 2009;

Sunshine et al., 2009), and similar hydroxyl forming processes are predicted to be operate on all airless bodies in the solar system (McCord et al., 2011).

We also considered infall of hydrated and hydroxylated materials as a source for the 2.8 μm feature. The closest source of external material is ejecta from Mars, whose dust shows a complex spectral feature everywhere in the ~2.8 to ~3.0 μm region that has been interpreted to result from H_2O and metal-OH (Bell, 2008 and references therein). Presumably, much of the H_2O would be removed by desiccation when exposed to the space environment, leaving the metal-OH. However, dynamical modeling has shown Phobos is only likely to contain at most a few percent mass fraction Martian material, and Deimos would have even less (Chappaz et al., 2012). This small fraction is unlikely to make a significant change to the global spectral properties of the moons, and the smaller amount of Martian material predicted to be on Deimos is inconsistent with it having on average deeper absorption bands than Phobos. The hypothesis of Martian material as a source is also difficult to reconcile with the observations of other asteroids not in the Martian system that have a similar feature (Fig 3.7), so we conclude this explanation is unlikely.

3.7 SUMMARY

Mapping of mineral absorptions on Phobos and Deimos using visible / near infrared (0.4 - 4.0 μm) observations from CRISM shows that Fe^{2+} electronic absorptions diagnostic of olivine and pyroxene are not detectable on the moons' surfaces. CRISM data show a broad absorption centered around 0.65 μm within the red spectral units of both moons, and this feature is also evident in telescopic, Pathfinder, and Phobos-2 data for Phobos. CRISM data also show a 2.8 μm metal-OH combination absorption for both moons, with a shallower absorption associated with

the Phobos blue unit. The strength, position, and shape of both of these absorptions are similar to features seen on red, low albedo primitive asteroids through the solar system.

Two end-member hypotheses could explain the spectral features on Phobos and Deimos. The first invokes the presence of highly desiccated Fe-phyllosilicate minerals inherent to the Phobos and Deimos to explain the absorption features, and the second appeals to exogenic processes associated the solar wind that may create Fe and OH on the moons' surface. Expanded wavelength coverage in the far UV with remote sensing may provide further constraints on the moons' compositions, but in-situ exploration by a lander or through a returned sample will be the most robust way to ultimately determine the underlying causes for the pair of spectral features observed on Phobos and Deimos.

3.8 Acknowledgements

We thank NASA/JHUAPL for support on this work and the engineers and scientists associated with the CRISM operations center. This manuscript was improved based on insightful comments from E. Cloutis and one anonymous reviewer. We also acknowledge R. Binzel and C. Hergenrother for their assistance in collecting the Phobos telescopic spectra, and E. Howell for sharing her table of asteroids with features near 0.7 and 3.0 μm. AAF was funded by the Mr. and Mrs. Spencer T. Olin Fellowship for Women in Graduate Study.

3.9 FIGURES

Figure 3.1: Context HiRISE and CRISM images of Phobos and Deimos

(top) High spatial resolution context HiRISE observations of Phobos (PSP_007769_9010) and Deimos (ESP_012065_9000) and (bottom) CRISM observations acquired at similar illumination and viewing geometries for Phobos (FRT00002992_03) and Deimos (FRT00002983_03). The Phobos blue spectral unit is visible to the east of Stickney crater. Most of Phobos is covered by the red spectral unit that is spectrally similar to Deimos. Two additional CRISM observations of Phobos (FRT00002992_01 and FRT00002992_05) and Deimos (FRT00002983_01 and FRT00002983_05) are not shown but have similar viewing geometries.

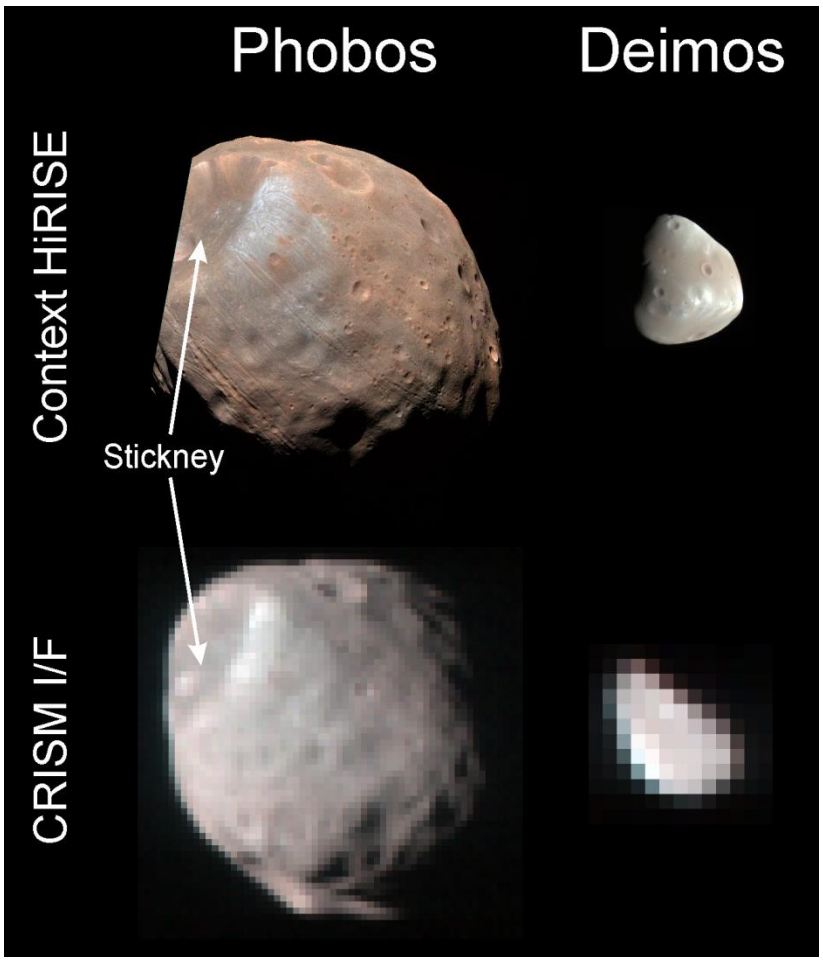

Figure 3.2: Representative CRISM I/F and SSA spectra from Phobos and Deimos

(a) Representative CRISM I/F spectra from regions of interest covering the Phobos red and blue units and Deimos. The Deimos spectrum is brighter than the Phobos spectra because it was acquired at a lower phase angle and the moons have backscattering surfaces. (b) Derived single scattering albedo spectra (SSA) for the same regions, by definition independent of lighting and viewing geometries.

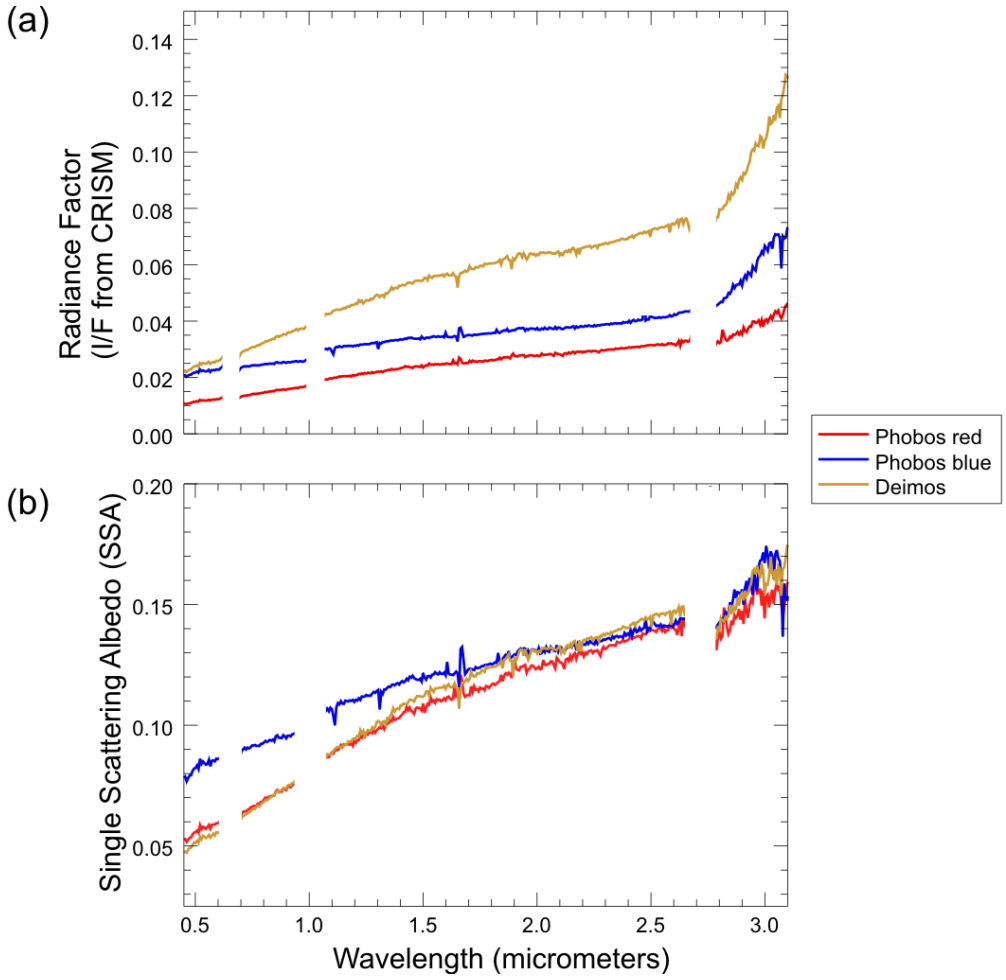

Figure 3.3: Mineral parameter maps of CRISM Phobos and Deimos data

Mineral parameter maps generated from CRISM Phobos and Deimos single scattering albedo observations. There is no evidence for features above the noise in parameter maps for low- and high-calcium, pyroxene, olivine, and 1.9 μm (molecular H_2O), but there is a signature for a band at 0.65 μm that is spatially correlated with the red-blue index. There is also a ubiquitous 2.8 μm band that is on average deeper in the Phobos red unit and Deimos than the Phobos blue unit.

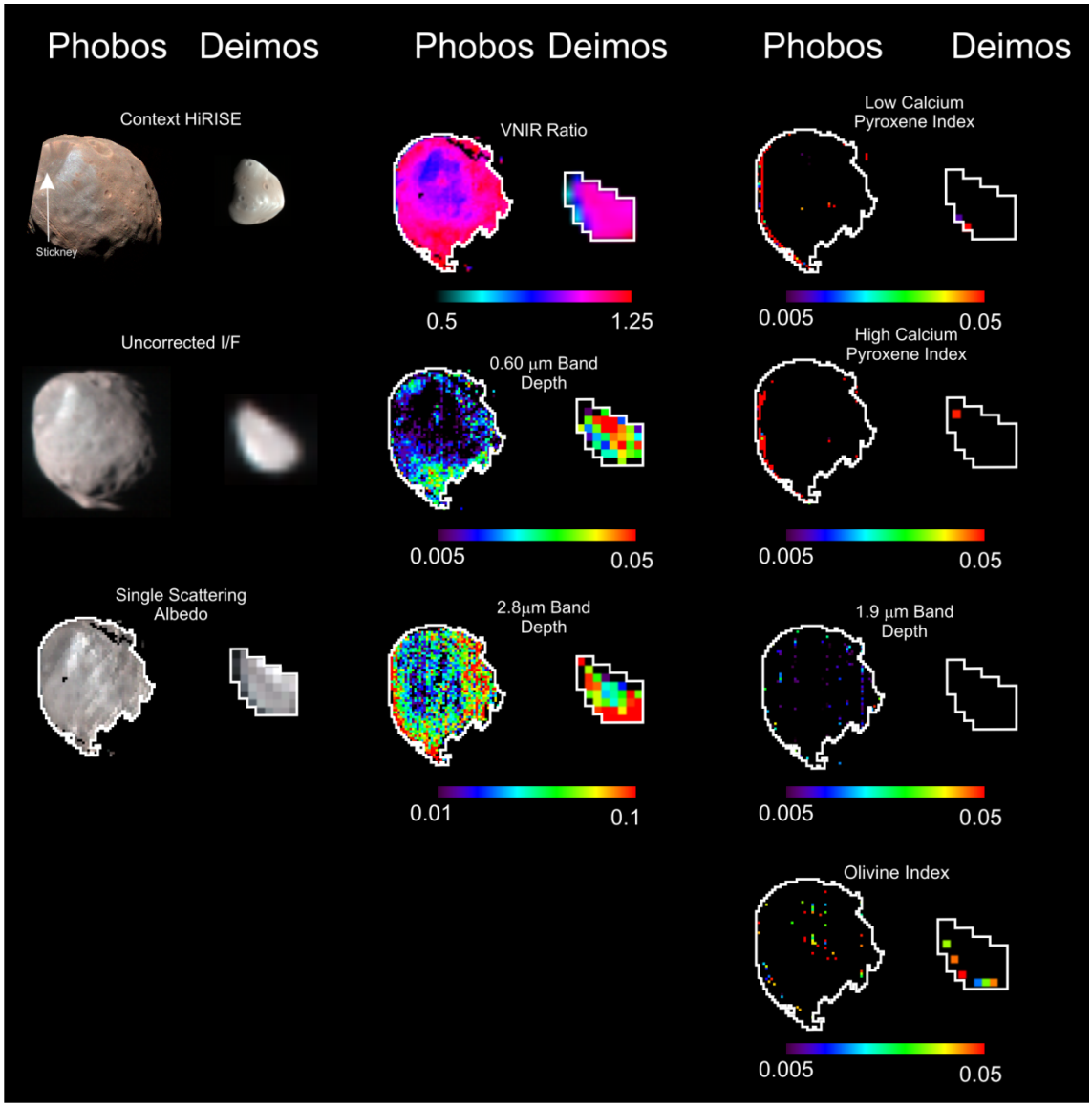

Figure 3.4: SSA and telescopic spectra showing absorption at 0.65 μm in Phobos Red Unit (a) Single scattering albedo (SSA) scaled to 0.55 μm and offset for clarity comparing CRISM and telescopic data over Phobos' blue and red units and Deimos. The CRISM data are averages of multiple pixels from each region from the disk-resolved image. The disk-integrated telescopic data are centered over Phobos' red (92° longitude) and blue (74° longitude) units. Dashed lines are linear continuums from 0.5 – 0.85 μm. (b) Same spectra continuum removed. The CRISM Phobos red unit, Deimos, and telescopic red unit dominated spectra all show a feature centered near 0.65 μm having a consistent width and depth.

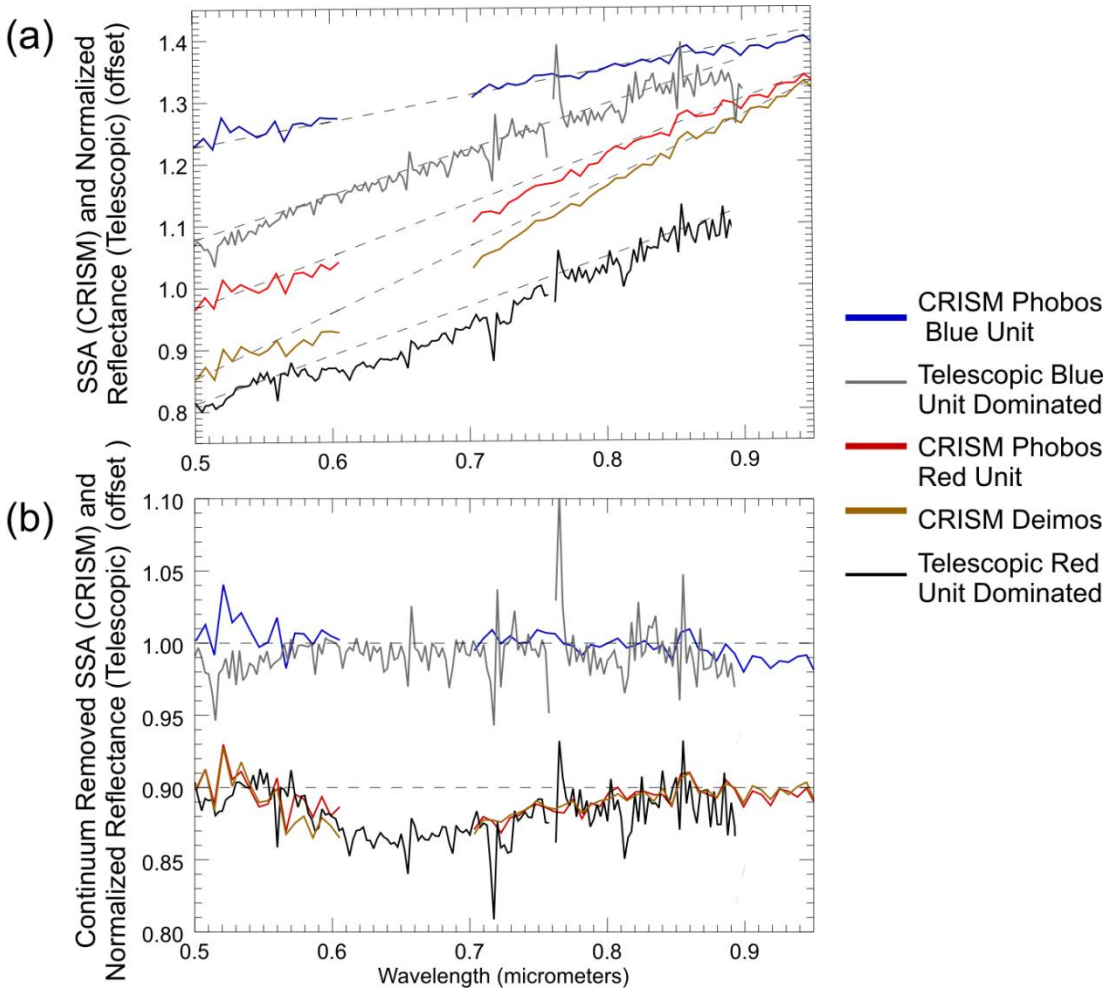

Figure 3.5: Thermally corrected CRISM SSA spectra showing absorption near 2.7 μm

CRISM single scattering albedo (SSA) scaled to 1.55 μm and offset for clarity showing spectra over Phobos' blue and red units and Deimos (thin, pale lines). Spectra that have been smoothed using a 5x5 median filter (heavy line) are over plotted. The spectra all show a feature centered near 2.8 μm that is slightly deeper in the Phobos red unit and Deimos than in the Phobos blue unit.

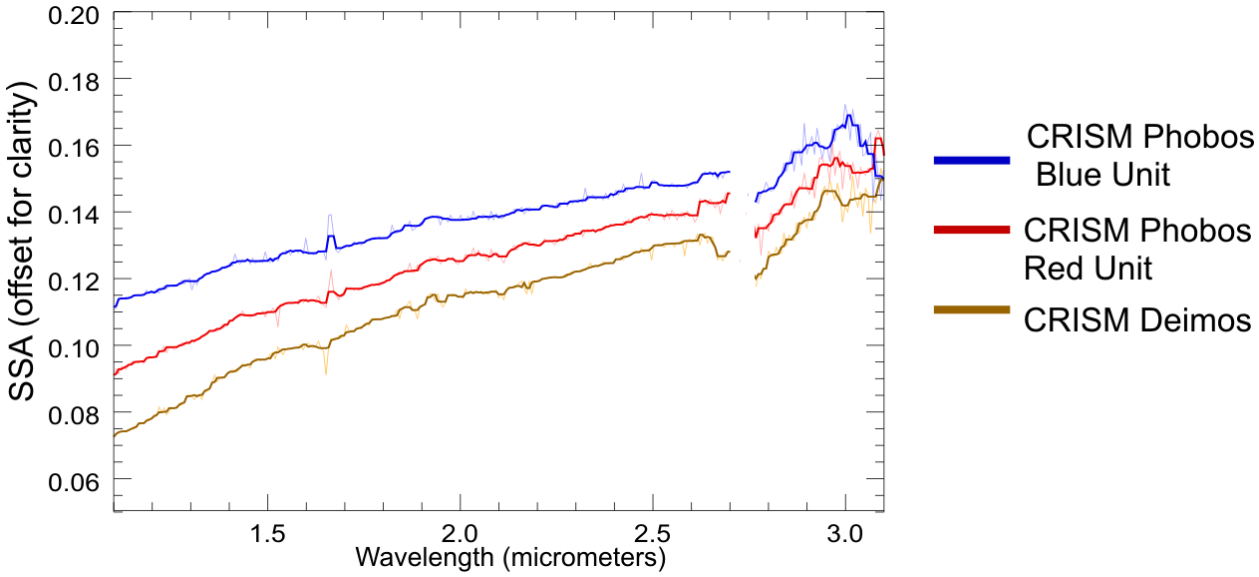

Figure 3.6: Asteroid spectra with 0.65 µm feature

Linear continuum removed (a) and scaled (b) asteroid normalized reflectance spectra having similar 0.65 features µm to Phobos' red unit and Deimos. Asteroid spectra are from the Vilas asteroid survey (Vilas et al., 1998) Spectra in (a) have been fit with a 5th order polynomial (heavy dotted line) to emphasize the width and location of the band near 0.65 µm.

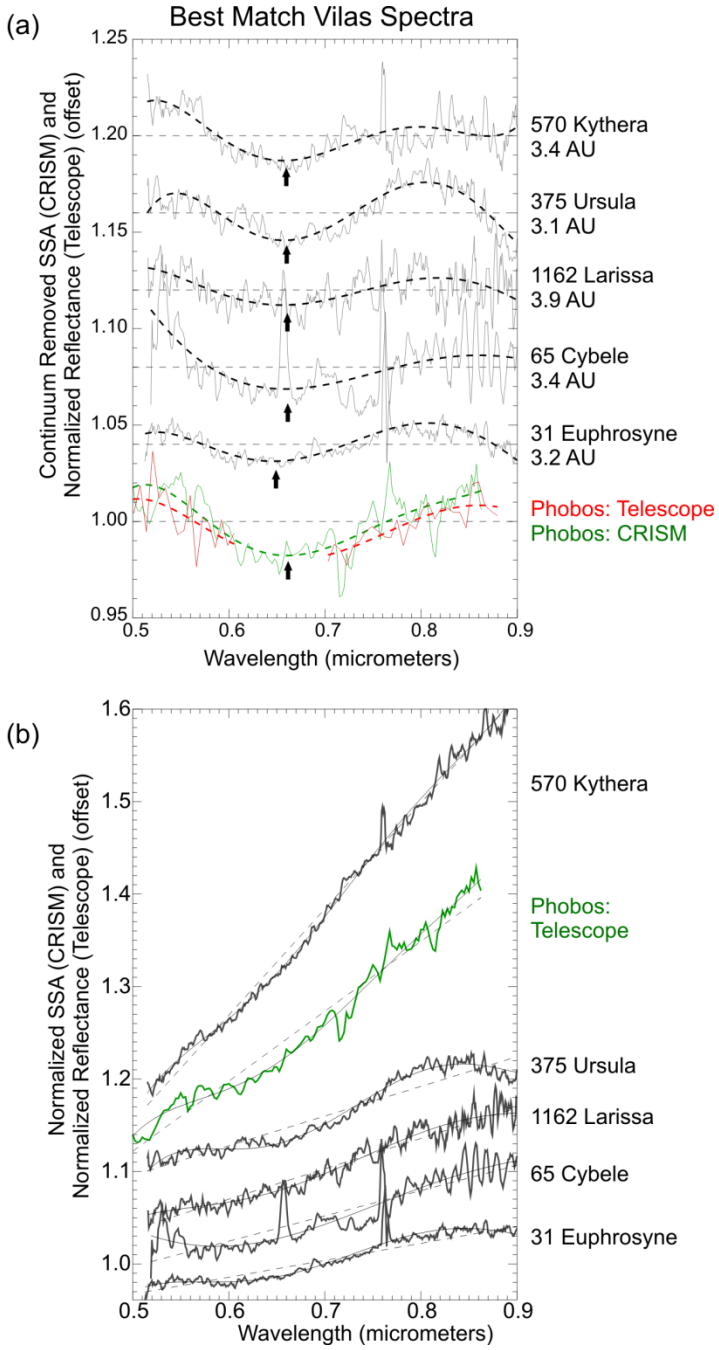

Figure 3.7: Asteroid spectra with 2.7 μm feature

Scaled normalized reflectance asteroid spectra having similar 2.8 μm features to Phobos and Deimos. Asteroid spectra have been binned by a factor of 9 from original data and corrected using beaming parameters of 0.900 (Stereoskopia), 0.975 (Aegle), 0.800 (Egeria), and 0.950 (Nemausa) (discussion of data reduction techniques in Rivkin et al., 2011).

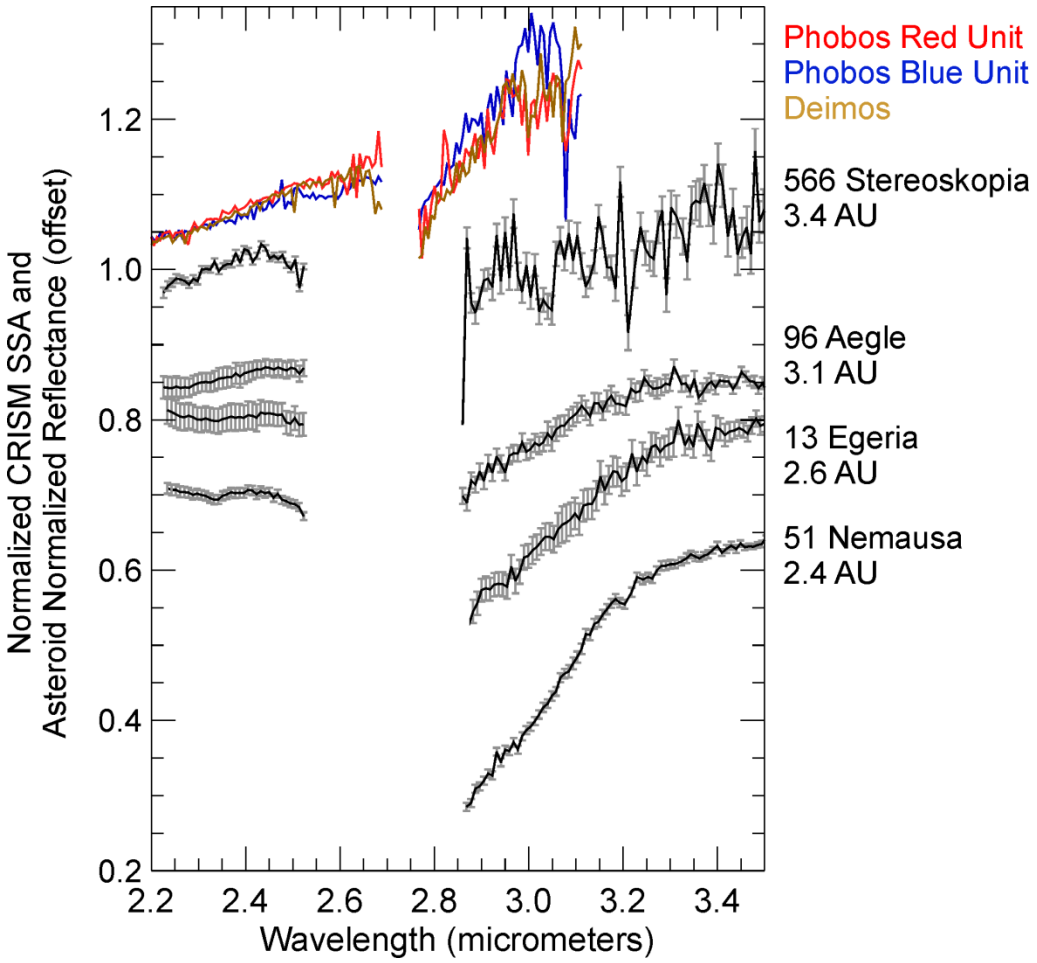

Figure 3.8: Comparison of CRISM Phobos red unit spectra to laboratory analogs and models

(a) Comparison of Phobos red unit CRISM (red) and telescopic spectra (green) to Fe-phyllosilicates cronstedtite (USGS spectral library sample M3542), nontronite (PHY07) at room temperature (Morris et al., 2010 sample A2D05711) and heated to 105 C for 451 hr. (Morris et al., 2010 sample A2D06206). CRISM Phobos single scattering albedo data have been modeled at laboratory viewing geometry. Deimos spectra not shown to improve clarity of figure. (b) Comparison to model with iron particles of varying sizes, described in text. (c) Linear continuum removed versions of all spectra highlighting position of band near 0.65 μm.

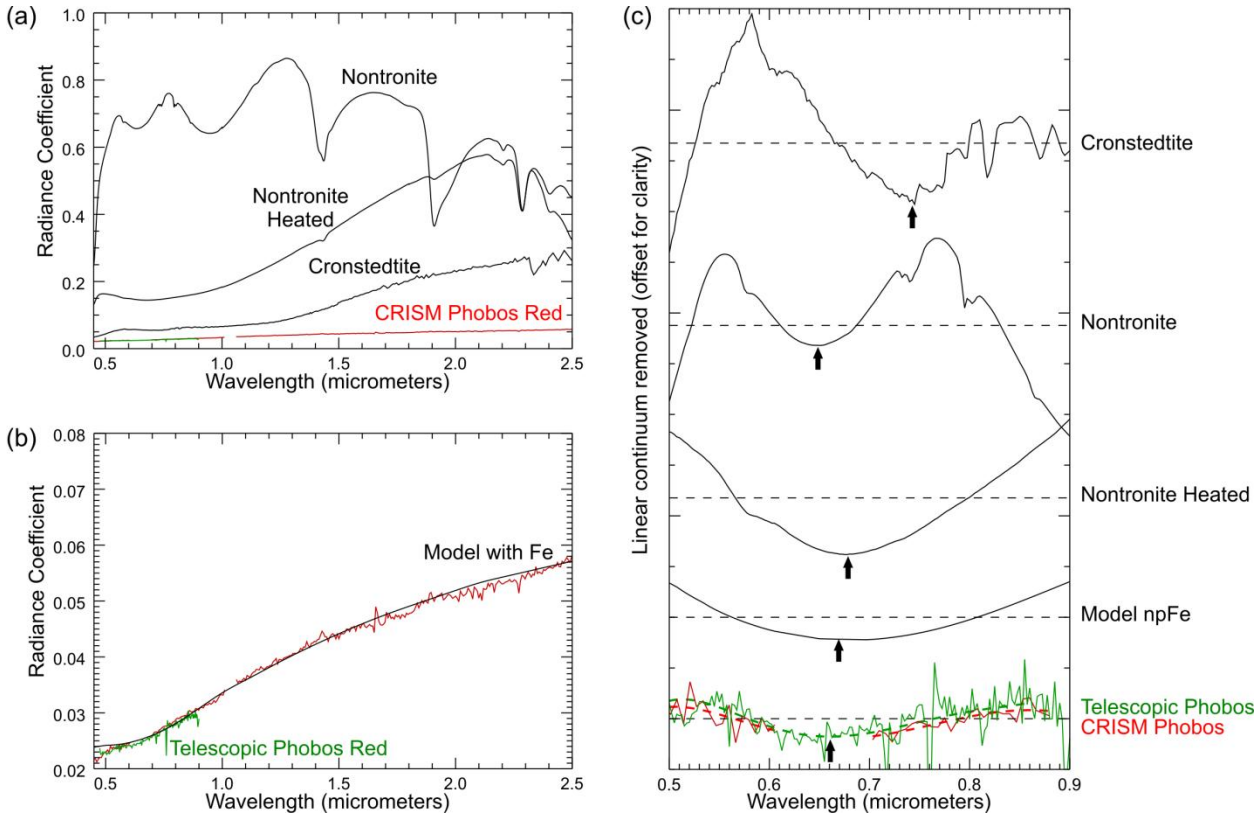

3.10 REFERENCES CITED

Bell, J., 2008. The Martian Surface. Cambridge, UK: Cambridge University Press.

Bibring, J.-P., et al, 2004. OMEGA: Observatoire pour la Minéralogie, l'Eau, les Glaces et l'Activité. Mars Express: the Scientific Payload, Eur. Space Agency Spec. Publ. 1240, 37–49.

Binzel, R.P., Harris, A.W., Schelte, J.B., Burbine, T.H, 2001. Spectral properties of near-Earth objects: Palomar and IRTF results for 48 objects including spacecraft targets (9969) Braille and (10302) 1989 ML. Icarus 151, 134-149. doi: 10.1006/icar.2001.6613.

Binzel, R.P., Rivkin, A.S., Scott, S. J., Harris, A.W., Bus, S.J., Burbine, T.H, 2004. Observed spectral properties of near-Earth objects: results for population distribution, source regions, and space weathering processes. Icarus 170, 259-294. doi: 10.1016/j.icarus.2004.04.004.

Burns, J.A., 1992. Contradictory clues as to the origin of the Martian moons. Mars, 1283–1301.

Cahill, J., Blewett, D., Nguyen, N., Xu, K., Kirillov, O., Lawrence, S., Denevi, B., Coman, E. 2012. Determination of iron metal optical constants: Implications for ultraviolet, visible, and near-infrared remote sensing of airless bodies. Geophysical Research Letters, 39, L10204. doi: 10.1029/2012GL051630.

Calvin, W.M., King, T.V.V., 1997. Spectral characteristics of iron-bearing phyllosilicates: Comparison to Orgueil (CI1), Murchison and Murray (CM2). Meteoritics & Planetary Science 32, 693–701. doi: 10.1111/j.1945-5100.1997.tb01554.

Castillo-Rogez, J.C., Pavone, M., Nesnas, I.A.D., Hoffman, J.A., 2012. Expected science return of spatially-extended in-situ exploration at small Solar system bodies, 2012 IEEE Aerospace Conference, 1–15.

Chappaz, L., Melosh, H.J., Vaquero, M., Howell, K.C., 2012. Material transfer from the surface of Mars to Phobos and Deimos. 43rd Lunar and Planetary Institute Science Conference, abstract #1422.

Clark, R.N., 2009. Detection of Adsorbed Water and Hydroxyl on the Moon. Science 326, 562–564. doi: 10.1126/science.1178105.

Clark, R.N., Roush, T.L., 1984. Reflectance spectroscopy: Quantitative analysis techniques for remote sensing applications. Journal of Geophysical Research: Solid Earth 89, 6329–6340. doi: 10.1029/JB089iB07p06329.Clark, R.N., Cruikshank, D.P., Jaumann, R., Brown, R.H., Stephan, K., Dalle Ore, C.M., Eric Livo, K., Pearson, N., Curchin, J.M., Hoefen, T.M., Buratti, B.J., Filacchione, G., Baines, K.H., Nicholson, P.D., 2012. The surface composition of Iapetus: Mapping results from Cassini VIMS. Icarus 218, 831–860. doi: 10.1016/j.icarus.2012.01.008.

Clark, R.N., King, T.V.V., Klejwa, M., Swayze, G.A., Vergo, N., 1990. High Spectral Resolution Reflectance Spectroscopy of Minerals. J. Geophys. Res. 95, 12,653–12,680. doi: 10.1029/JB095iB08p12653.

Clark, R.N., Pieters, C.M., Green, R.O., Boardman, J.W., Petro, N.E., 2011. Thermal removal from near-infrared imaging spectroscopy data of the Moon. Journal of Geophysical Research: Planets 116, E00G16 . doi: 10.1029/2010JE003751.

Clark, R.N., Swayze, G.A., Wise, R., Livo, K.E., Hoefen, T. M., Kokaly, R.F., Sutley, S.J., 2003. USGS Digital Spectral Library Splib05a: US Geological Survey Open-File Report 03-395. <http://pubs.usgs.gov/of/2003/ofr-03-395>.

Clark, R.N., Swayze, G.A., Wise, R., Livo, K.E., Hoefen, T. M., Kokaly, R.F., Sutley, S.J., 2007. USGS Digital Spectral Library Splib06a: US Geological Survey, Data Series 231. <http://speclab.cr.usgs.gov/spectral-lib.html>.

Cloutis, E.A., Hudon, P., Hiroi, T., Gaffey, M.J., Mann, P., 2011. Spectral reflectance properties of carbonaceous chondrites: 2. CM chondrites. Icarus 216, 309–346. doi:10.1016/j.icarus.2011.09.009.

Fraeman, A.A., Arvidson, R.E., Murchie, S.L., Rivkin, A., Bibring, J.-P., Choo, T.H., Gondet, B., Humm, D., Kuzmin, R.O., Manaud, N., Zabalueva, E.V., 2012. Analysis of disk-resolved OMEGA and CRISM spectral observations of Phobos and Deimos. J. Geophys. Res. 117, E00J15. doi:10.1029/2012JE004137.

Giuranna, M., Roush, T.L., Duxbury, T., Hogan, R.C., Carli, C., Geminale, A., Formisano, V., 2011. Compositional interpretation of PFS/MEx and TES/MGS thermal infrared spectra of Phobos. Planetary and Space Science 59, 1308–1325. doi:10.1016/j.pss.2011.01.019.

Goguen, J., Veverka, J., Duxbury, T. 1979. Marsshine on Phobos. Icarus 37, 377-388. doi:10.1016/0019-1035(79)90002-2.

Hapke, B., 1993. Theory of reflectance and emittance spectroscopy. Cambridge University Press, Cambridge, UK.

Hunten, D.M., 1979. Capture of Phobos and Deimos by photoatmospheric drag. Icarus 37, 113–123. doi:10.1016/0019-1035(79)90119-2.

Jarvis, K.S., Vilas, F., Gaffey, M.J., 1993. Iron oxide bands in the visible and near-infrared reflectance spectra of primitive asteroids. 24th Lunar and Planetary Institute Science Conference Abstracts, 715–716.

King, T.V.V., Clark, R.N., 1998. The Presence of A Single Absorption Feature: What It Does and Doesn't Imply. 28th Lunar and Planetary Science Institute Science Conference Abstracts, abstract #1848.

Kuzmin, R.O., Zabalueva, E.V., 2003. The temperature regime of the surface layer of the Phobos regolith in the region of the potential Fobos-Grunt space station landing site. Solar System Research 37, 480–488. doi:10.1023/B:SOLS.0000007946.02888.bd.

Landolt, A.U., 1992. Broadband UBVRI photometry of the Baldwin-Stone Southern Hemisphere spectrophotometric standards. The Astronomical Journal 104, 372–376. doi:10.1086/116243.

Lawrence, D.J., Feldman, W.C., Elphic, R.C., Little, R.C., Prettyman, T.H., Maurice, S., Lucey, P.G., Binder, A.B., 2002. Iron abundances on the lunar surface as measured by the Lunar Prospector gamma-ray and neutron spectrometers. Journal of Geophysical Research: Planets 107, 13-1 -- 13-6. doi: 10.1029/2001JE001530.

Lynch, D.K., Russell, R.W., Rudy, R.J., Mazuk, S., Venturini, C.C., Hammel, H.B., Sykes, M.V., Puetter, R.C., Perry, R.B., 2007. Infrared Spectra of Deimos (1-13 μm) and Phobos (3-13 μm). The Astronomical Journal 134, 1459–1463. doi: 10.1086/519975.

Mason, B., 1963. The carbonaceous chondrites. Space Sci Rev 1, 621–646.

McCord, T.B., Taylor, L.A., Combe, J.-P., Kramer, G., Pieters, C.M., Sunshine, J.M., Clark, R.N., 2011. Sources and physical processes responsible for OH/H2O in the lunar soil as revealed by the Moon Mineralogy Mapper (M3). Journal of Geophysical Research: Planets 116. doi: 10.1029/2010JE003711.

Milliken, R.E., Rivkin, A.S., 2009. Brucite and carbonate assemblages from altered olivine-rich materials on Ceres. Nature Geosci 2, 258–261. doi: 10.1038/ngeo478.

Moroz, L.V., Hiroi, T., Shingareva, T.V., Basilevsky, A.T., Fisenko, A.V., Semjonova, L.F., Pieters, C.M., 2004a. Reflectance Spectra of CM2 Chondrite Mighei Irradiated with Pulsed Laser and Implications for Low-Albedo Asteroids and Martian Moons. 35th Lunar and Planetary Institute Science Conference Abstracts, abstract # 1279.

Moroz, L., Baratta, G., Strazzulla, G., Starukhina, L., Dotto, E., Barucci, M.A., Arnold, G., Distefano, E., 2004b. Optical alteration of complex organics induced by ion irradiation:: 1. Laboratory experiments suggest unusual space weathering trend. Icarus 170, 214–228. doi: 10.1016/j.icarus.2004.02.003.

Morris, R.V., Jr, H.V.L., Lawson, C.A., Jr, E.K.G., Nace, G.A., Stewart, C., 1985. Spectral and Other Physicochemical Properties of Submicron Powders of Hematite (α-Fe2O3), Maghemite (γ-Fe2O3), Magnetite (Fe3O4), Goethite (α-FeOOH), and Lepidocrocite (γ-FeOOH). J. Geophys. Res. 90, 3126–3144. doi:10.1029/JB090iB04p03126.

Morris, R.V., Ming, D.W., Golden, D.C., Graff, T.G., Achilles, C.N., 2010. Evidence for Interlayer Collapse of Nontronite on Mars from Laboratory Visible and Near-IR Reflectance Spectra. 41st Lunar and Planetary Science Conference, abstract # 2156.

Murchie, S., Erard, S., 1996. Spectral Properties and Heterogeneity of Phobos from Measurements byPhobos 2. Icarus 123, 63–86. doi:10.1006/icar.1996.0142.

Murchie, S., et al, 2007. Compact Reconnaissance Imaging Spectrometer for Mars (CRISM) on Mars Reconnaissance Orbiter (MRO). J. Geophys. Res. 112. doi:200710.1029/2006JE002682.

Murchie, S., Eng., D., Chabot, N., Guo, Y., Arvidson, R., Yen, A., Trebi-Ollennu, A., Seelos, F., Adams, E., Fountain, G, 2014. MERLIN: Mars-Moons exploration, reconnaissance and

landed investigation. Acta Astronautica 93, 475-482. doi: 10.1016/j.actaastro.2012.10.014.

Murchie, S., Thomas, N., Britt, D., Herkenhoff, K., Bell, J.F., 1999. Mars Pathfinder spectral measurements of Phobos and Deimos: Comparison with previous data. Journal of Geophysical Research: Planets 104, 9069–9079. doi: 10.1029/98JE02248.

Murchie, S.L., Choo, T., Humm, D., Rivkin, A.S., Bibring, J.-P., Langevin, Y., Gondet, B., Roush, T.L., Duxbury, T., Team, C., 2008. MRO/CRISM Observations of Phobos and Deimos, 39th Lunar and Planetary Institute Science Conference Abstracts, abstract #1434.

Muscatello, A.C., Mueller, R., Sanders, G.B., Larson, W.E., 2012. Phobos and Deimos Sample Collection and Prospecting Missions for Science and ISRU. LPI Contributions 1679, 4296.

Noble, S.K., Pieters, C.M., Keller, L.P., 2007. An experimental approach to understanding the optical effects of space weathering. Icarus 192, 629–642. doi: 10.1016/j.icarus.2007.07.021.

Ordal, M.A., Bell, R.J., Alexander, J., Long, L.L., Querry, M.R., 1985. Optical properties of fourteen metals in the infrared and far infrared: Al, Co, Cu, Au, Fe, Pb, Mo, Ni, Pd, Pt, Ag, Ti, V, and W. Applied Optics 24, 4493–4499. doi: 10.1364/AO.24.004493.

Pelkey, S.M., Mustard, J.F., Murchie, S., Clancy, R.T., Wolff, M., Smith, M., Milliken, R., Bibring, J.-P., Gendrin, A., Poulet, F., Langevin, Y., Gondet, B., 2007. CRISM multispectral summary products: Parameterizing mineral diversity on Mars from reflectance. J. Geophys. Res. 112. doi:200710.1029/2006JE002831.

Pieters, C.M., et al, 2009. Character and Spatial Distribution of OH/H2O on the Surface of the Moon Seen by M3 on Chandrayaan-1. Science 326, 568–572. doi:10.1126/science.1178658.

Pieters, C.M., Taylor, L.A., Noble, S.K., Keller, L.P., Hapke, B., Morris, R.V., Allen, C.C., McKAY, D.S., Wentworth, S., 2000. Space weathering on airless bodies: Resolving a mystery with lunar samples. Meteoritics & Planetary Science 35, 1101–1107. doi:10.1111/j.1945-5100.2000.tb01496.x.

Rivkin, A.S., 2007. The Composition of Phobos and Deimos: Constraints and Questions. Exploration of Phobos and Deimos, 33.

Rivkin, A.S., Brown, R.H., Trilling, D.E., Bell III, J.F., Plassmann, J.H., 2002. Near-Infrared Spectrophotometry of Phobos and Deimos. Icarus 156, 64–75. doi:10.1006/icar.2001.6767.

Rivkin, A.S., Clark, B.E., Ockert-Bell, M., Volquardsen, E., Howell, E.S., Bus, S.J., Thomas, C.A., Shepard, M., 2011. Asteroid 21 Lutetia at 3 μm: Observations with IRTF SpeX. Icarus 216, 62–68. doi: 10.1016/j.icarus.2011.08.009.

Rivkin, A.S., Emery, J.P., 2010. Detection of ice and organics on an asteroidal surface. Nature 464, 1322–1323. doi: 10.1038/nature09028.

Rivkin, A. S., Howell, E.S., Vilas, F., Lebofksy, L.A., 2002. Hydrated Minerals on Asteroids: The Astronomical Record, in: Asteroids III. University of Arizona Press, p. 785.

Sasaki, S., 1990. Origin of Phobos--Aerodynamic Drag Capture by the Primary Atmosphere of Mars. 21st Lunar and Planetary Institute Science Conference Abstracts, abstract # 1069.

Shingareva, T.V., Basilevsky, A.T., Fisenko, A.V., Semjonova, L.F., Korotaeva, N.N., 2004. Mineralogy and Petrology of Laser Irradiated Carbonaceous Chondrite Mighei. 35th Lunar and Planetary Institute Science Conference Abstracts, abstract # 1137.

Sunshine, J.M., Farnham, T.L., Feaga, L.M., Groussin, O., Merlin, F., Milliken, R.E., A'Hearn, M.F., 2009. Temporal and Spatial Variability of Lunar Hydration As Observed by the Deep Impact Spacecraft. Science 326, 565–568. doi:10.1126/science.1179788.

Takir, D., Emery, J.P., Mcsween, H.Y., Hibbitts, C.A., Clark, R.N., Pearson, N., Wang, A., 2013. Nature and degree of aqueous alteration in CM and CI carbonaceous chondrites. Meteoritics & Planetary Science. doi:10.111/maps.12171.

Vilas, F., 1994. A Cheaper, Faster, Better Way to Detect Water of Hydration on Solar System Bodies. Icarus 111, 456–467. doi:10.1006/icar.1994.1156.

Vilas, F., Gaffey, M., 1989. Phyllosilicate Absorption Features in Main-Belt and Outer-Belt Asteroid Reflectance Spectra. Science 246, 790–792.

Vilas, F., Jarvis, K.S., Gaffey, M.J., 1994. Iron Alteration Minerals in the Visible and Near-Infrared Spectra of Low-Albedo Asteroids. Icarus 109, 274–283. doi:10.1006/icar.1994.1093.

Vilas, F., Larson, S.M., Hatch, E., Jarvis, K.S., 1993. CCD Reflectance Spectra of Selected Asteroids. II. Low-Albedo Asteroid Spectra and Data Extraction Techniques. Icarus 105, 67–78. doi:10.1006/icar.1993.1111.

Vilas, F., Smith, B., McFadden, L., Gaffey, M.J., Larson, S.M., Hatch, E., Jarvis, K.S., 1998. Vilas Asteroid Spectra V1.1. EAR-A-3-RDR-VILAS-ASTEROID-SPECTRA-V1.1. NASA Planetary Data System.

Chapter 4: A Hematite-Bearing Layer in Gale Crater: Mapping and Implications for Past Aqueous Conditions

Associated Publication: Fraeman, A., Arvidson, R., Catalano, J., Grotzinger, J., Morris, R., Murchie, S., Seelos, F., Seelos, K., McGovern, J., Humm, D., Stack, K., Viviano, C. 2013. "A hematite-bearing layer in Gale Crater: mapping and implications for past aqueous conditions," *Geology*, 41, 1103-1106, doi:10.1130/G43613.1

ABSTRACT

Oversampled CRISM visible/near-infrared hyperspectral data over Mt. Sharp in Gale Crater were used to generate spatially sharpened maps of the location of red crystalline hematite within the uppermost stratum of a ~6.5 km long ridge on the mound's northern flank. Finely layered strata underlie the ridge to the north and have dips consistent with the nearby Mt. Sharp sedimentary sequence. Fe/Mg smectites are exposed in a valley to the south of the ridge. Emplacement of the hematite is hypothesized to result either from exposure of anoxic Fe^{+2}-rich groundwater to an oxidizing environment, leading to precipitation of hematite or its precursors, or from in place weathering of precursor silicate materials under oxidizing conditions. These hypotheses and implications for habitability will be testable with in situ measurements by the Curiosity Mars Rover when it reaches Mt. Sharp.

4.1 INTRODUCTION

In August 2012 the Mars Science Laboratory (MSL) rover Curiosity landed in Gale Crater, a ~155 km diameter impact crater located near the Martian hemispheric dichotomy. Gale Crater was selected as the landing site largely due to the presence of a ~5 km high mound of layered rock in its center named Mt. Sharp (formally Aeolis Mons) (Grotzinger et al., 2012). Hyperspectral data acquired by the Mars Reconnaissance Orbiter (MRO) Compact

Reconnaissance Imaging Spectrometer for Mars (CRISM) indicates that Mt. Sharp contains a stratigraphic sequence with Fe/Mg smectites in the lowest layers that transition upwards to layers with hydrated sulfates (e.g., Milliken et al., 2010). The uppermost strata of the mound contain only anhydrous minerals (Milliken et al., 2010; Grotzinger et al., 2012). The extensive stratigraphic section exposed in Mt. Sharp provides Curiosity with the opportunity to characterize bedrock that was emplaced during periods of global-scale environmental changes on Mars (Thomson et al., 2011).

Hematite was first observed in Mt. Sharp by Milliken et al., (2010) who noted its presence mixed within the hydrated sulfate strata. The CRISM data used by Milliken et al. (2010) for mineral mapping were acquired in a full resolution targeted (FRT) mode (Murchie et al., 2007) with a pixel size of ~18 m. Subsequent to that work, the gimbaled CRISM optical system was operated to oversample some scenes in the along-track direction, i.e., to collect spectra at sub-pixel intervals in the along-track direction. This oversampled mode allows enhanced spatial resolution mapping of mineral spectral signatures.

Here we introduce spatial sharpening techniques for an oversampled observation centered on a ridge running along the northern flank of Mt. Sharp (Fig. 4.1). We use the results to generate the highest spatial resolution map to-date of a hematite deposit that is localized in the uppermost stratum of the ridge. Using updated parameter mapping from FRT data (Seelos et al., 2013), we also find the ridge deposits are relatively dehydrated compared to surrounding materials. We propose two possible formation environments for the hematite that can be tested by Curiosity while simultaneously addressing Curiosity's mission objectives to search for habitable environments. This region is projected to be among the first Mt. Sharp deposits traversed by Curiosity (Grotzinger et al., 2012) (Fig 4.1).

4.2 Spatial Processing of CRISM Along-Track Oversampled Data

CRISM operates analogously to a line scanner where incoming spectral radiance enters spectrometer optics through a narrow slit and is split into short-wavelength (S, 0.41–1.03 μm) and long-wavelength (L, 1.03–3.92 μm) ranges. High-resolution targeted observations have pixel footprints determined by CRISM's instantaneous field of view of 61.5 μrad cross-track (~18 m projected onto the surface). Along-track pixel spacing is governed by integration time, the along-track velocity of MRO, and extent to which a gimbal compensates for MRO's motion. In standard FRT observations, pixels are collected at sampling intervals of ~61.5 μrad along-track to "square" the pixels. In along-track oversampled observations (ATOs), the gimbal sampling interval is commanded to be <<61.5 μrad between image lines to provide spatial overlap needed to support image sharpening. Spacing between pixels for the ATO used in this paper (FRT00021C92) ranges from ~1 m to ~18 m across the scene when projected onto the surface.

One advantage of ATOs is the ability to generate map products with smaller pixel sizes than standard FRTs. We use the built-in geometric lookup table (super-GLT) mapping in ENVI software to produce products with resolutions as low as ~6 m/pixel in the along-track direction. The super-GLT processing method creates a spatial filter for a projection at a specified spatial resolution and then averages data near the filter centers weighted by 1/pixel distance from the filter center. This procedure assumes a minimum number of real data values are present within the filter area, otherwise the resulting central pixel value is left as 0. We run this process sequentially with 6, 9, 12, 15, and 18 m/pixel spatial filters and keep the highest resolution data where it exists.

4.3 Mapping of Crystalline Hematite and Additional Mineral Phases

The use of mineral parameter maps to identify areas for spectral analysis has proven valuable in the analysis of CRISM data (Pelkey et al., 2007, Seelos et al., 2013). Thus we have generated parameter maps from atmospherically corrected I/F (radiance/(solar irradiance/$\boldsymbol{\pi}$)) spectral cubes for the processed ATO scene. Atmospheric corrections were applied using the standard "volcano-scan" method, which divides spectra containing atmospheric contributions by a scaled atmospheric transmission spectrum collected over Olympus Mons (e.g., Murchie et al., 2009). In addition to parameter maps from the ATO observation, we have also examined newly processed parameter maps from earlier FRT observations acquired without oversampling but with much colder detector temperatures than the ATO data (Seelos et al., 2013). These parameter maps were generated by explicit modeling of atmospheric and surface radiances to isolate surface mineral signatures. ATO parameter maps are similar to the FRT products, although the L-detector based ATO data are noisier due to warmer detector temperatures.

Results are similar to Milliken et al., (2010) in that they show Fe/Mg smectites located in a valley south of the ridge of interest and hydrated phases on the dissected strata north of the ridge, although in contrast to the previous work, the ridge itself appears less hydrated than the surrounding strata (Fig. 4.2a). The innovation of the along-track oversampling becomes apparent in S-detector based parameter maps covering the ridge, which runs approximately perpendicular to the cross-track direction and therefore benefits from oversampling in this direction. The enhanced resolution of the ATO data coupled with overlays onto 0.25 m/pixel (High Resolution Imaging Science Experiment) HiRISE image data show that a 0.86 μm absorption feature is associated with the uppermost stratum on the southern side of the ridge (Fig. 4.2b, 4.3b).

Red crystalline hematite is characterized by a feature at 0.86 μm as well as two electronic transition bands near 0.55 and 0.64 μm and a relative reflectivity maximum at 0.75 μm (e.g. Morris et al., 1985) (Fig. 4.4). I/F spectra averaged over hundreds of pixels from the southern side of the ridge and normalized by the average spectrum in each image column (to minimize instrument artifacts and enhance local spectral variations) show pixels within this area have bands near 0.55 and 0.86 μm as well as a maximum at 0.75 μm, consistent with the laboratory spectra of red hematite (Fig. 4.4). The depth of the 0.86 μm band increases as the depth of the 0.55 μm band increases and the maximum at 0.75 μm is unique to normalized spectra at the ridge, further indicating the presence of hematite in this region. Unfortunately, the presence of the 0.64 μm band cannot be confirmed because of a wavelength gap in the CRISM S-detector (Murchie et al., 2007). Non-normalized I/F spectra also display these characteristics, although absorption features are less prominent due to the ubiquitous contamination by wind-blown dust and sands.

4.4 Hematite Ridge Geology Setting and Formation Hypotheses

The extensive mineral signatures near the ridge (Fig. 4.2) may result from the proximity of these exposures to the mouth of a large trough extending southward up Mt. Sharp (labeled in Fig. 4.1). Water and/or winds have likely stripped this region, keeping surfaces relatively free of dust and leaving the erosion-resistant, hematite-bearing ridge intact. The ridge is ~200 m wide and extends ~6.5 km NE-SW, running approximately parallel with the base of Mt. Sharp (Fig. 4.1). To the west, the ridge transitions to an escarpment overlain by younger strata; to the east, debris flows from Mt. Sharp cover and obscure the ridge. The upper ridge is defined by multiple layers exposed where the ridge is partially eroded (Fig. 4.2b), and the hematite signature maps most closely to the southern and uppermost layer of the ridge (Fig. 4.2b, 4.3b). Due to the

northwest dip of the ridge strata, the upslope (southern) edge of the ridge is a few meters higher than the downslope (northern) side and rises ~10 m above the phyllosilicate-bearing trough directly upslope. The southern side of the ridge is similar in elevation to the lowest layers in the sulfate-bearing unit south of the phyllosilicate-bearing trough (Fig. 4.2a, 4.3b). Bedding orientations were measured at 42 locations along the ridge using HiRISE orthoimages and digital elevation models. Beds dip to the northwest at an average dip of 7.1º with a standard deviation of 2.5º. Bedding orientations were also measured at 12 locations within the sulfate-bearing strata , and beds in this unit display an average dip of 6.4º with a standard deviation of 2.9º (Fig. 4.3). The similarity between the bedding orientation measurements within the ridge and in the strata above and below it imply that the ridge strata are likely part of the original Mt. Sharp stratigraphic sequence.

That the strata in the ridge are conformable with nearby layers in Mt. Sharp and the fact that there are no obvious nearby fractures suggests the hematite is associated with the Mt. Sharp sedimentary sequence rather than a massive lava flow. This leads to two hypotheses regarding the hematite's formation: (1) Transport of soluble Fe^{2+} ions by anoxic fluids that encountered an oxidizing environment and subsequently precipitated relatively insoluble Fe^{3+} minerals, or (2) in place oxidative weathering of Fe^{2+}-bearing materials by neutral to slightly acidic waters. In both settings, reduced iron (Fe^{2+}) is substantially more soluble than oxidized iron (Fe^{3+}). Depending on assumptions regarding the phase limiting solubility of Fe^{3+} (hematite or metastable phases such as ferrihydrite, schwertmannite, or jarosite), Fe^{2+} is calculated to be 10^9 to 10^{11} times more soluble at pH 7 and 10^3 to 10^5 times more soluble at pH 2 using established thermodynamic data (Delany and Lundeen, 1991; Majzlan et al., 2004a; Majzlan et al., 2004b; Grevel and Majzlan, 2011).

For the first hypothesis, anoxic groundwater traveling through Mt. Sharp would transport Fe^{2+} in solution until encountering an oxidizing atmosphere or mixing with oxidizing local groundwaters. Hematite would form where mixing and Fe^{2+} oxidation occurs. Hematite's precipitation is normally kinetically limited, so precursors such as schwertmannite, goethite or ferrihydrite would likely form first and over time undergo a phase transition to the thermodynamically stable phase hematite (Cornell and Schwertmann, 2006). The source of the Fe^{2+} could be dissolution of soluble ferrous sulfates within Mt. Sharp, although remote sensing data has shown only magnesium sulfates present (Milliken et al., 2010). However, subsurface deposits of soluble ferrous sulfate are not unreasonable on the basis of the similar solubility and chemical behavior of Fe^{2+} and Mg^{2+}. Additionally, ferrous sulfates are expected to be unobservable by remote sensing methods because these phases would be oxidized after exposure to UV light and water or atmospherically-produced oxidants (Jambor et al., 2000; Jerz and Rimstidt, 2003). The highly localized exposure of the hematite suggests mixing would have occurred as a redox-front, and hematite and its precursors could be present as cement and matrix fill or, less likely, directly deposited on the surface. Similar redox interface settings have been postulated to be the origin of iron oxides at Meridiani Planum, Mars (Hurowitz et al., 2010), although specifics of these settings could differ due to stagnant waters proposed at Meridiani Planum versus possible flowing water through Mt. Sharp at Gale Crater.

For the second hypothesis, slightly acidic waters would corrode olivine and other local silicate materials, neutralizing the waters and depositing hematite and/or its precursors under oxidizing conditions, Low pH water could be sourced from acid rain during periods of volcanism. In this scenario, other mineral phases should also be present because corrosion of local materials would have released cations and anions. In particular, this processes would

produce a high-SiO_2 residue near where the leaching has taken place that has not been reported to date at Gale Crater. However, the residue may be present only in small-scale outcrops or subsurface and therefore not detectable by CRISM, similar to Gusev Crater where subsurface high-SiO_2 (and high-Fe^{3+}-sulfate) deposits were observed by the Spirit rover but not detected by CRISM (Arvidson, et al., 2008).

Curiosity's scientific payload is well-equipped for testing hypotheses about hematite formation (Grotzinger et al., 2012). If hematite formed through in-place alteration of local materials, images from Mastcam and the Mars Hand Lens Imager (MAHLI) would show corrosion of local, originally Fe^{2+}-bearing, materials. In this scenario, hematite is also expected to be present as either a coating or cement fill and to be spatially associated with easily leached material. Data from the Chemical Camera (ChemCam), Alpha-Particle X-Ray Spectrometer (APXS), and Chemistry and Mineralogy Instrument (CheMin) would show the presence of amorphous SiO_2 and/or possibly phyllosilicates formed during weathering. Alternatively, if hematite formed through oxidation of Fe^{2+} transported by anoxic fluid flow, ChemCam, APXS, and CheMin analyses of ridge outcrops would be consistent with local bedrock enriched in an additional hematite component. MAHLI observations may also show hematite is present as a pore-filling cement.

Regardless of formation mechanism, both scenarios indicate that this ridge was a site of past active iron oxidation and thus is a site to search for evidence of past habitability. Iron oxidation that occurs in terrestrial environments at chemical interfaces is almost exclusively mediated by chemolithotrophic microorganisms that obtain energy by enzymatically coupling the oxidation of Fe^{2+} to the reduction of an oxidant such as O_2 or NO_3^- (Weber et al., 2006). While many locations on Mars provide potential chemical energy for life to conduct chemolithotrophic

metabolic processes, this hematite-bearing ridge represents a specific site that is accessible for detailed study by a rover where concentrated and localized iron oxidation occurred, and thus is a prime candidate for searching for signs of past habitability.

4.5 Acknowledgements

We thank the CRISM SOC for their assistance in developing the ATO observing scheme. This chapter was substantially improved by insightful reviews from E. Rampe, N. Tosca, S. Ruff, and one anonymous reviewer. We also thank S. McLennan and J. Hurowitz for comments on an early version of this chapter. This work was supported by CRISM APL/JPL contract 104149 and A.A.F. was funded by an NSF Graduate Student Research Fellowship, Grant #DGE-1143954. J.G.C. acknowledges financial support from the NASA Mars Fundamental Research Program (grant NNX11AH09G) and R.V.M. acknowledges the support of the Mars Exploration Program.

4.6 FIGURES

Figure 4.1: Ridge context map

(A) Themis daytime IR image overlain with MOLA elevations showing the context of Gale Crater. (B) Context Imager mosaic showing the area from the white box in (A) and oversampled CRISM observation FRT00021C92 (outlined in black). For comparison, the normal 18 m/pixel CRISM FRT000058A3 is also shown (no outline). Both observations contain the same number of pixels in the along-track direction, but the FRT00021C92 covers a smaller spatial areas in the along-track direction due to oversampling. The CRISM images are false color with R = 0.6 μm, G = 0.53 μm, and B = 0.44 μm. The hematite-bearing ridge is located at the base of a large trough descending from the top of Mt. Sharp.

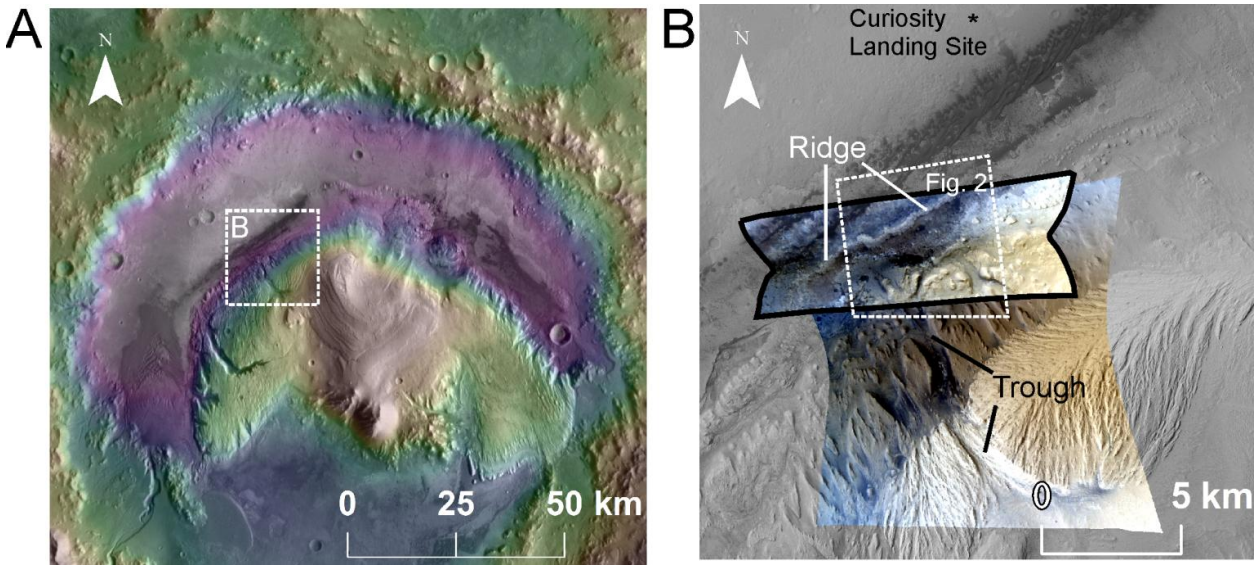

Figure 4.2: CRISM mineral detections at and around ridge

(A) HiRISE image DT1EA_009149_1750_009294_1750_U01 overlain by 5x5 median filtered 0.86 µm band depth mineral parameter map (red), indicative of red hematite. The map was created from FRT00021C92 and projected to along-track resolutions as small as 6 m/pixel. Additional mineral phases mapped using 18 m/pixel FRT data show areas with Fe/Mg smectite clay (2.3 µm band depth, yellow), sulfate minerals (SINDEX2, defined as convexity at 2.29 µm due to absorptions at 2.1 µm and 2.4 µm, green), and hydrated phases (1.9 µm band depth, blue) (Seelos et al., 2013). (B) Zoom in on hematite bearing ridge and ATO-generated 0.86 µm band depth map. The CRISM detections follow the uppermost stratum on the southern end of the finely layered ridge.

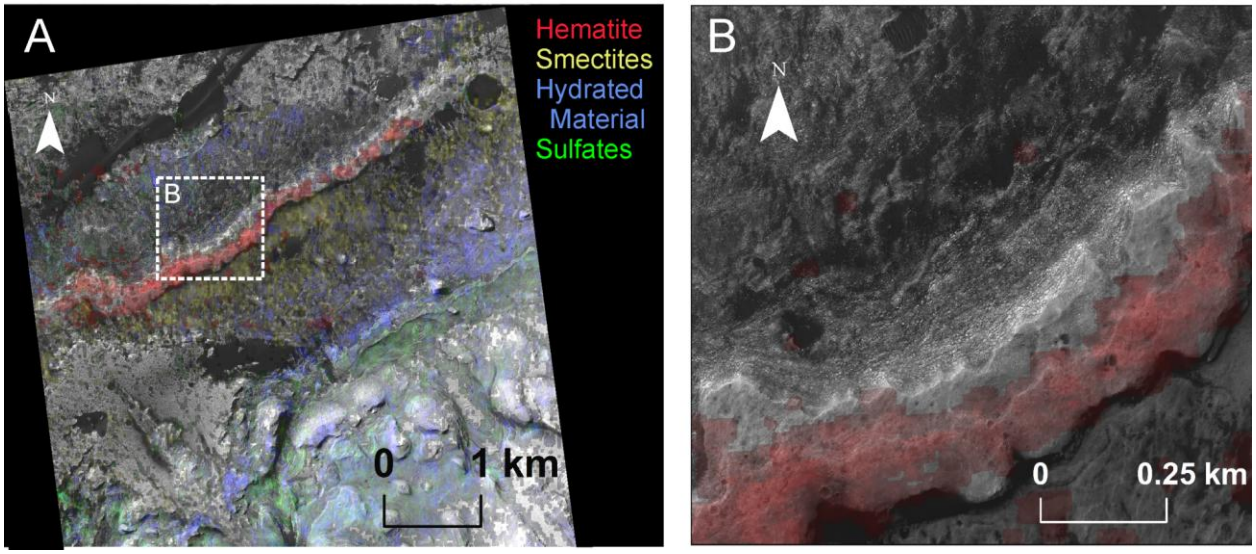

Figure 4.3: Geologic setting of ridge

(a) Measured strikes and dips and (b) cartoon transect from A to A' with a 2x vertical exaggeration along the average terrain slope with layers drawn showing approximate measured dips. Bedding orientation was calculated from HiRISE DTM DTEEC_009149_1750_009294_1750_U01 by extracting X (easting), Y (northing), and Z (elevation) coordinates along bedding planes using ENVI software. Coordinates were fit to a plane using least squares multiple linear regression in MATLAB (Metz, 2010; Watters et al., 2011), and the orientation of this plane represented the strike and dip of the measured bed. One-sigma confidence intervals for the strike and dip measurements were calculated for each bedding plane using a Monte Carlo simulation (bootstrapping with 1000 iterations) of a random residual error in elevation (Metz, 2010). Only every other bedding measurement is shown for clarity in the figure.

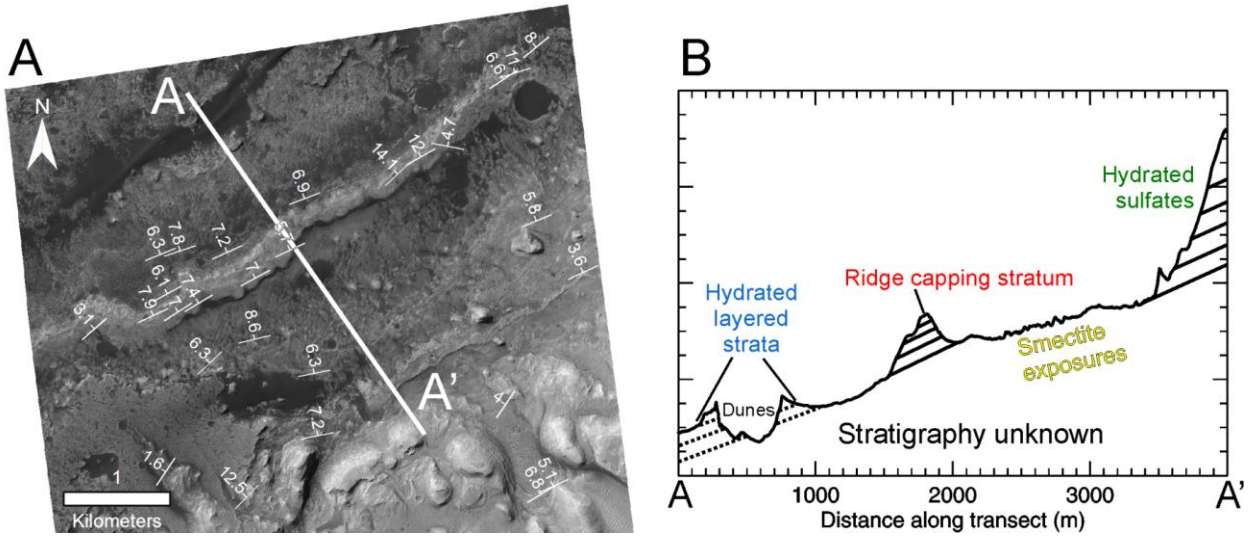

Figure 4.4: CRISM ridge spectrum and laboratory analogs

Average of hundreds of CRISM I/F spectra from the area on the southern side of ridge normalized by column averages of pixels from the same columns. The steep slope at wavelengths shorter than ~0.55 µm is likely an artifact of the normalization and incomplete removal of atmospheric aerosols. The bands around 0.55 µm and 0.86 µm as well as local maximum near 0.75 µm are consistent with red crystalline hematite. (B) Bidirectional reflectance iron oxide laboratory spectra from the USGS spectral library (red hematite GDS27, lepidocrocite, goethite, ferrihydrite), Morris et al. 1985 (red hematite HMS03), and Lane et al., (2002) (gray hematite HM1R2).

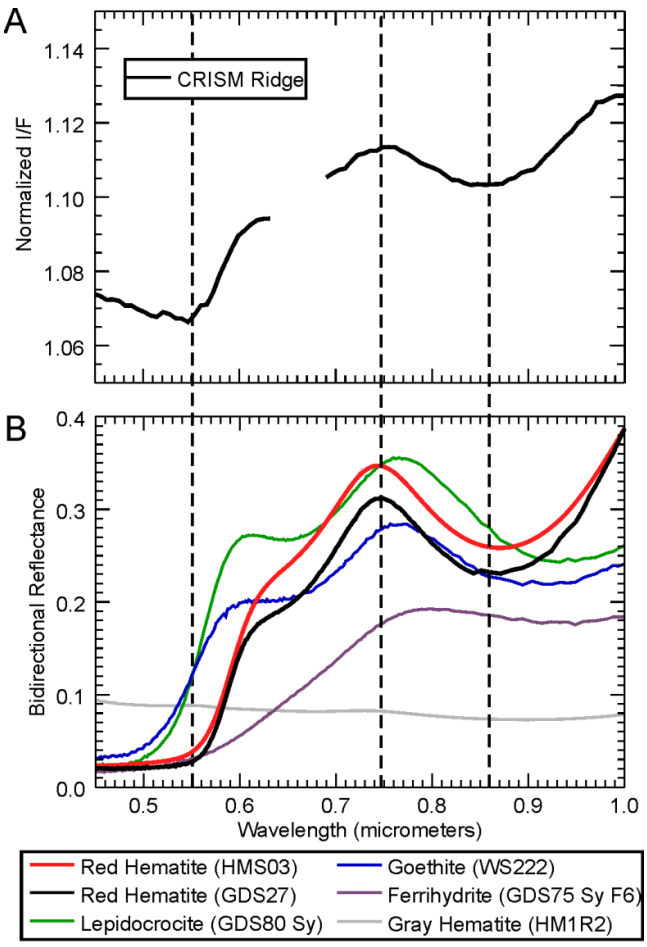

4.7 REFERENCE CITED

Arvidson, R.E., and 20 others, 2008, Spirit Mars Rover Mission to the Columbia Hills, Gusev Cater: Mission over and selected results from the Cumberland Ridge to Home Plate: Journal of Geophysical Research, v. 113, doi:10.1029/2008JE003183.

Cornell, R. M. and Schwertmann, U. 2006. The Iron Oxides: Structure, Properties, Reactions, Occurences, and Uses. *John Wiley & Sons.*

Delany, J.M., and Lundeen, S.R., 1991, The LLNL Thermochemical Data Base: Revised Data and File Format for the EQ3/6 Package: Lawrence Livermore National Laboratory.

Grevel, K.-D., and Majzlan, J., 2011, Internally consistent thermodynamic data for metal divalent sulphate hydrates: Chemical Geology, v. 286, no. 3–4, p. 301–306, doi:10.1016/j.chemgeo.2011.05.016.

Grotzinger, J., and 25 others, 2012, Science Laboratory Mission and Science Investigation: Space Science Reviews, v. 170, p. 5–56, doi:10.1007/s11214-012-9892-2.

Hurowitz, J.A., Fischer, W.W., Tosca, N.J., and Milliken, R.E., 2010, Origin of acidic surface waters and the evolution of atmospheric chemistry on early Mars: Nature Geoscience, v. 3, p. 323–326, doi:10.1038/ngeo831.

Jambor, J.L., Nordstrom, D.K., and Alpers, C.N., 2000, Metal-sulfate salts from sulfide mineral oxidation: Reviews in Mineralogy and Geochemistry, v. 40, p. 303–350, doi:10.2138/rmg.2000.40.6.

Jerz, J.K., and Rimstidt, J.D., 2003, Efflorescent iron sulfate minerals: Paragenesis, relative stability, and environmental impact: The American Mineralogist, v. 88, no. 11–12, p. 1919–1932.

Lane, M.D., Morris, R.V., Mertzman, S.A., and Christensen, P.R., 2002, Evidence for platy hematite grains in Sinus Meridiani, Mars: Journal of Geophysical Research, v. 107, 5126, doi:10.1029/2001JE001832.

Majzlan, J., Navrotsky, A., and Schwertmann, U., 2004a, Thermodynamics of iron oxides: Part III. Enthalpies of formation and stability of ferrihydrite (Fe(OH)3), schwertmannite (FeO(OH)3/4(SO4)1/8), and Fe2O3: Geochimica et Cosmochimica Acta, v. 68, p. 1049–1059, doi:10.1016/S0016-7037(03)00371-5.

Majzlan, J., Stevens, R., Boerio-Goates, J., Woodfield, B.F., Navrotsky, A., Burns, P.C., Crawford, M.K., and Amos, T.G., 2004b, Thermodynamic properties, low-temperature heat-capacity anomalies, and single-crystal X-ray refinement of hydronium jarosite, (H3O)Fe3(SO4)2(OH)6: Physics and Chemistry of Minerals, v. 31, p. 518–531, doi:10.1007/s00269-004-0405-z.

Metz, J.M., 2010, A study of the record of ancient sedimentary rocks on Mars using MER, HiRISE and CRISM images [Ph.D. dissertation]: Department of Geology and Planetary Science, Caltech, Pasadena, Calfornia.

Milliken, R.E., Grotzinger, J.P., and Thomson, B.J., 2010, Paleoclimate of Mars as captured by the stratigraphic record in Gale Crater: Geophysical Research Letters, v. 37, doi:201010.1029/2009GL041870.

Morris, R.V., Jr, H.V.L., Lawson, C.A., Jr, E.K.G., Nace, G.A., and Stewart, C., 1985, Spectral and other physicochemical properties of submicron powders of hematite (α-Fe2O3), Maghemite (γ-Fe2O3), Magnetite (Fe3O4), Goethite (α-FeOOH), and Lepidocrocite (γ-FeOOH): Journal of Geophysical Research, v. 90, p. 3126–3144, doi:10.1029/JB090iB04p03126.

Murchie, S., and 49 others, 2007, Compact Reconnaissance Imaging Spectrometer for Mars (CRISM) on Mars Reconnaissance Orbiter (MRO): Journal of Geophysical Research, v. 112, doi:10.1029/2006JE002682.

Murchie, S.L., and 16 others, 2009, A synthesis of Martian aqueous mineralogy after 1 Mars year of observations from the Mars Reconnaissance Orbiter: Journal of Geophysical Research, v. 114, doi:10.1029/2009JE003342.

Pelkey, S.M., Mustard, J.F., Murchie, S., Clancy, R.T., Wolff, M., Smith, M., Milliken, R., Bibring, J.-P., Gendrin, A., Poulet, F., Langevin, Y., and Gondet, B., 2007, CRISM multispectral summary products: Parameterizing mineral diversity on Mars from reflectance: Journal of Geophysical Research, v. 112, doi: 10.1029/2006JE002831.

Seelos, K.D., Seelos, F.P., Murchie, S.L., Arvidson, R.E., and Fraeman, A.A., 2013, Mosaicked hyperspectral CRISM data: mineralogic variability of the MSL landing site and possible traverse in Gale Crater, 44th Lunar and Planetary Science Conference, abstract #2814.

Thomson, B.J., Bridges, N.T., Milliken, R., Baldridge, A., Hook, S.J., Crowley, J.K., Marion, G.M., De Souza Filho, C.R., Brown, A.J., and Weitz, C.M., 2011, Constraints on the origin and evolution of the layered mound in Gale Crater, Mars using Mars Reconnaissance Orbiter data: Icarus, v. 214, p. 413–432, doi:10.1016/j.icarus.2011.05.002.

Watters, W.A., Grotzinger, J.P., Bell, J., III, Grant, J., Hayes, A.G., Li, R., Squyres, S.W., and Zuber, M.T., 2011, Origin of the structure and planform of small impact craters in fractured targets: Endurance Crater at Meridiani Planum, Mars: Icarus, v. 211, no. 1, p. 472–497, doi:10.1016/j.icarus.2010.08.030.

Weber, K.A., Achenbach, L.A., and Coates, J.D., 2006, Microorganisms pumping iron: Anaerobic microbial iron oxidation and reduction: Nature Reviews. Microbiology, v. 4, p. 752–764, doi:10.1038/nrmicro1490.

Chapter 5: Future *In Situ* Observation of the Hematite Ridge with Curiosity

ABSTRACT

Curiosity's instrument payload will be a powerful tool for investigating the hematite-bearing ridge described in Chapter 4. Although at the time of writing the rover is still ~6 km north of the ridge, high resolution color imaging and low resolution spectral remote sensing data of the ridge collected by Curiosity are consistent with the CRISM and HiRISE orbital observations. Once Curiosity does arrive at Mt. Sharp, strategic path planning to reach the hematite-rich ridge top will be necessary to find a traversable route that provides access to the most scientifically rewarding targets. A detailed *in situ* campaign at the ridge is proposed and consists of survey remote sensing coupled with targeted contact science, drilling, and both mineralogical and reduced carbon compound analyses. Using this strategy, Curiosity is well equipped to distinguish between predicted end-member textural scenarios for ridge materials, which will be essential to understand the formation and evolution of ridge.

5.1 INTRODUCTION

The Curiosity Mars rover is equipped with a payload of scientific instruments that were selected for their ability to address questions about the habitability of ancient and modern Mars [*Grotzinger et al.*, 2012], and these instruments will be powerful tools for investigating the hematite-bearing ridge described in Chapter 4. In this chapter, we briefly review Curiosity's instrument payload and describe the "ground-truth" remote sensing observations the rover has been able to make of the ridge since landing. We then consider the detailed measurement campaign Curiosity should conduct when reaching the ridge and discuss how the instrument

capabilities will be used to distinguish between the predicted end-member textural possibilities for materials at the ridge. This thought experiment is based on a combination of investigations of orbital data, experience with the previous drill campaign at Yellowknife Bay, and analyses of iron oxide and oxyhydroxide terrestrial samples that are textural analogs for ridge materials.

5.2 Background: Curiosity Payload

Curiosity's science payload is comprised of ten instruments (Fig. 5.1) that are used synergistically to address the mission objectives of assessing the biological potential and characterizing the geology of Gale Crater, investigating planetary processes that influence habitability, and characterizing the broad spectrum of surface radiation [*Grotzinger et al.*, 2012]. The instruments are used to analyze rock, soil, and atmospheric targets of interest through a combination of *in situ* remote sensing and contact investigations, and they are described briefly below.

5.2.1 Mast-mounted remote sensing instruments

Two instruments mounted on Curiosity's remote sensing mast, the Mast Cameras (Mastcam) and the ChemCam, give textural and compositional information about the terrain through remote sensing. The Mastcam is composed of a pair of fixed focal length cameras that capture broadband color (RGB) context imagery. One camera, the M-34, has a focal length of 34 mm, field of view of 15˚, and has a pixel scale of 22 cm at 1 km distance. The other, the M-100, has a 100 mm focal length, field of view of 5.1˚, and pixel scale of 7.4 cm at 1 km distance [*Grotzinger et al.*, 2012]. In addition to providing broadband color imaging, both cameras are equipped with a set of narrowband "science filters" intended for making multispectral measurements at 10 distinct wavelengths ranging from 440 nm to 1000 nm [*Bell et al.*, 2012].

The ChemCam instrument package is comprised of two instruments, a Laser-Induced Breakdown Spectrometer (LIBS) that provides remote elemental information at millimeter size scales, and the Remote Mast Imager (RMI) that generates high-resolution black and white context images with pixel sizes of 40-120 μm at distances of 2-6 m [*Maurice et al.*, 2012; *Wiens et al.*, 2012]. In addition to compositional information, pit sizes from the LIBS instrument have also been analyzed to infer information about physical properties of rocks and soils [*Arvidson et al., submitted*], and the spectrometer component of the LIBS instrument has been operated in a passive mode in which it collects high-resolution hyperspectral information of point targets from 400 – 850 nm [*Johnson et al.*, 2014a].

Also partially mounted on the mast is the Rover Environmental Monitoring Station (REMS), which is an environmental science instrument designed to investigate the modern day weather patterns at Gale Crater [*Gómez-Elvira et al.*, 2012]. Two booms equipped with wind, humidity, and air and ground temperature sensors are attached about halfway up the remote sensing mast, and a UV sensor assembly and pressure sensor that are also part of REMS are located on the rover deck.

5.2.2 Arm contact science instruments

The 70+ kg instrument arm is the home of the Sample Acquisition, Processing, and Handling (SA/SPaH) system, which is used to acquire rock and soil samples and deliver them to instruments internal to the rover (section 5.2.3). The SA/SPaH contains a dirt removal tool for cleaning dusty rock surfaces, a scoop for collecting loose soil samples, and a drill that is used to collect consolidated rock samples [*Anderson et al.*, 2012]. The SA/SPaH also houses two scientific instruments that provide textural and compositional information through contact science, the Mars Hand Lens Imager (MAHLI) and the Alpha Particle X-Ray Spectrometer

(APXS). MAHLI is analogous to a geologist's hand lens and captures color images with spatial resolutions as high as 14 μm/pixel [*Edgett et al.*, 2012]. MAHLI can focus on targets at distances from 21 mm to infinity, and the instrument is also equipped with white and UV LEDs for nighttime imaging. The APXS similar to instruments flown on Pathfinder, Spirit, and Opportunity, but with higher detection sensitivities and shorter necessary integration times, and this instrument provides elemental analyses of rock and soil targets [*Campbell et al.*, 2012].

5.2.3 Rover body instruments

Two instruments located inside the body of Curiosity, Chemistry and Mineralogy (CheMin) and Sample Analysis at Mars (SAM), require delivery of drilled or scooped samples from the SA/SPaH. CheMin is an X-Ray Diffraction (XRD) instrument that also has X-ray Fluorescence (XRF) capabilities [*Blake et al.*, 2012]. CheMin provides definitive mineralogy, with a quantification accuracy of ±15% for minerals that are present in concentrations of 12% and above. The SAM instrument suite is comprised of three individual instruments, a Quadrupole Mass Spectrometer (QMS), a Gas Chromatograph (GC), and a Tunable Laser Spectrometer (TLS) [*Mahaffy et al.*, 2012]. Together, these instruments address carbon chemistry through detecting the presence of organic compounds, determining the chemical state of other light elements besides carbon, and detecting isotopic ratios that are indicative of planetary evolution.

Two additional instruments in the rover body are Dynamic Albedo of Neutrons (DAN) and Radiation Assessment Detector (RAD). DAN is a neutron spectrometer that measures the abundance and distribution of hydrogen in the shallow Martian subsurface [*Mitrofanov et al.*, 2012]. RAD is an energetic particle detector whose primary science objectives include

characterizing the energetic particle spectrum at Mars and providing input to help understand the radiation input to any future or past life on Mars [*Hassler et al.*, 2012].

A fifth instrument on the rover body, MARDI (Mars Descent Imager), is an imager located under the belly of the rover and was used primarily to image Curiosity's descent onto the floor of Gale Crater [*Grotzinger et al.*, 2012]. Since landing, MARDI has also been used to image the terrain directly below the vehicle.

5.3 Curiosity's Initial Observations of the Ridge

Steep slopes, abundant scarps, and rocky terrain precluded Curiosity from landing directly on the flanks of Mt. Sharp. The rover instead landed on the flat plains of Gale Crater, approximately 4 km due north of the mound's base and 6 km north of the eastern-most edge of the hematite ridge (Fig. 5.2). Soon after touching down at Bradbury Landing, Curiosity drove 451 m east towards Yellowknife Bay, where coordinated measurements from the rover's full payload provided evidence that the area was once a habitable fluvio-lacustrine environment [*Grotzinger et al.*, 2014]. After completing the work at Yellowknife Bay, Curiosity began a ~8.6 km southwest trek towards the entrance point of Mt. Sharp, which is defined by a break in the dune field that surrounds the mound (Fig. 5.2).

At the time of writing, Curiosity is still several kilometers from the mound and hematite ridge. Despite this distance, both the Mastcam M-100 and M-34 cameras have been able to collect RGB images of the ridge at several locations along the traverse due in part to the cameras' high resolving power at long distances and in part to low atmospheric opacities at the time of imaging (Fig. 5.3, 5.4(a)). Close examination of these images show that the ridge is layered (Fig. 5.3(a)), with the layers dipping at angles that are qualitatively similar to the layers in the overlying sulfate stacks. The ridge is also composed of light-toned bedrock that contrasts

with the surrounding dark basaltic sands. Steep scarps designate the edges of the ridge in some locations, and confirm its erosive resistant nature in comparison with the surrounding terrain.

On sol 467 and 475, during a period of particularly low atmospheric opacity, ChemCam acquired passive spectra from point targets on a portion of the ridge ~5 km away from the rover. These data are presented and analyzed in *Johnson et al.,* [2014b], and they provide the first high-resolution "ground truth" spectral data of the ridge. The ChemCam data cover a wavelength range from 400 nm - 850 nm, and show the ridge materials are associated with an enhanced 535 nm band, a minor 670 nm band, and a reflectance peak at ~750 nm followed by a downturn (Fig. 5.4). All of these features are consistent with the Compact Reconnaissance Imaging Spectrometer for Mars (CRISM) observations of the ridge (Fig. 4.4) and the presence of crystalline hematite.

Mastcam was also commanded to use its narrow band "science filters" to acquire multispectral images of the same area of the ridge on sols 467 and 475. These data cover a much larger spatial area than the ChemCam point targets, but they have much lower spectral resolution and higher uncertainties in measured values. Analyses of the Mastcam images again presented in *Johnson et al.,* [2014] show the ridge has a relatively low 900 nm : 1000 nm ratio and high 900 nm - 1000 nm slope with respect to the surrounding terrain (Fig. 5.5). When combined with the observed downturn between 750 nm - 850 nm from the ChemCam passive spectra, these findings are consistent with the ridge containing material that has an absorption centered between 850 nm and ~950 nm. An absorption near this location is caused by an $^6A_1 \rightarrow {}^4T_1$ electronic transition in iron, and it is a staple in all iron oxide reflectance spectra [*Morris et al.*, 1985]. The low spectral resolution of the Mastcam data and cutoff at 850 nm of the ChemCam data, however, does not

allow for determination of the exact position of the absorption minimum, which precludes definitively identifying hematite as the responsible iron oxide from these data alone.

5.4 Ridge Approach and Initial Reconnaissance

Strategic path planning during the ridge approach will require carefully selecting a traversable route that is both time-efficient and that will provide access to the most scientifically rewarding targets. A combination of mobility constraints and analyses of orbital and *in situ* remote sensing data will therefore be the inputs that drive the selection of a specific area within the ~6 km long ridge for Curiosity to explore in detail (Fig. 5.6).

High Resolution Imaging Science Experiment (HiRISE) digital elevation models (DEMs) show that slopes greater than 20˚ surround the ridge at many locations (Fig. 5.7). Field tests on Earth have demonstrated that Curiosity is capable of traversing 20+˚ slopes on clean bedrock surfaces [*Arvidson et al., submitted*], but if the bedrock is covered by debris, the amount of slip the rover experiences may increase to the point where these slopes are no longer traversable. There are a few locations along the edge of the ridge, however, that are bounded by slopes <15˚, and several of these breaks are near locations with strong hematite signatures in the CRISM data (Fig. 5.7). These areas are the best candidate locations for Curiosity to safely climb onto the ridge top where the CRISM hematite signature was mapped.

Once Curiosity crosses the ridge, Curiosity will likely conduct a detailed *in situ* investigation, including drilling samples to deliver to SAM and CheMin, to determine the mechanisms behind its formation, evolution, and potential as a previously habitable environment. At Yellowknife Bay, currently the only site where Curiosity has completed drilling activities [e.g. *Grotzinger et al.*, 2014], the rover spent several weeks performing systematic remote sensing and contact science reconnaissance to provide geologic context and to guide the selection of two drilling

locations. Building on the success of this campaign, a similar strategy of remote sensing coupled with targeted contact science should be implemented for investigation of the hematite ridge.

Mastcam RGB and multispectral mosaics should be acquired of the area during initial ridge reconnaissance. Similar to the parameter mapping techniques used in the CRISM orbital data and the results from *Johnson et al.,* [2014] discussed in section 5.3, parameters such as the 900 nm : 1000 nm ratio and 900 nm - 1000 nm slope in the high-spatial resolution Mastcam image will provide an initial assessment of where and how hematite is distributed within the scene. These observations will be a key product for understanding the geologic context of the deposit and selecting hematite-rich locations for contact and drilled science. Mastcam multispectral data will also give an initial hint about other mineral phases that are associated with the hematite.

ChemCam passive spectra should also be collected at locations suggested as having hematite in the Mastcam multispectral data. Preliminary long distance observations have demonstrated the utility of ChemCam passive observations for detecting a variety of ferric and ferrous phases [*Johnson et al.*, 2014a], and this tool will provide higher spectral resolution data to complement Mastcam detections from selected locations. For targets of interest closer than 7 m, ChemCam should also acquire active LIBS spectra that will give compositional information about any iron oxides and associated phases that are present. On Mars, ChemCam LIBS data have detected increased iron content at the Rocknest rock field that was interpreted to be due to an iron-oxide cement [*Blaney et al., submitted*], although passive spectral data do not show clear evidence for iron oxides in these same rocks [*Johnson et al.,* 2014a]. This discrepancy is possibly due to the passive spectral signatures being obscured by the ubiquitous Martian dust.

5.5 Distinguishing Between Hematite Textures Using Contact Science

Clues to the origin of the hematite ridge will be preserved in its texture (section 4.4). The resistant nature of the ridge and common textural forms of iron oxides implies the hematite is likely present either as a coating, cement, or in a massive form. We have examined terrestrial iron oxide and oxyhydroxide samples (herein after referred to by the general term "iron oxides") with these end-member textures to understand how Curiosity may distinguish between them when the rover reaches the ridge and to predict the kinds of data it will collect (Fig 5.8). This thought experiment will help inform the decisions and interpretations of the detailed contact science and drill campaign Curiosity will likely conduct when reaching the ridge. Results are summarized in table 5.1.

We characterized each sample spectrally by collecting visible-to-near infrared (VNIR) spectra from 0.4 to 2.5 μm using an ASD field spectrometer. We also studied the fine-scale texture and the distribution of iron within the samples using reflected and transmitted light thin section analysis and backscattered-electron mapping using a JEOL JXA-8200 Electron Microprobe. Finally we characterized the composition of the samples through selected microprobe energy dispersive X-ray spectroscopy (EDS) spot analyses.

5.5.1 Iron oxides as dominant phase

Iron oxides are the dominant phase in a red rock from San Bernardino, CA that was purchased from Burminco Rocks and Minerals (Fig. 5.8). Spectrally, this sample is a close match to laboratory spectra of powdered hematite because it has absorptions near 0.53 μm, 0.63μm, and 0.88 μm caused by iron electronic transfers, and well as a relative reflectance maximum near 0.75 μm (Fig. 5.9). The sample also has H_2O and OH features at 1.4 μm and 1.9 μm as well as a pair of small absorptions near 2.3 μm and 2.35 μm likely due to metal-OH

stretches from the presence of a mica-group phyllosilicate [*Clark et al.*, 1990]. Thin section analyses show at small spatial scales this rock is botryoidal, which is a common texture of iron oxides (Fig. 5.10) [*Cornell and Schwertmann*, 2006]. EDS analyses reveal the sample is primarily composed of iron oxide – silica mixtures, with a large light element component by mass (Fig 5.10, Table 5.2). A few locations were also found that have compositions similar to mica-group phyllosilicates, which is consistent with the VNIR spectral observations. To supplement the EDS elemental analyses, powdered samples from this rock were also run through the Bruker d8 Advance XRD to determine the mineralogy of the iron oxides present. The resulting XRD pattern indicated both goethite and hematite were present within the sample, along with an amorphous component (Fig. 5.11).

Despite its spectral similarity to the powdered laboratory hematite standard, very little of this sample is actually pure hematite and it is mostly composed of material with compositions closer to goethite. The spectral dominance of hematite over other iron oxides is well documented [*Cornell and Schwertmann*, 2006], and this behavior raises the possibility that despite its spectral similarity to hematite, the ridge material could also be a mixture of a various iron oxides phases with only a minor component of hematite. CheMin XRD analyses of drilled samples will be need to clearly distinguish the specific iron oxides phases present in the ridge.

If the ridge materials are similar in texture to this sample, they will appear to be massive in Mastcam-scale images, and botryoidal structures would be resolved in MAHLI (and possibly Mastcam) observations. LIBS-based compositions will be fairly homogenous across multiple locations and depths, although they may show variations in Fe and Si contents between shot locations. APXS data will be dominated and Fe and Si, and CheMin will show the sample is primarily dominated by iron oxides (Table 5.1).

5.5.2 Cements

Iron oxides are present as cements in sandstones from the Cambrian Lamotte Formation and Ordovician Roubidoux Formations, both located in Missouri (Fig. 5.8). Although the quartz-rich nature of these sandstones is not likely representative of Martian materials, the alluvial environments in which they formed are similar to environments inferred to have been present in the plains of Gale Crater [*Williams et al.*, 2013]. Thin section analyses show these samples are grain supported quartz sandstones cemented by a red-brown matrix (Fig. 5.12). In hand samples, these grain-supported sandstones are highly friable, indicating they are only weakly cemented.

EDS analyses and electron backscatter images revealed that the cement is composed of a mixture of Al-rich clays and only a small amount of iron oxides (Fig. 5.12, Table 5.3). Despite the relatively small amount of iron oxides in the sample compared with quartz and clay, their presence is clearly evident in the VNIR spectra. Both samples have spectra with electronic transition absorptions at ~0.5 μm, 0.65 μm, and 0.9 μm as well as a local maximum near 0.75 μm, intermediate between powdered laboratory goethite and hematite spectra (Fig. 5.13). The presence of these absorptions caused by only a small amount of iron oxide in the samples demonstrates that if hematite is present in the ridge as a cementing agent, it may only comprise a small volume percent of the entire bedrock despite its strong spectral signature. Both samples also have clear spectral evidence for Al-rich clays due to H_2O and OH absorptions at 1.4 and 1.9 μm, and Al-OH absorptions near 2.2 μm. For the Lamotte sandstone, the absorption at 2.2 μm is actually a doublet characteristic of kaolinite, while in the Roubidoux sandstone, the single absorption near 2.2 μm is more consistent with montmorillonite [*Clark et al.*, 1990].

If the ridge materials are cements, Mastcam and MAHLI images may be able to resolve individual grains, the distribution of cement between grains, and whether the sandstone is grain or matrix supported. These images may also show primary sedimentary features (e.g. bedding or mud cracks) that would provide information about materials' depositional environment. LIBS data will be heterogeneous between shot points, reflecting compositions of both the grains (likely basaltic) and matrix, and the size of LIBS pits will give information about the strength of the cement. APXS compositional data will also be reflective of the mixture of cement and grain compositions. If the sample has greater than 3 wt% of crystalline hematite (the detection limit for crystalline phases in CheMin [*Blake et al.*, 2012]) a sample delivered to CheMin will show minor to significant amounts of iron oxide, and the composition of the grains will also be noteworthy contributors to the sample's bulk composition (Table 5.1).

5.5.3 Coatings

River rocks from the Berrocal section of Rio Tinto, Spain represent iron oxides in the form of coatings (Fig 5.8). These coatings formed when seasonal evaporation of river waters rich in sulfuric acid and ferric iron left behind sulfate salts that, in the returning rainy season, subsequently underwent hydrolysis and precipitated as nanophase goethite [*Fernández-Remolar et al.*, 2005]. Spectrally, the Rio Tinto rocks have electronic transition absorptions at 0.5 µm, 0.65 µm, and 0.9 µm and a local maximum near 0.75 µm, consistent with laboratory powdered goethite (Fig 5.14). The samples also have absorptions near 1.4 µm, 1.9 µm, and 2.4 µm, consistent with sulfates such as jarosite (Fig 5.14) [*Clark et al.*, 1990]. The thin section analyses and backscattered electron images (Fig 5.14) show the iron oxide coating is only a few hundred microns thick, and EDS analysis of highly backscattering material reveals the coating is comprised of goethite-like iron oxides (Table 5.4, Fig 5.15). Similar to the cemented sandstones,

the coated samples once again highlight the spectral dominance iron oxides can have despite being present as only a minor phase in the whole sample.

If Curiosity encounters coatings at the ridge, they may appear homogenous at both Mastcam and MAHLI spatial scales. Any areas where the coating is patchy will provide information about the thickness of the coatings and the nature of underlying rocks. Laboratory experiments have demonstrated that depth profiling with LIBS can reveal compositional changes in sample suites consistent with the development of coatings and rinds [*Lanza et al.*, 2012], and LIBS measurements of hematite coated calcite from the Saline Valley, CA have shown this technique will be sensitive to hematite coatings in particular [*Sharma et al.*, 2007]. LIBS shots will therefore be spatially homogenous across sample locations but they will become less iron rich with increasing depth/shot number. APXS data will show the rock compositions are a mixture of iron oxides and composition of the underlying parent rock. Collecting a coating through drilling maybe problematic as Curiosity's drill does not save the upper-most portion of the drill core [*Anderson et al.*, 2012]. CheMin may therefore only show trace amounts of iron oxides in a coated sample (Table 5.1).

5.6 CONCLUSIONS

Even from ~6 km away, "ground-truth" remote sensing observations from Curiosity show the materials in the ridge are consistent with orbital predictions discussed in Chapter 4, and these observations strengthen the argument that the ridge should be a high priority target for Curiosity. When the rover eventually reaches the ridge, the best way to investigate it to understand its origin and evolution will be through a combination of remote sensing analyses and targeted contact science. The textures of the hematite in the ridge will reflect its formation mechanism,

and Curiosity will be able to distinguish between the three end-member textures that are likely to be present.

5.7 Acknowledgements

Paul Carpenter provided invaluable assistance in analyzing the samples with the electron microprobe.

5.8 TABLES

Table 5.1: Summary of Expected Observations for Iron Oxides with Different Textures

Texture	Mastcam	ChemCam	MAHLI	APXS	CheMin	SAM
Dominant Phase	At Mastcam spatial scales see massive exposures, perhaps including botryoidal structures.	LIBS-based compositions will be fairly homogenous both spatially and with depth, show variations in Fe and Si content between shot points.	MAHLI scale resolution able to resolve if sample has botryoidal texture similar to laboratory samples.	Data dominated by Fe and Si.	Samples dominantly iron oxides.	Search for reduced carbon compounds.
Cement	Individual grains and cement resolved in Mastcam scale images. Primary sedimentary features (e.g. cross bedding or mud cracks) provide evidence for depositional environment.	Compositions from LIBS rasters heterogeneous and reflective of whether they are sampling grains or cements. Size of LIBS pits give information about strength of cement.	MAHLI scale resolution resolves distribution of cement between grains and whether material is grain- or matrix-supported sandstone.	Data show a mixture of iron oxides and grain compositions, likely basaltic for Martian material.	Samples have minor to significant amounts of iron oxides, composition of cemented grains also noteworthy contributors.	Search for reduced carbon compounds.
Coating	At Mastcam spatial scales, textures appear to be homogenous. Patchy coatings provide information on thickness of coatings and nature of underlying rocks.	LIBS shots homogeneous across sampling locations but will become less iron-rich with increasing depth/shot number.	Grains sizes of coatings too small to be resolved by MAHLI. Patchy coatings provide information on thickness of coatings and nature of underlying rocks.	Data show a mixture of iron oxides and underlying parent rock compositions.	Drilling will not preserve thin coating, delivered sample only shows trace amounts of iron oxides.	Search for reduced carbon compounds.

Table 5.2: Weight % Oxides for Massive Sample

Assume all Fe is present as Fe_2O_3 and calculate H_2O by difference. Na, Ti, Cr, P, Ba, Sr were <0.1 in all spots and not shown on table. Locations of spots are shown on figure 5.10.

Point #	MgO Wt %	Al_2O_3 Wt %	SiO_2 Wt %	K_2O Wt %	CaO Wt %	MnO Wt %	Fe_2O_3 Wt %	*H_2O* Wt %
1	<0.1	0.5	67.0	0.1	0.26	<0.1	13.8	18.2
2	0.1	0.7	24.5	0.6	0.4	0.1	47.7	25.7
3	0.1	0.8	3.5	0.1	0.7	0.2	73.6	20.9
4	<0.1	0.8	3.5	<0.1	0.8	0.2	74.0	20.6
5	0.1	0.8	3.6	<0.1	0.7	0.2	75.5	18.8
6	1.8	1.2	48.2	7.7	0.3	0.3	33.4	7.1

Table 5.3: Weight % Oxides for Cement Samples

Assume all Fe is present as Fe_2O_3 and calculate H_2O by difference. Cr, P, Ba, Sr were <0.1 in all spots and not shown on table. Locations of spot are shown on figure 5.11.

	Loc #	Na_2O Wt %	MgO Wt %	Al_2O_3 Wt %	SiO_2 Wt %	K_2O Wt %	CaO Wt %	MnO Wt %	Fe_2O_3 Wt %	TiO_2 Wt %	*H_2O Wt %*
Lam.	1	<0.1	<0.1	1.6	0.5	<0.1	<0.1	<0.1	95.5	1.3	*1.0*
	2	<0.1	0.1	0.7	4.2	<0.1	0.8	0.2	74.8	<0.1	*19.1*
	3	<0.1	<0.1	0.9	8.1	<0.1	0.6	0.3	63.8	<0.1	*26.0*
Roubidoux	1	<0.1	1.8	27.2	46.7	2.8	0.4	0.1	8.7	0.6	*11.4*
	2	<0.1	2.0	26.4	46.5	3.1	0.4	0.1	8.1	0.6	*12.5*
	3	<0.1	0.5	3.6	4.5	<0.1	0.1	0.1	76.2	<0.1	*13.8*
	4	<0.1	0.4	1.0	2.9	<0.1	0.1	0.1	84.6	<0.1	*10.1*
	5	0.1	0.5	3.5	6.4	<0.1	0.2	0.3	80.3	<0.1	*7.3*

Table 5.4: Weight % Oxides for Coated Samples

Assume all Fe is present as Fe_2O_3 and calculate H_2O by difference. N, K, Cr, Ba, Sr were <0.1 in all spots and not shown on table. Locations of spot are shown on figure 5.13.

	Loc #	MgO Wt %	Al_2O_3 Wt %	SiO_2 Wt %	CaO Wt %	MnO Wt %	Fe_2O_3 Wt %	TiO_2 Wt %	P_2O_5 Wt %	*H_2O Wt %*
Sample 1	1	<0.1	1.6	0.5	<0.1	<0.1	95.5	1.3	<0.1	*1.0*
	2	0.1	0.7	4.2	0.8	0.2	74.8	<0.1	<0.1	*19.1*
	3	<0.1	0.9	8.1	0.6	0.3	63.8	<0.1	<0.1	*26.0*
Sample 2	1	0.4	1.0	5.7	0.9	<0.1	81.1	<0.1	0.9	*9.3*

5.9 FIGURES

Figure 5.1: Instruments on the Curiosity Mars Rover

The instruments and their locations on the Curiosity Mars Rovers. Mastcam, MAHLI, and MARDI provide high resolution color context imagery. ChemCam, APXS, and SAM generate compositional information. REMS and RAD reveal information about the Martian environment, and DAN investigates the shallow subsurface. Figure from *Grotzinger et al.*, 2012.

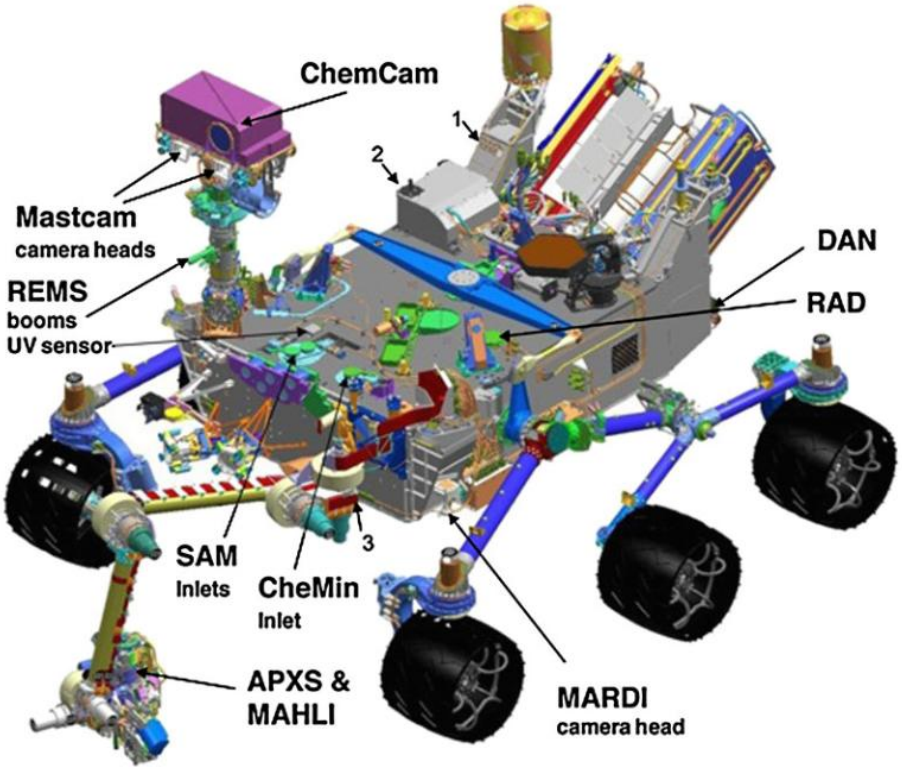

Figure 5.2: Curiosity traverse in Gale Crater

Curiosity traverse (red line) from landing to sol 574. The basemap is from the Context Imager (CTX) and data are shown on Mars Orbiting Laser Altimeter (MOLA) digital elevation map with 1.5x vertical exaggeration. North is approximately towards the lower right hand corner of the image. The ridge and trough described in Chapter 4 are labeled.

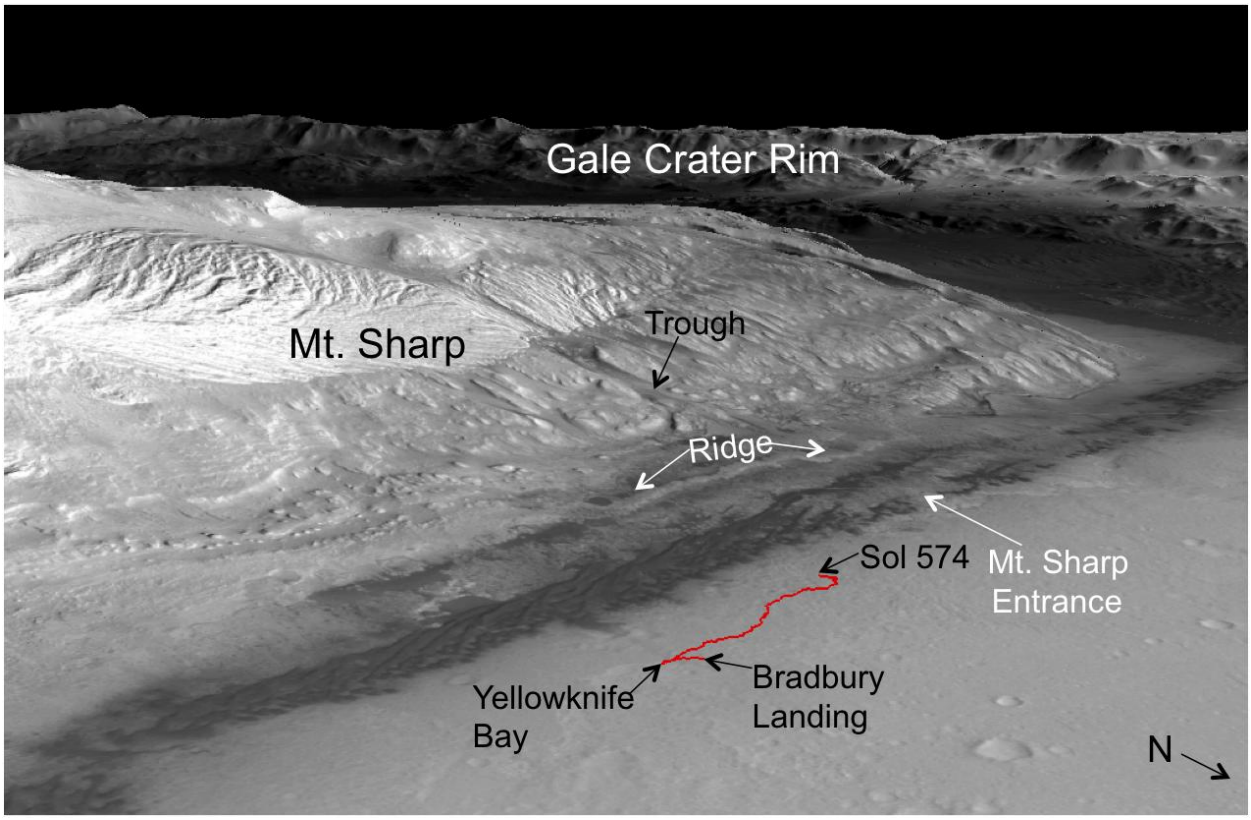

Figure 5.3: Sol 45 Mastcam Mosaic of Hematite Ridge

Sol 45 Mastcam R0 mosaic pointed south showing area with hematite-bearing ridge. The black box in (A) highlights the area shown blown up in (B).

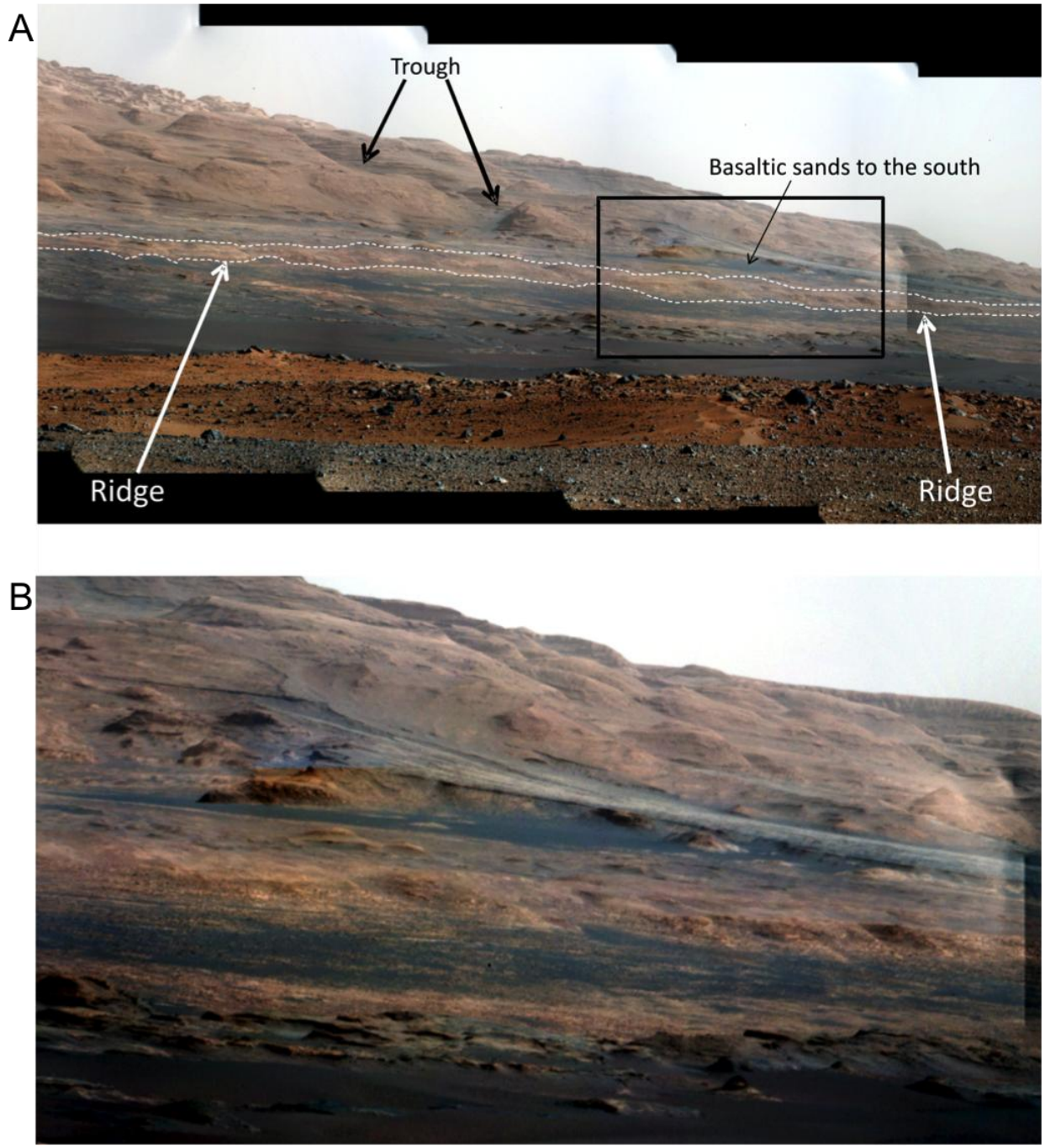

Figure 5.4: Mastcam spectral parameter mapping of ridge

(A) Sol 475 Mastcam images of ridge, pointed south. (B) Ratio and slope images show distinctive low 980/1013 nm ratio values an (C) high 908-1013 nm slope values for the ridge. Figures from *Johnson et al.*, 2014b.

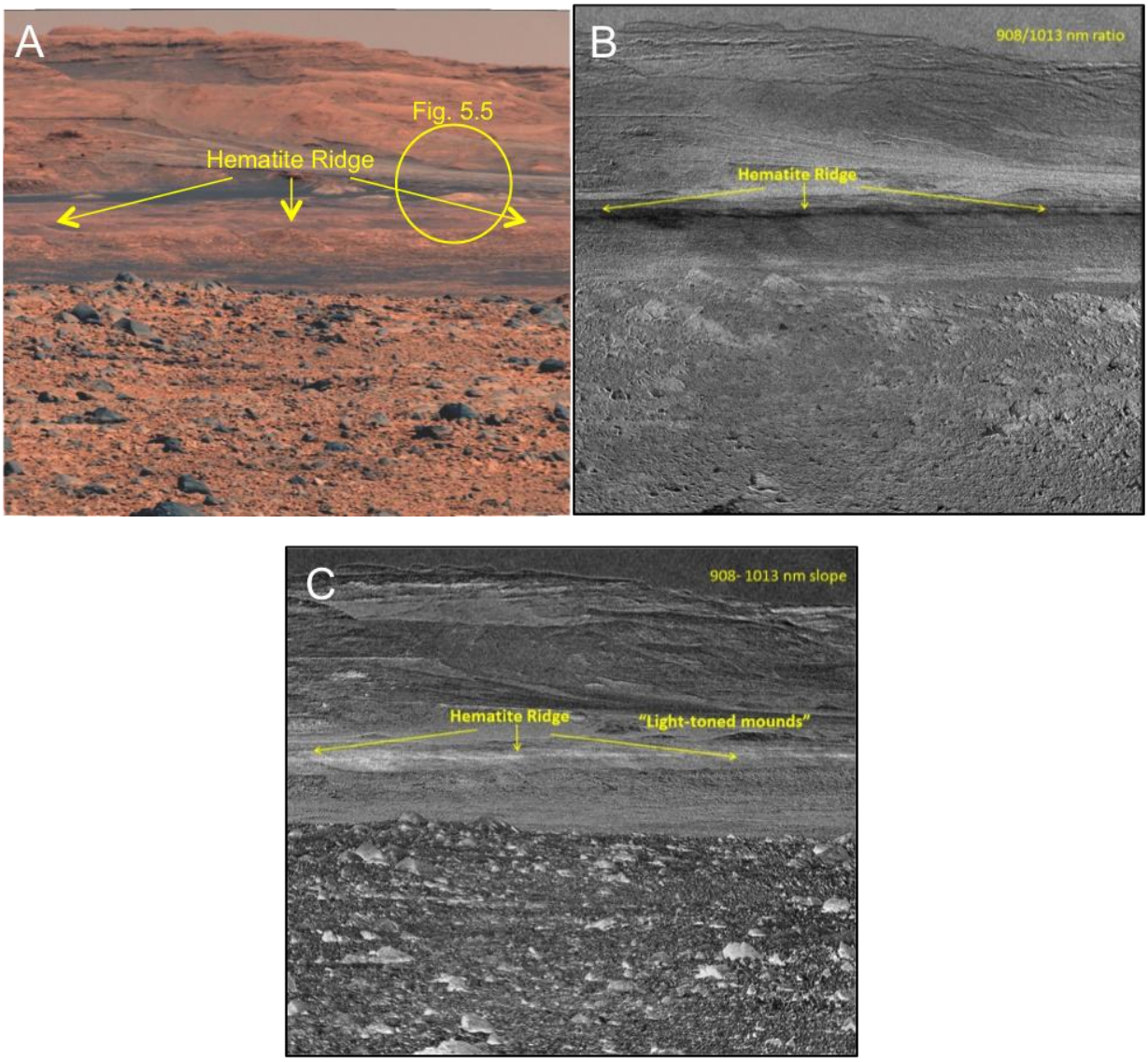

Figure 5.5: ChemCam Passive Spectra of Hematite Ridge

(A) ChemCam Remote Mast Imager (RMI) showing locations of (B) ChemCam passive spectra collected over the hematite ridge. Location 3 (green) was collected from the ridge and shows features that are consistent with hematite. For details and interpretations of additional spectra shown in this figure, see *Johnson et al.*, 2014b. Figure from *Johnson et al.*, 2014b.

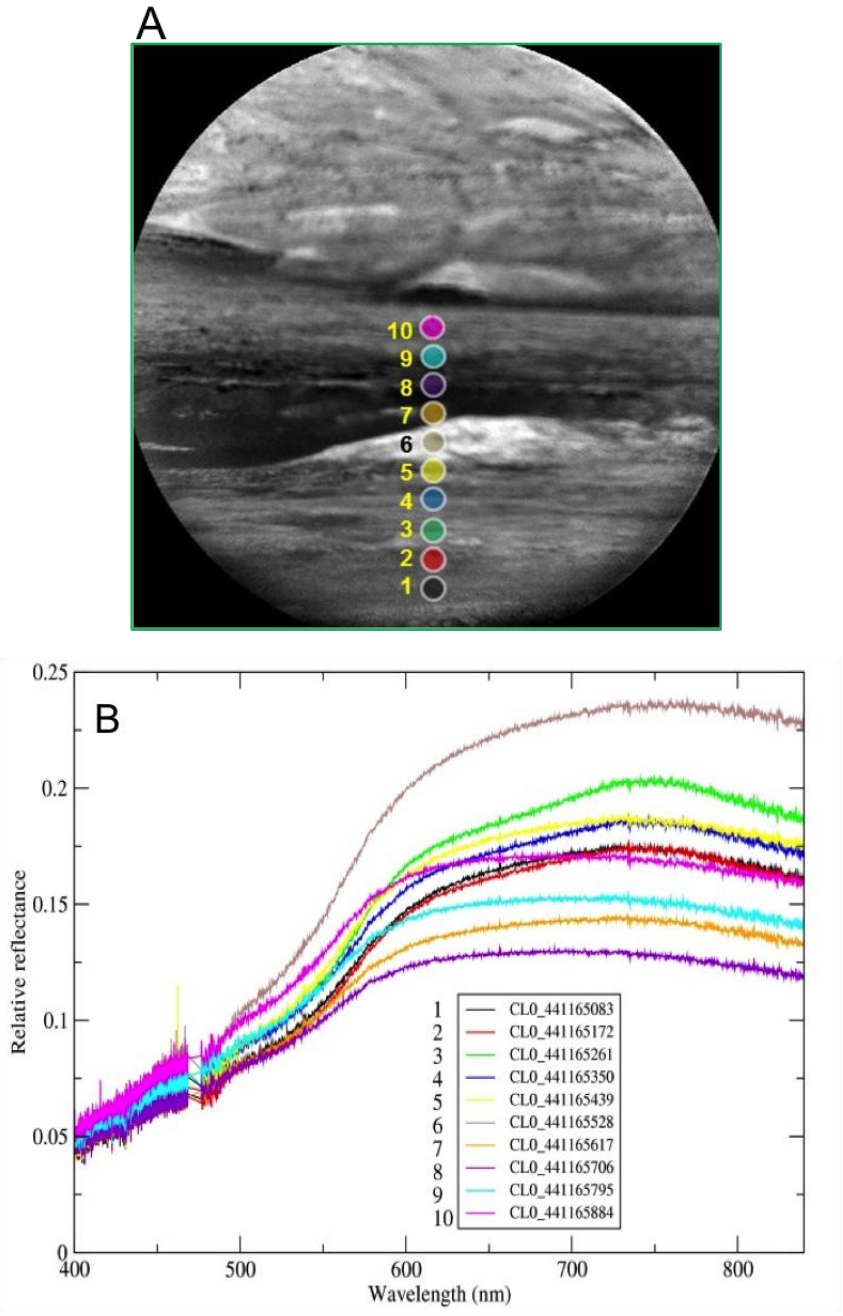

Figure 5.6: Curiosity rover size in relationship to ridge

HiRISE context image demonstrating scale of Curiosity rover versus the ridge. The white box in (A) is shown enlarged in (B). Curiosity is the size of the red rectangle, highlight by the red arrow. The small size of Curiosity in comparison to the entire ridge demonstrates the importance of wisely selecting key areas of the ridge to investigate in detail.

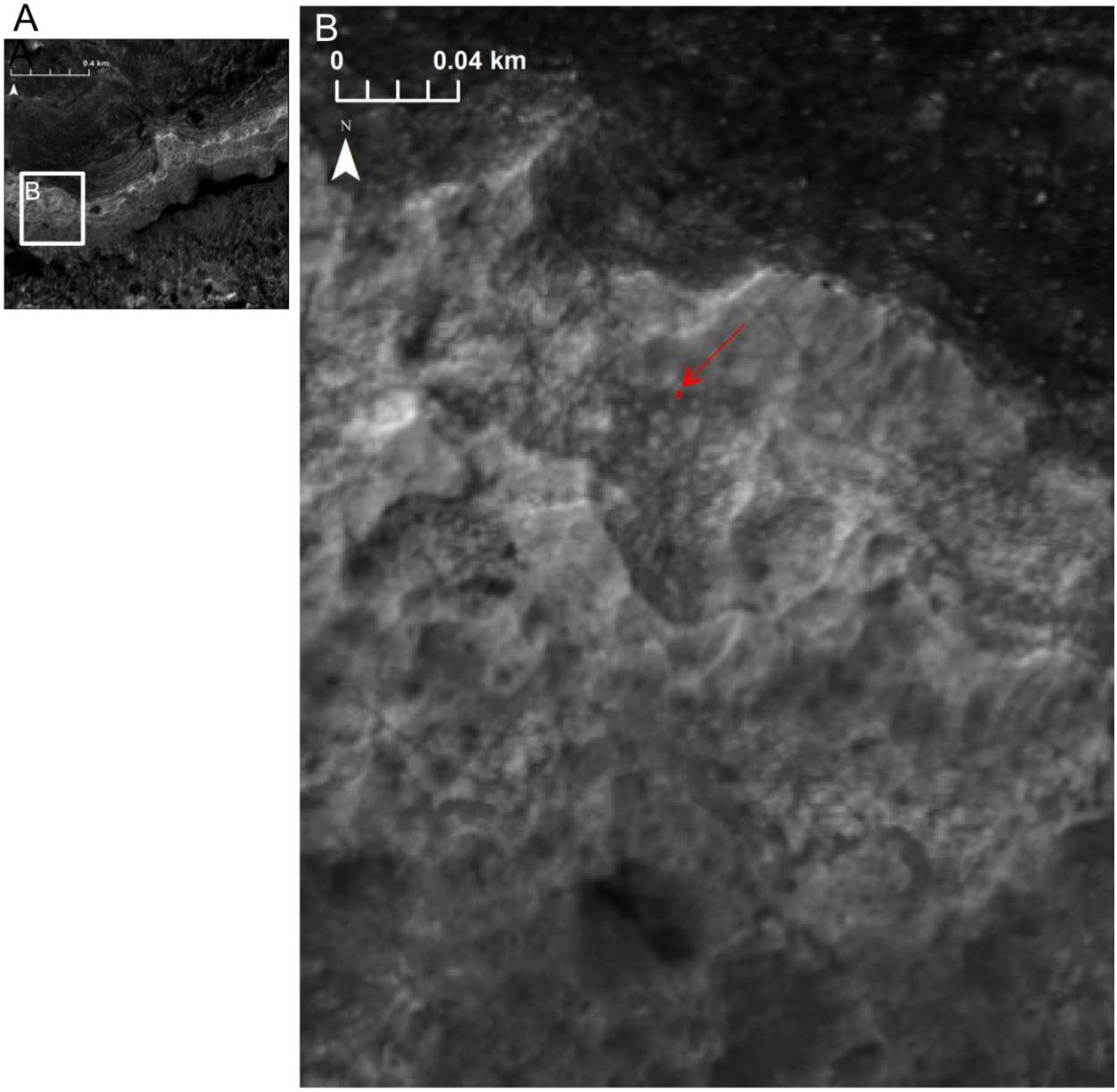

Figure 5.7: Ridge accessibility

HiRISE digital elevation map based slopes (red = 20˚+, yellow = 15-20˚) and CRISM 860 nm band depth map (green) overlain on HiRISE basemap. The area shown in the white box in (A) is blown up in (B). Possible areas for Curiosity to cross that will be safe and near hematite-rich outcrop are indicated by white arrows in (B).

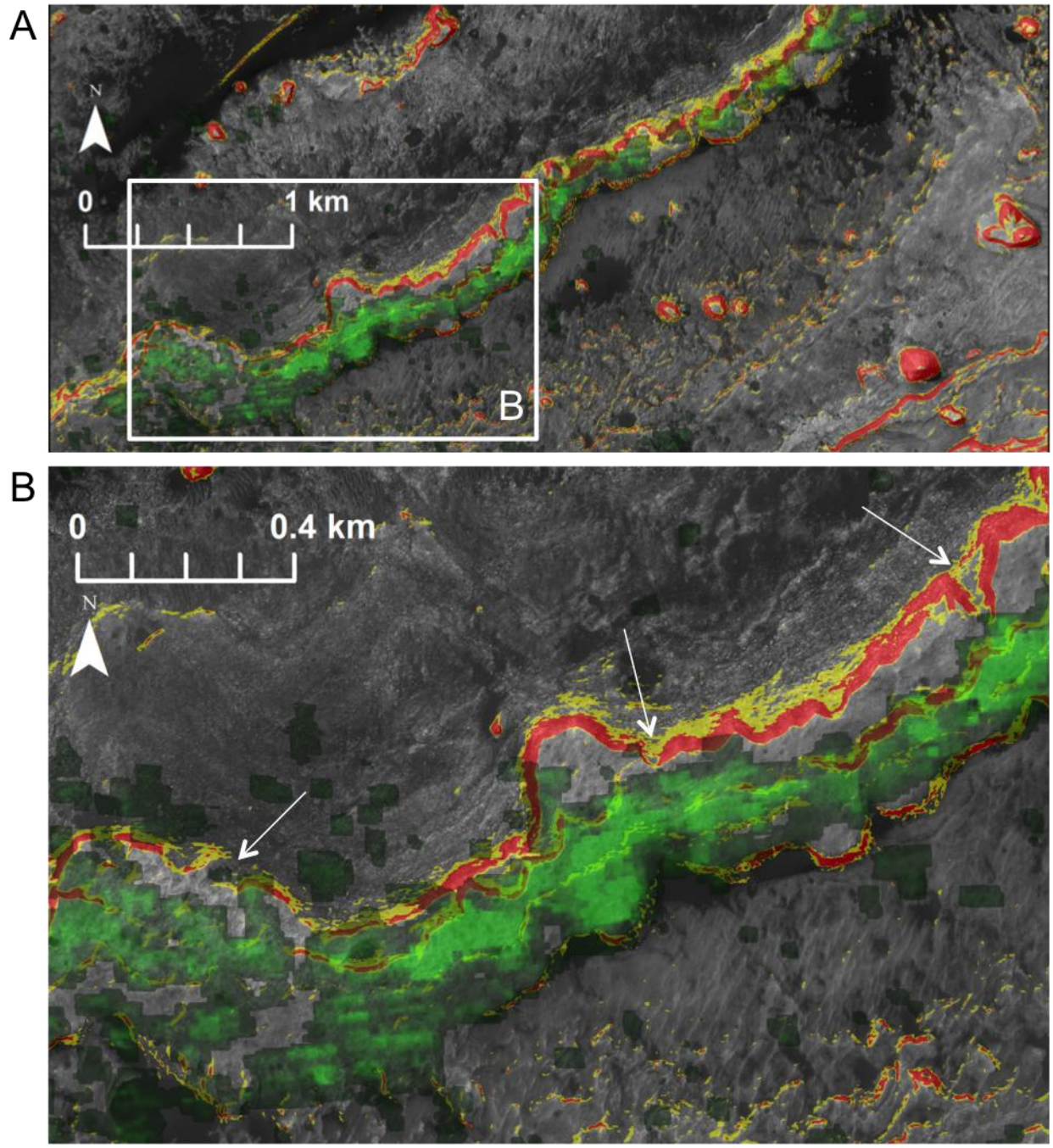

Figure 5.8: Iron oxide and oxyhydroxide whole rock samples

Images of whole rock iron oxide and oyxhydroxide samples showing (A) massive, (B,C) cemented, and coated (D-G) textures. A dime is shown for scale in A-E. Specific samples shown are (A) San Bernardino red rock, (B) Lamotte Formation sandstone, (C) Roubidoux Formation sandstone, (D) Rio Tinto coated rock #1 exterior, (E) Rio Tinto coated rock #2 interior, (F) Rio Tinto coated rock #1 interior, (G) Rio Tinto coated rock #2 interior.

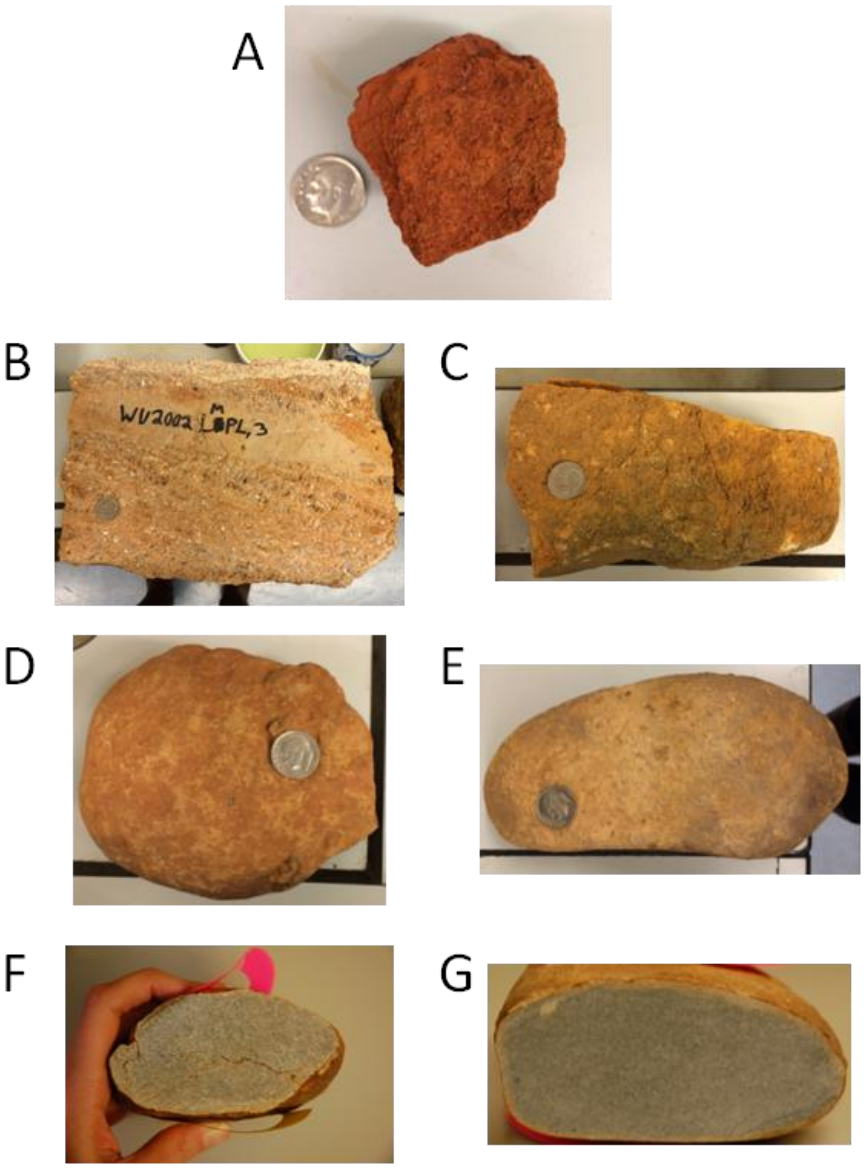

Figure 5.9: Massive sample spectrum

(A) Reflectance spectrum from San Bernardino red rock and (B) laboratory spectral library spectra from *Morris et al.*, 1985 (red hematite) and *Clark et al*, 2003 (all others). The short wavelength absorptions from this sample are closest to those of red hematite.

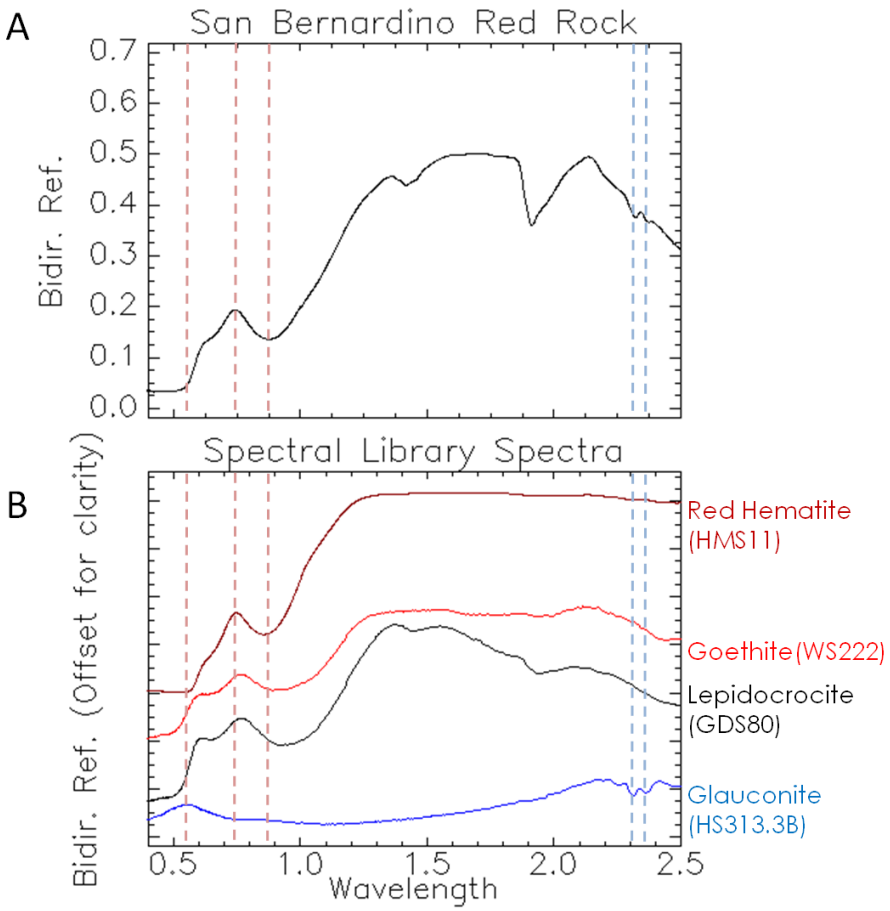

Figure 5.10: Massive sample thin section and backscatter electron images

(A) Transmitted light thin section image of San Bernardino red rock with (B,C) backscatter electron (BSE) images from two locations. Areas that are bright in BSE images have higher Fe content. The sample's botryoidal texture is evident at both spatial scales. Results from element analyses taken at numbered spots in (B,C) are shown in Table 5.2.

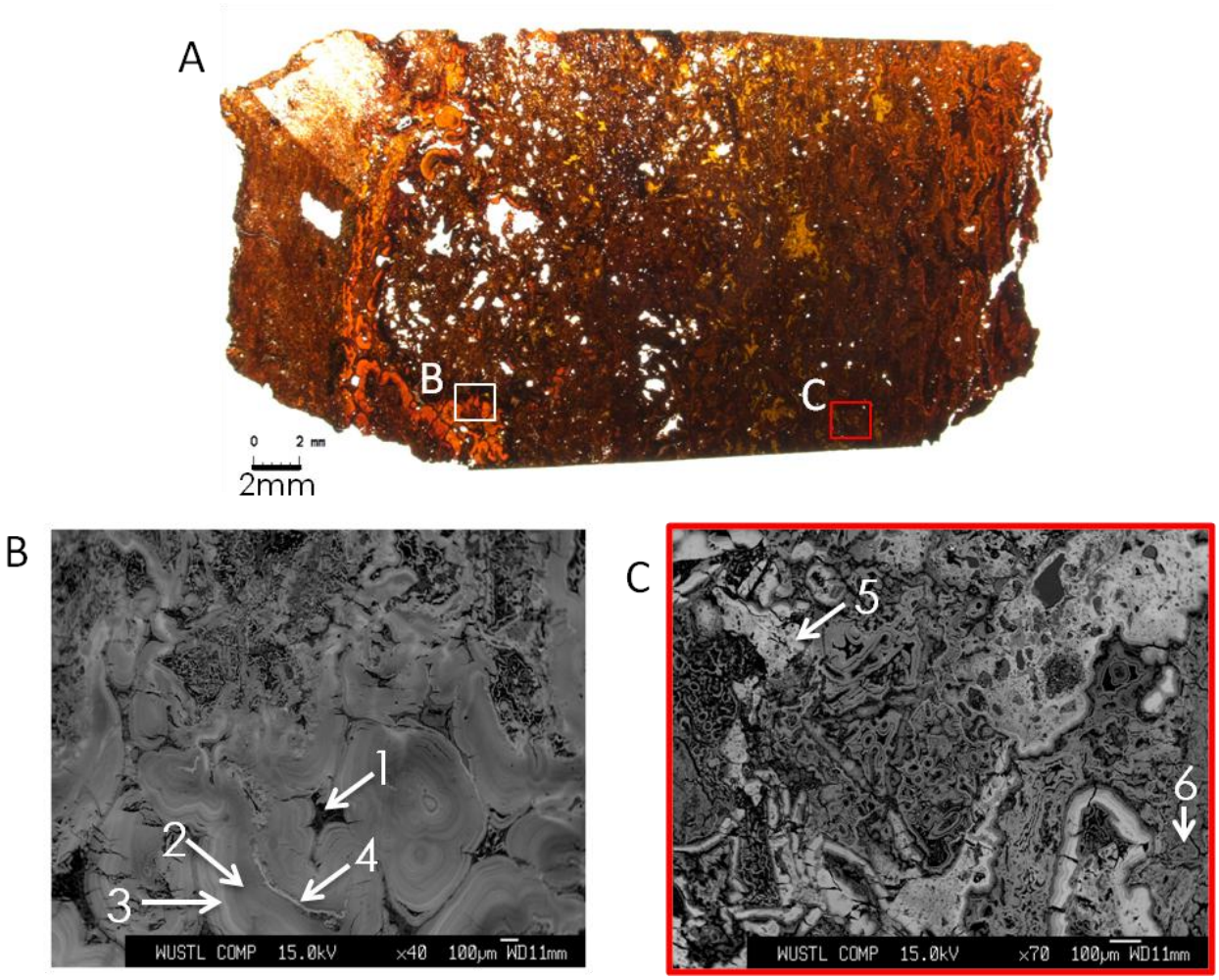

Figure 5.11: XRD analysis of massive sample

XRD data from massive sample. The uppermost graph (blue) shows the original pattern fit with goethtite and hematite (purple), while the middle graph (gray) shows the residual of this fit. The bottom graph (black) is background subtracted and shows the separate peak positions of goethite (pink vertical lines) and hematite (cyan vertical lines).

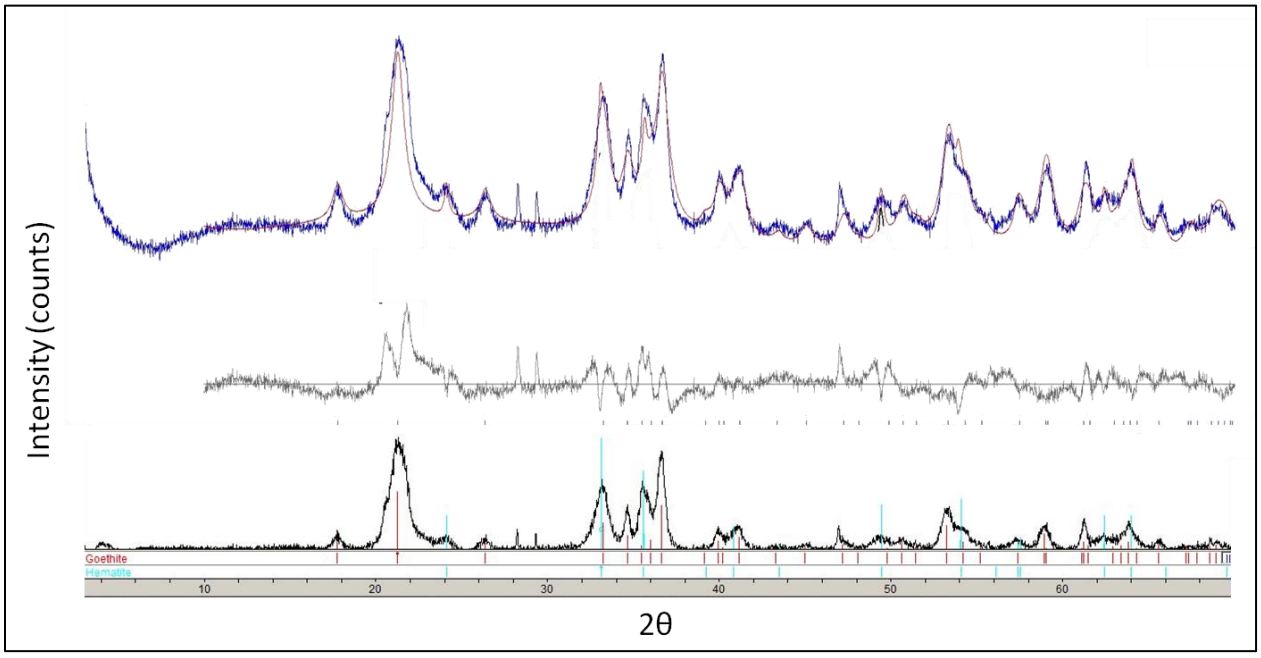

Figure 5.12: Cemented sample thin section and backscatter electron image

(A) Transmitted light thin section image of Lamotte sandstone and (B) backscattered electron (BSE) image of same area. (C) Transmitted light thin section image of Roubidoux sandstone and (D) backscattered electron image of same area with zoom on detail showing (E) cement between quartz grains and (F) iron rich grain Results from elemental analyses taken at numbered spots in (B,C-F) are shown in Table 5.3 and other phases that were mapped but not recorded are identified in red text.

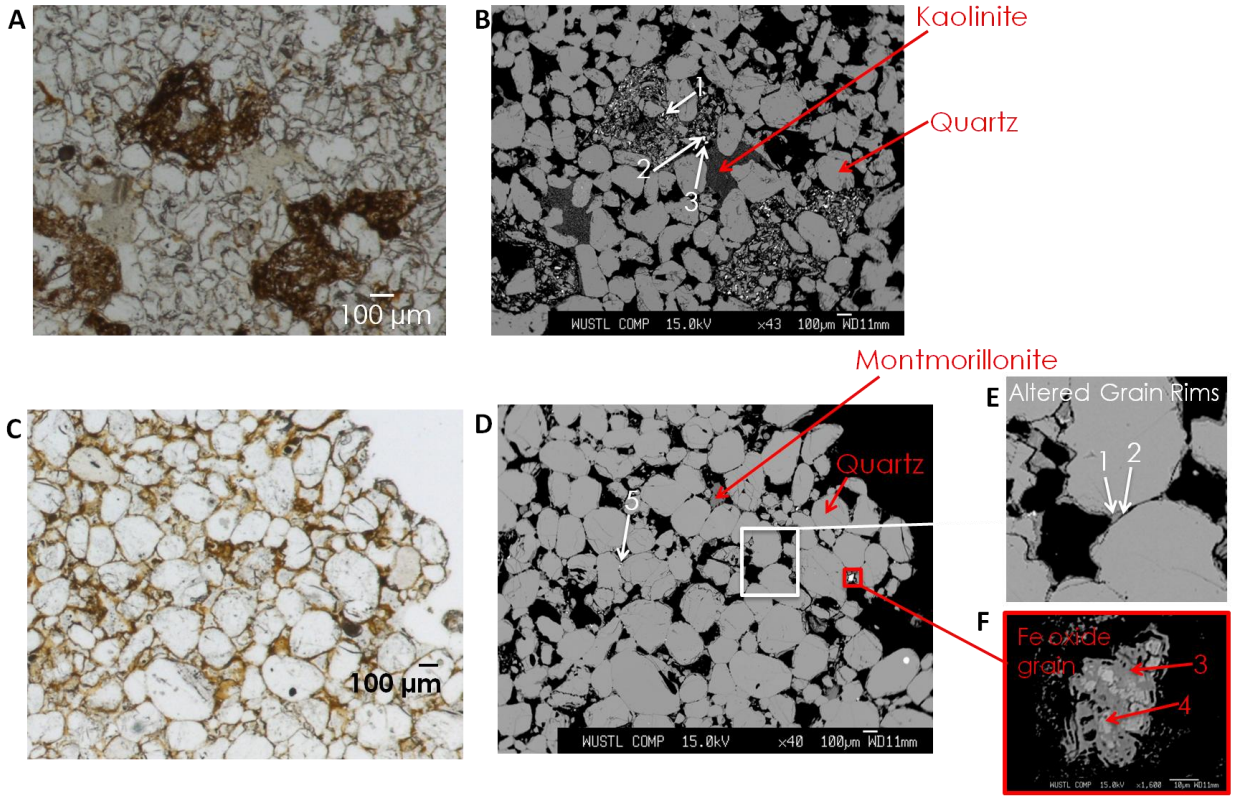

Figure 5.13: Cemented sample spectra

Reflectance spectra from two locations on (A) Lamotte and (B) Roubidoux sandstones with (C) laboratory spectral library spectra from *Morris et al.*, 1985 (red hematite) and *Clark et al*, 2003 (all others). Iron oxides clearly influence the reflectance spectra of these samples.

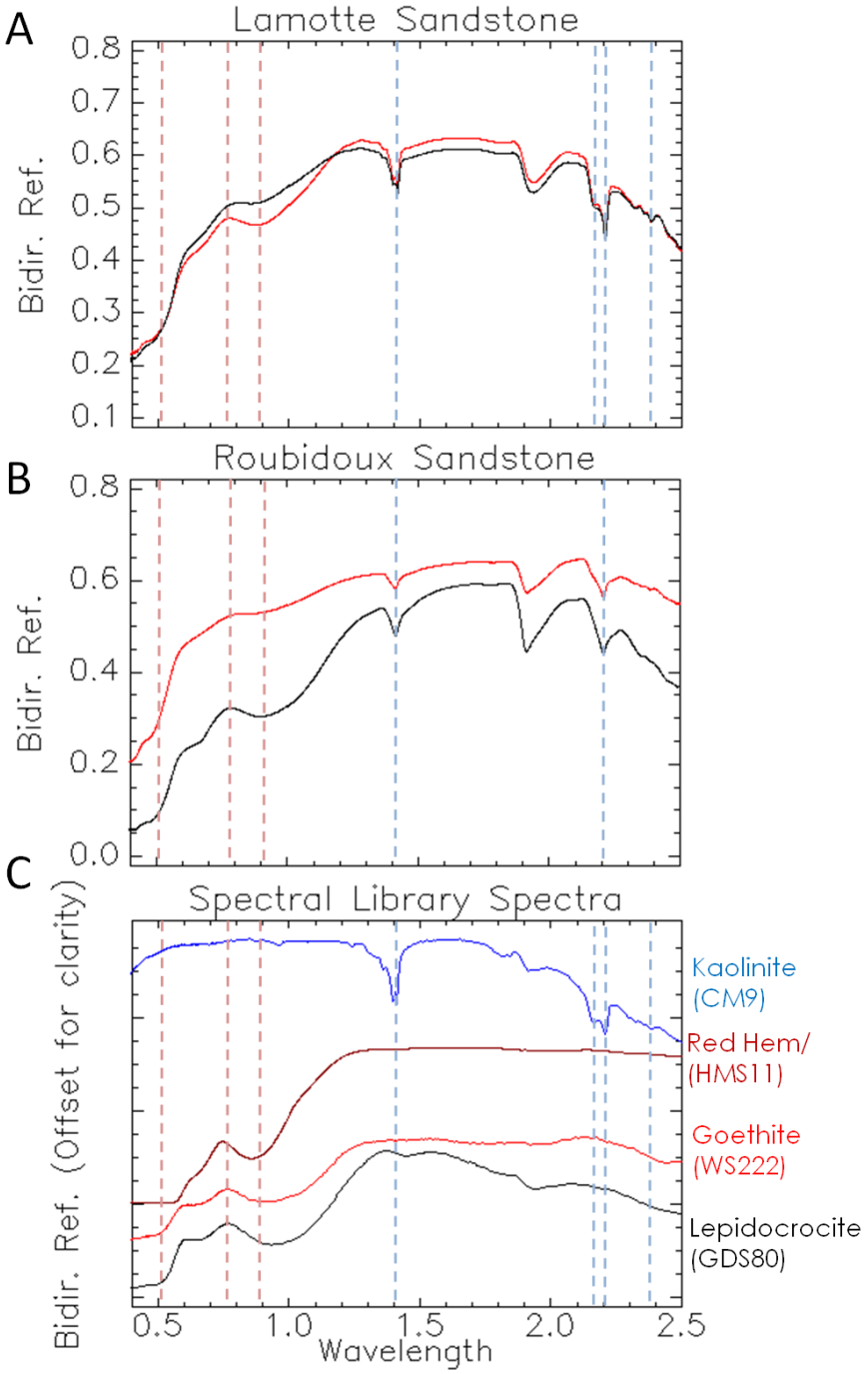

Figure 5.14: Coated sample spectra

Reflectance spectra from two locations on (A) Rio Tinto 1 and (B) Rio Tionto 2 coated rocks with (C) laboratory spectral library spectra from *Morris et al.*, 1985 (red hematite) and *Clark et al*, 2003 (all others). Iron oxides clearly influence the reflectance spectra of these samples.

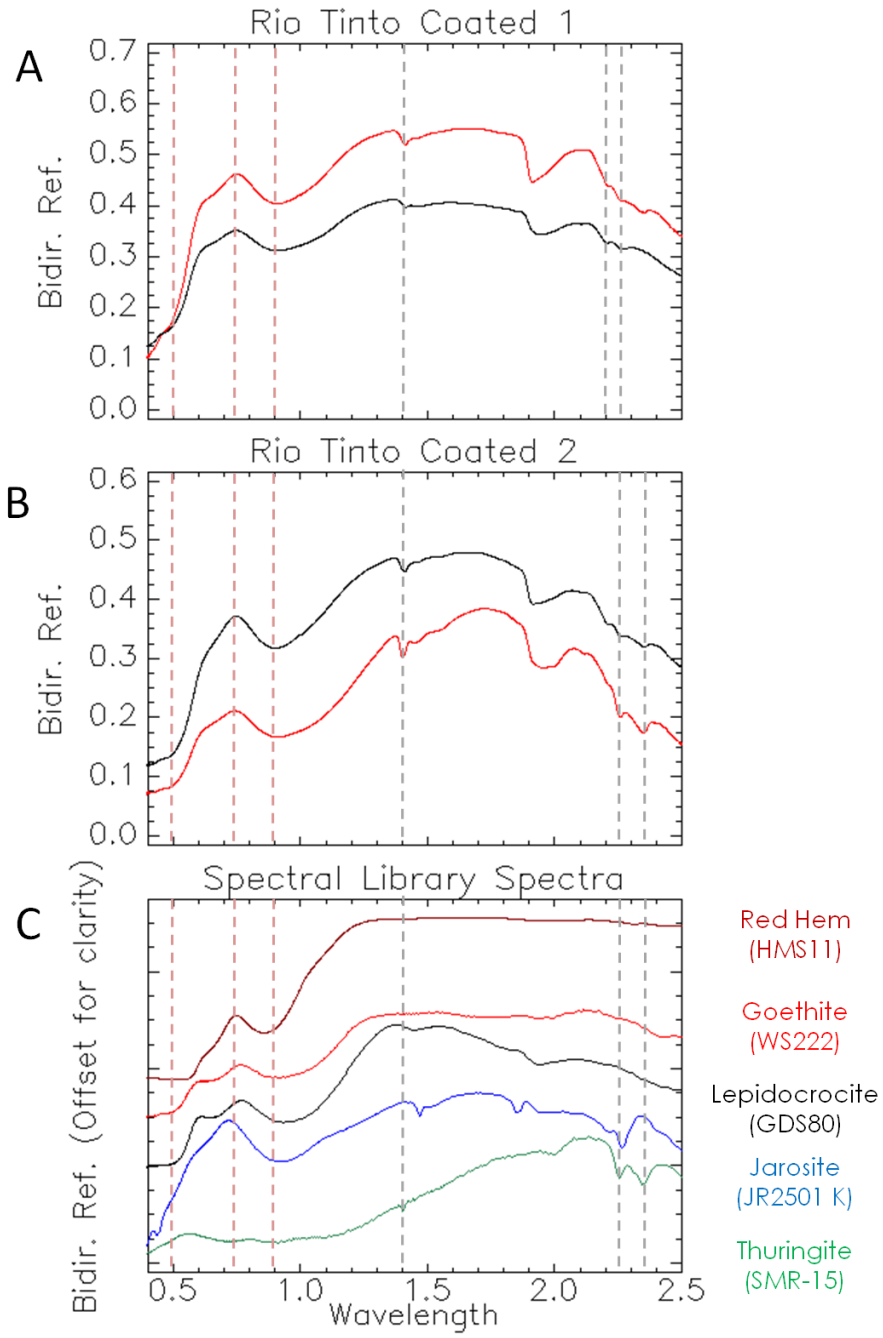

Figure 5.15: Coated sample thin section and backscatter electron image

(A, B) Transmitted light thin section image of Rio Tinto sample #1 and (C) backscattered electron (BSE) image of same area. (D) Transmitted light thin section image of Rio Tinto sample #2 and (E) backscattered electron image of subsetted area with (F) zoom on detail of coatings. Results from elemental analyses taken at numbered spots in (C,E,F) are shown in Table 5.4.

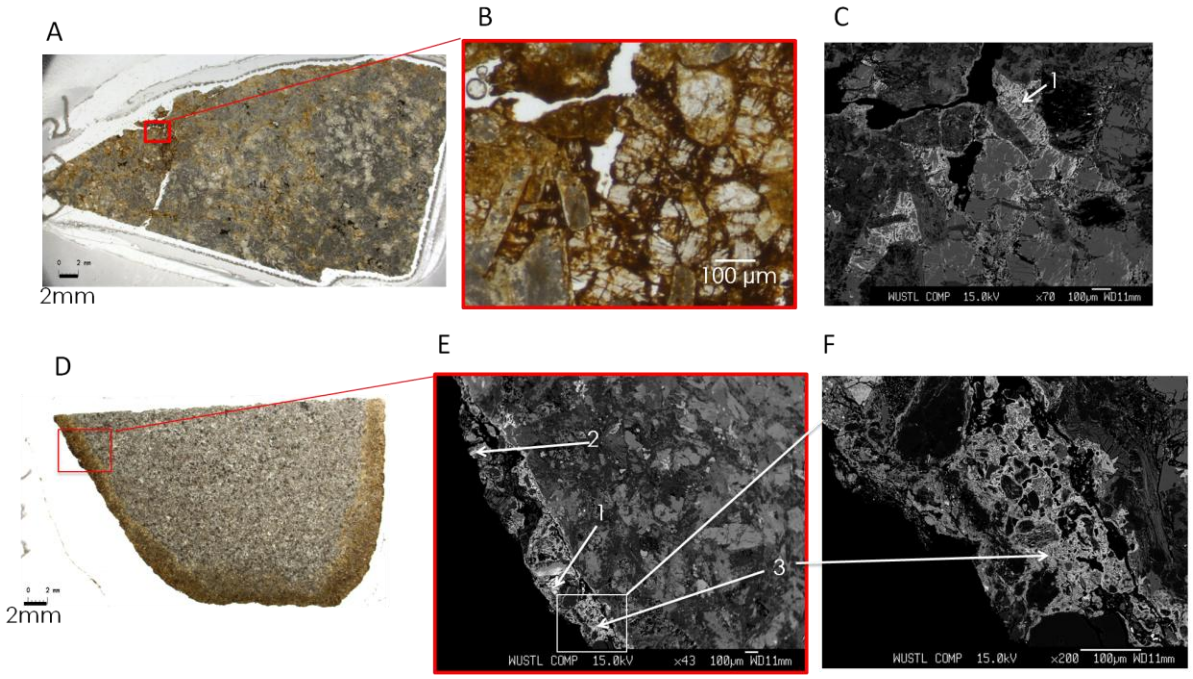

5.10 REFERENCES CITED

Anderson, R. C. et al. (2012), Collecting Samples in Gale Crater, Mars; an Overview of the Mars Science Laboratory Sample Acquisition, Sample Processing and Handling System, *Space Sci Rev*, *170*(1-4), 57–75, doi:10.1007/s11214-012-9898-9.

Bell, J. F., M. C. Malin, M. A. Caplinger, M. A. Ravine, A. S. Godber, M. C. Jungers, M. S. Rice, and R. B. Anderson (2012), Mastcam Multispectral Imaging on the Mars Science Laboratory Rover: Wavelength Coverage and Imaging Strategies at the Gale Crater Field Site, *Lunar and Planetary Science Conference*, vol. 43, p. 2541.

Blake, D. et al. (2012), Characterization and Calibration of the CheMin Mineralogical Instrument on Mars Science Laboratory, *Space Sci Rev*, *170*(1-4), 341–399, doi:10.1007/s11214-012-9905-1.

Campbell, J. L., G. M. Perrett, R. Gellert, S. M. Andrushenko, N. I. Boyd, J. A. Maxwell, P. L. King, and C. D. M. Schofield (2012), Calibration of the Mars Science Laboratory Alpha Particle X-ray Spectrometer, *Space Sci Rev*, *170*(1-4), 319–340, doi:10.1007/s11214-012-9873-5.

Clark, R. N., T. V. V. King, M. Klejwa, G. A. Swayze, and N. Vergo (1990), High Spectral Resolution Reflectance Spectroscopy of Minerals, *J. Geophys. Res.*, *95*(B8), PP. 12,653–12,680, doi:199010.1029/JB095iB08p12653.

Cornell, R. M., and U. Schwertmann (2006), *The Iron Oxides: Structure, Properties, Reactions, Occurrences and Uses*, John Wiley & Sons.

Edgett, K. S. et al. (2012), Curiosity's Mars Hand Lens Imager (MAHLI) Investigation, *Space Sci Rev*, *170*(1-4), 259–317, doi:10.1007/s11214-012-9910-4.

Fernández-Remolar, D. C., R. V. Morris, J. E. Gruener, R. Amils, and A. H. Knoll (2005), The Río Tinto Basin, Spain: Mineralogy, sedimentary geobiology, and implications for interpretation of outcrop rocks at Meridiani Planum, Mars, *Earth and Planetary Science Letters*, *240*(1), 149–167, doi:10.1016/j.epsl.2005.09.043.

Grotzinger, J. et al. (2012), Mars Science Laboratory Mission and Science Investigation, *Space Science Reviews*, *170*(1), 5–56, doi:10.1007/s11214-012-9892-2.

Grotzinger, J. P. et al. (2014), A Habitable Fluvio-Lacustrine Environment at Yellowknife Bay, Gale Crater, Mars, *Science*, *343*(6169), 1242777, doi:10.1126/science.1242777.

Hassler, D. M. et al. (2012), The Radiation Assessment Detector (RAD) Investigation, *Space Sci Rev*, *170*(1-4), 503–558, doi:10.1007/s11214-012-9913-1.

Johnson, J. R. et al. (2014a), ChemCam passive reflectance spectroscopy of surface materials at the Curiosity landing site, Mars, *Icarus*, doi:10.1016/j.icarus.2014.02.028.

Johnson, J.R., J.F. Bell, A.A. Fraeman, M. Rice, O. Gasnault, E. Cloutis, S. Le Mouelic, R.C. Wiens, and the MSL science Team. (2014b), Long-Distance Visible/Near-Infrared Reflectance Spectroscopy with ChemCam and Mastcam Along the Curiosity Rover Traverse, *8th Mars Conference*, abstract submitted.

Lanza, N. L., S. M. Clegg, R. C. Wiens, R. E. McInroy, H. E. Newsom, and M. D. Deans (2012), Examining natural rock varnish and weathering rinds with laser-induced breakdown spectroscopy for application to ChemCam on Mars, *Appl. Opt.*, *51*(7), B74–B82, doi:10.1364/AO.51.000B74.

Mahaffy, P. R. et al. (2012), The Sample Analysis at Mars Investigation and Instrument Suite, *Space Sci Rev*, *170*(1-4), 401–478, doi:10.1007/s11214-012-9879-z.

Maurice, S. et al. (2012), The ChemCam Instrument Suite on the Mars Science Laboratory (MSL) Rover: Science Objectives and Mast Unit Description, *Space Sci Rev*, *170*(1-4), 95–166, doi:10.1007/s11214-012-9912-2.

Mitrofanov, I. G. et al. (2012), Dynamic Albedo of Neutrons (DAN) Experiment Onboard NASA's Mars Science Laboratory, *Space Sci Rev*, *170*(1-4), 559–582, doi:10.1007/s11214-012-9924-y.

Morris, R. V., H. V. Lauer. Jr, C. A. Lawson, E. K. Gibson, G. A. Nace, and C. Stewart (1985), Spectral and Other Physicochemical Properties of Submicron Powders of Hematite (α-Fe_2O_3), Maghemite (γ-Fe_2O_3), Magnetite (Fe_3O_4), Goethite (α-FeOOH), and Lepidocrocite (γ-FeOOH), *J. Geophys. Res.*, *90*(B4), 3126–3144, doi:10.1029/JB090iB04p03126.

Sharma, S. K., A. K. Misra, P. G. Lucey, R. C. Wiens, and S. M. Clegg (2007), Combined remote LIBS and Raman spectroscopy at 8.6 m of sulfur-containing minerals, and minerals coated with hematite or covered with basaltic dust, *Spectrochimica Acta Part A: Molecular and Biomolecular Spectroscopy*, *68*(4), 1036–1045, doi:10.1016/j.saa.2007.06.046.

Wiens, R. C. et al. (2012), The ChemCam Instrument Suite on the Mars Science Laboratory (MSL) Rover: Body Unit and Combined System Tests, *Space Sci Rev*, *170*(1-4), 167–227, doi:10.1007/s11214-012-9902-4.